Interaction of Supra-Thermal Ions with Turbulence in a Magnetized Toroidal Plasma

THÈSE N^{O} 4543 (2009)

PRÉSENTÉE LE 3 DÉCEMBRE 2009

À LA FACULTÉ SCIENCES DE BASE

CRPP ASSOCIATION EURATOM

PROGRAMME DOCTORAL EN PHYSIQUE

ÉCOLE POLYTECHNIQUE FÉDÉRALE DE LAUSANNE

POUR L'OBTENTION DU GRADE DE DOCTEUR ÈS SCIENCES

PAR

Gennady PLYUSHCHEV

acceptée sur proposition du jury:

Prof. G. Dietler, président du jury
Prof. A. Fasoli, directeur de thèse
Dr J. Graves, rapporteur
Dr C. Hidalgo, rapporteur
Dr J. Snipes, rapporteur

ÉCOLE POLYTECHNIQUE
FÉDÉRALE DE LAUSANNE

Suisse
2009

Table of Contents

Abstract

This Thesis addresses the interaction of a supra-thermal ion beam with turbulence in the simple magnetized toroidal plasma of TORPEX.

The first part of the Thesis deals with the ohmic assisted discharges on TORPEX. The aim of these discharges is the investigation of the open to closed magnetic field line transition. The relevant magnetic diagnostics were developed. Ohmic assisted discharges with a maximum plasma current up to 1kA are routinely obtained. The equilibrium conditions on the vacuum magnetic field configuration were investigated.

In the second part of the Thesis, the design of the fast ion source and detector are discussed. The accelerating electric field needed for the fast ion source was optimized. The fast ion source was constructed and commissioned. To detect the fast ions a specially designed gridded energy analyzer was used. The electron energy distribution function was obtained to demonstrate the efficiency of the detector.

The experiments with the fast ion beam were conducted in different plasma regions of TORPEX. In the third part of the Thesis numerical simulations are used to interpret the measured fast ion beam behavior. It is shown that a simple single particle equation of motion explains the beam behavior in the experiments in the absence of plasma. To explain the fast ion beam experiments with the plasma a turbulent electric field must be used. The model that takes into account this turbulent electrical field qualitatively explains the shape of the fast ion current density profile in the different plasma regions of TORPEX. The vertically elongated fast ion current density profiles are explained by a spread in the fast ion velocity distribution. The theoretically predicted radial fast ion beam spreading due to the turbulent electric field was observed in the experiment.

Keywords: TORPEX, experiment, plasma, fast ion beam, fast ion source, gridded energy analyzer, ohmic assisted discharge

Version abrégée

Cette thèse aborde la question de l'interaction d'un faisceau d'ions suprathermiques avec la turbulence dans le plasma simple magnétisé toroïdal de TORPEX.
La première partie de la thèse porte sur les décharges ohmiques assistées sur TORPEX. L'objectif de ces décharges consiste à étudier la transition de la ligne de champ magnétique ouverte à la ligne fermée. Les diagnostics magnétiques correspondants ont été développés. Des décharges ohmiques assistées avec un courant plasma maximal jusqu'à 1kA ont été couramment obtenues. Les conditions d'équilibre sur la configuration du champ magnétique sous vide ont été étudiées.
Dans la deuxième partie de la thèse, la conception de la source et du détecteur d'ions rapides est examinée. Le champ électrique d'accélération de la source d'ions rapides a été optimisé. La source d'ions rapides a été construite et mise en service. Pour la détection des ions rapides, un analyseur d'énergie à grille spécial a été utilisé. Afin de démontrer l'efficacité du détecteur, la fonction de distribution énergétique des électrons a été obtenue.
Les expériences utilisant le faisceau d'ions rapides ont été menées dans les différentes régions du plasma de TORPEX. Dans la troisième partie de la thèse, le comportement du faisceau des ions rapides est interprété à l'aide de simulations numériques. Il est démontré qu'un simple équation du mouvement d'une particule seul explique le comportement du faisceau dans les essais sans plasma. Pour interpréter les essais avec plasma, il est nécessaire d'utiliser le champ électrique turbulent. Le modèle qui tient compte de ce champ électrique turbulent explique qualitativement la forme du profil de densité de courant des ions rapides dans les différentes régions de TORPEX. L'extension verticale du profil de densité de courant des ions rapides s'explique par l'écart dans la distribution de vitesse des ions rapides. Le déploiement radial du faisceau des ions rapides à cause du champ électrique turbulent anticipé dans la théorie a été effectivement observé pendant l'expérience.

Mots-clés: TORPEX, expérience, plasma, faisceau d'ions rapides, source d'ions rapides, analyseur d'énergie à grille, décharge ohmique assistée

Chapter 1

Introduction and motivation

The plasma of ITER [1] and future thermonuclear reactors will be heated by the by-products of thermonuclear reactions, alpha particles with very high energy, 3.5MeV, in other words by fast, or supra-thermal, ions. These supra-thermal ions will carry large amounts of power, 200MW for a fusion power of 1GW. In existing tokamaks [2][3], fast ions can be generated by additional ion heating neutral beam injection or ion cyclotron heating [4] or even electron heating [5]. Highly energetic ions can exert a strong influence on plasma properties, such as temperature and density profiles, turbulence, and equilibrium, via direct heating, by exciting instabilities, for example Alfvén frequency modes, or by interacting with existing instabilities e.g., sawteeth [6]. A very important question related both to the basics physics of turbulence and to the problem of anomalous, i.e. non-collisional, transport of these ions is how low-frequency plasma turbulence influences fast ions and, in turn, how fast ions can influence turbulence.

The interaction of fast ions with turbulence has not been extensively investigated to date. One of the reasons is that, in the present tokamaks, the fast ions do not play a crucial role, as it will be the case on ITER. The other more fundamental reason is that, as the fast ions usually have a gyroradius that is larger than the turbulence scale, their interaction with turbulence was expected to be very weak [7][8]. For example, on TFTR it was shown that the typical alpha gyroradius is a factor of 5 larger than the turbulence correlation length [9]. Gyro-averaging effects would than weaken or almost entirely suppress the interaction of alphas with turbulence. The results in [10] indicate that significant diffusive redistribution of supra-thermal ions is driven by turbulence. However, no direct measurements of fluctuation-induced fast ion transport on toroidal devices have been performed so far [11].

A number of theoretical works have attempted to quantify this effect of averaging over the gyromotion [12][13][14][15][16], concluding that interaction of fast ions with turbulence is reduced when the gyroradius is increased. However, several other authors found than when the gyroradius increases up to the fluctuation correlation length, the fast ion transport could remain unchanged [17] or even increase [18][19]. In [20][21], it was found that in some conditions the turbulence can indeed significantly affect the fast ion transport. In particular, it was shown that orbit averaging is not valid at moderate or high magnetic shear [22][23]. In [24], it was found that for typical parameters in ITER the fast ion transport can be driven at significant levels by core turbulence. On the other hand, in [25] the interaction between fast ions and turbulence is found to be negligible.

Thus, the interaction of fast ions with the turbulence remains an open question. Both the mechanisms and the significance of this interaction should be investigated. In particular, there exists a strong need for experimental data with which to compare and validate the relevant theoretical and numerical models. An experimental investigation of the fast ion beam interaction with turbulence is undertaken in the TORoidal Plasma EXperiment [26] TORPEX offers a relatively simple experimental environment with easy access for diagnostics, and a well understood background of drift-wave and interchange instabilities and turbulence [27][28][29][30][31][32].

Specific goals of this Thesis include the development of a miniaturized fast ion source and detector, an exploration of the closed tokamak-like magnetic field line configuration on TORPEX, and, most importantly, an assessment of the fast ion transport in interchange turbulence. This could be done over different poloidal plasma regions, where the predominant effect is the wave-like propagation of the unstable mode or the dynamics of isolated filament-like structures (blobs).

The Thesis starts with a general description of the TORPEX experimental setup. The magnetic system is described in detail, as it is important for understanding the constraints relative to the ohmic assisted discharge development. We include also the description of the most used diagnostics on TORPEX for this work.

In the third Chapter, the ohmic assisted discharge developments are presented, including the design and fabrication of dedicated magnetic diagnostics. The initial ohmic system had relatively large parasitic poloidal magnetic field. The conditions for plasma equilibrium are discussed and the tests of improved configurations are illustrated.

Two versions of the fast ion source were developed. Both of them use aluminosilicate lithium ion emitters. The design of the fast ion sources was optimized to have a homogeneous electric field. Most of the constraints (e.g. maximum ion current, life time) are defined by the emitter. Extensive tests of the emitters were performed on a dedicated test-bench. A 2D poloidal moving system was developed for the source to be able to place it practically in any poloidal position of TORPEX. These specific developments are described in Chapter 4.

Chapter 5 illustrates the design of the fast ion detector, based on a double gridded energy analyzer. To show the capability of the detector, we measure the electron energy distribution function at several radial positions. We demonstrate that most of the fast electrons are localized near the electron cyclotron and lower hybrid resonances, where they are accelerated by microwaves and ionize the neutral gas.

The theoretical background for the fast ion beam experiment on TORPEX is presented in Chapter 6. To analyze experimental data, two simulation packages were developed. These packages, based on a Matlab and on a C++ platform are described in Chapter 7. Both models are based on the single particle equation of motion. The Matlab based model takes into account the collisions of fast ions with background plasma ions. The main feature of the C++ based model is that it accounts for the turbulent electric field obtained from a fluid code, specifically constructed for a quantitative description of turbulent phenomena in TORPEX. The benchmark of the two models is also presented.

In Chapter 8, we present the fast ion beam experiments. First of all, we describe the experiments with magnetic fields but no plasma to establish the fast ion beam behavior. Next, we deal with the experiments with the fast ion beam injected in the blob region, where

the structures with higher plasma pressure are present, for two fast ion energies, 300eV and 600eV. The experiments in the mode region, where the density fluctuations are dominated by coherent oscillations, are conducted with a fast ion energy of 300eV. Conservation of the fast ion current along the fast ions path in the plasma is experimentally verified.

The results of the simulations presented in Chapter 9 help us understand the experimental data. The Matlab based model qualitatively explains the propagation of the fast ion beam in the absence of plasma. In the presence of plasma, it is necessary to introduce the turbulent electric field, thus the C++ based model was used for the simulation of these experiments. The results of the simulations are in qualitative agreement with the experiment, in particular in terms of the main expected effect of the turbulence, i.e. a broadening of the fast ion beam radial profile. However, we conclude that for better agreement, for example on the location and full shape of the fast ion beam profile, more realistic turbulent electric fields and fast ion energy distributions should be used, as discussed in Chapter 10.

Chapter 11 concludes the Thesis and discusses the issues that should be addressed in future activities along the research avenue opened by this work.

Chapter 2

The TORPEX device

The TORoidal Plasma EXperiment (TORPEX) device (Fig.2.1) is a toroidal plasma machine dedicated to basic plasma physics studies [26], which started operation in 2003 at CRPP-EPFL, Lausanne. The primary goal of TORPEX is the investigation of turbulence, plasma instabilities and transport in a simplified environment relative to the tokamak configuration. The low plasma temperature and density of TORPEX allows easy access by diagnostics.

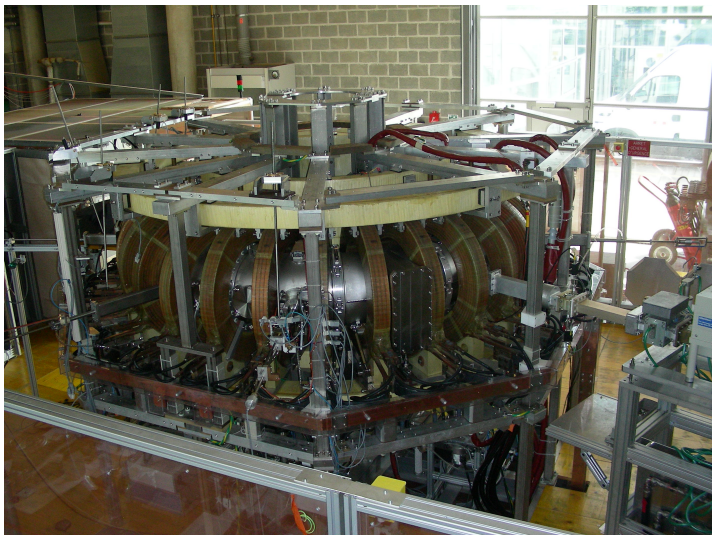

Figure 2.1: The TORPEX device.

2.1 General description

The vacuum chamber of the TORPEX device has a major radius 1 m, a minor radius 0.2 m. One of the TORPEX features is the presence of movable sectors: there are four sectors in

the vacuum chamber, which can be dismounted completely to have even greater access for the installation of new diagnostics. For example, for the new experiment [33], the steel limiter plate mounted on the ring, which is only a few centimeters less than the diameter of the vacuum chamber, was installed in the movable sector.

The TORPEX device has 28 toroidal magnetic coils, which can produce a toroidal magnetic field up to 0.1T on the axis (Fig.2.2). The poloidal magnetic field can be produced by 10 coils (Fig.2.3) that can be connected in an almost arbitrary way. The configuration with B1, B2, C1 and C2 coils connected in series is used to produce an almost homogeneous vertical field, up to 5mT. For the ohmic discharges, the original configuration uses D1, D2, E1 and E2 coils connected in series.

The most used gases for plasma are hydrogen and argon. The typical average electron temperature is 5eV for both hydrogen and argon plasmas, with average electron densities $3\times10^{16}m^{-3}$ for hydrogen and $2\times10^{17}m^{-3}$ for argon. With addition of ohmic power the density can rise up to $2\times10^{18}m^{-3}$. These low temperatures and densities allow highly localized measurements of plasma parameters with sets of different probes inserted directly in the plasma core. More than 300 channels can be acquired simultaneously during the whole discharge, with a sampling rate of 250 kHz.

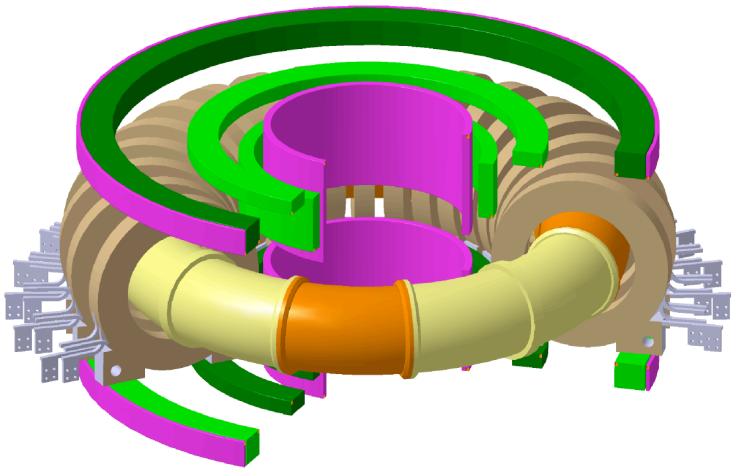

Figure 2.2: The TORPEX coils.

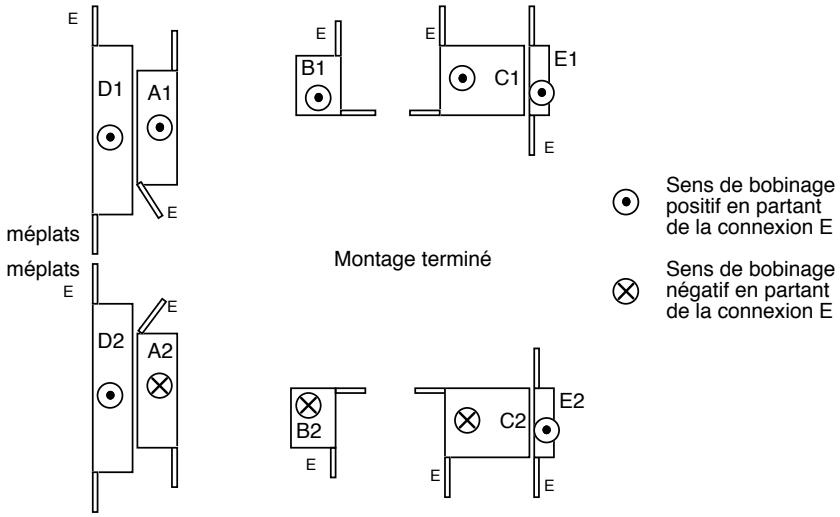

FIG. 2.3. Schematics of the TORPEX magnetic coils that produce poloidal magnetic field.

2.2 Vacuum and gas injection systems

The vacuum system of TORPEX consists of the four turbo-pumps, backed by four primary pumps. The pumping is carried out through four equidistantly separated in toroidal direction flanges. The vacuum inside the vessel is about 3×10^{-7}mbar. The separate primary pump is used for differential pumping of the probe movable systems. The vacuum in this line is maintained at 5×10^{-3}mbar. The gas injection system can puff the gas in one toroidal position with the rate controlled by flow-meter. The commonly used gases include Hydrogen, Argon, Neon, Nitrogen, Helium, and Deuterium.

2.3 Plasma production

The plasma of TORPEX can be produced by one of two magnetron sources. Both magnetrons used ordinary mode microwaves at frequency 2.45GHz. The electron cyclotron resonance for this frequency corresponds to a toroidal field of 87.5mT.

The first magnetron launches microwaves from the low field side. The maximum power of this magnetron is 30kW in the pulse mode for duration up to 100ms and 5kW in continuous mode operation. The electronics of this magnetron allows using arbitrary waveforms for the

magnetron power. The disadvantage of this magnetron is the existence of a minimum possible value of injected microwave power (200W). The microwave power lower than 200W should be used to produce weakly turbulent plasmas. To overcome this problem a second magnetron, which does not have this limitation, was installed on TORPEX. The second magnetron launches microwaves from the bottom of the machine. It works only in continuous mode and can deliver microwave power up to 1.2kW.

2.4 Diagnostics

There are numerous diagnostics on TORPEX: different arrays of Langmuir probes, gridded energy analyzers, Mach probes, Mirnov coils, Rogowskii coils and fast visible camera. The two most used diagnostics for this work, besides the fast ion detector that is described separately, are the arrays of Langmuir probes: HEXTIP and SLP.

2.4.1 HEXTIP - HEXagonal Turbulent Imaging Probe

The HEXTIP is a two-dimensional Langmuir probe array [34], consisting of 86 tips, which cover the entire poloidal cross-section (Fig.2.4). HEPXTIP is mainly used for measurements of density and floating potential profiles. The HEXTIP electronics bandwidth of 20kHz is enough for the turbulence study on TORPEX. The spatial resolution is 3.5cm.

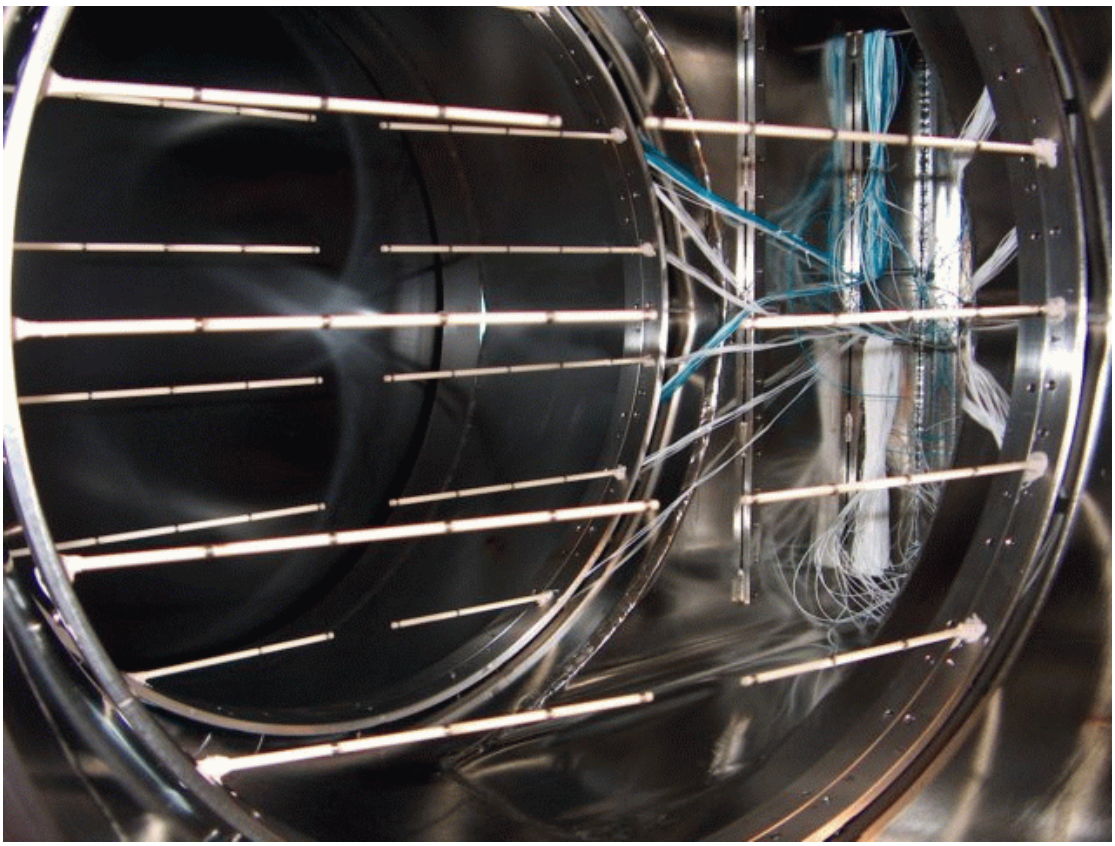

Figure 2.4: HEXTIP.

2.4.2 SLP – Slow Langmuir Probe

The SLP is a one-dimensional probe array consisting of 8 tips separated by 1.8cm [35]. This diagnostic is mounted on a movable system, which allows placing SLP at different poloidal positions. Moving the probe discharge by discharge one can fully reconstruct the density, temperature and plasma potential profiles with practically arbitrary good spatial resolution. The time resolution of SLP is about 0.5ms.

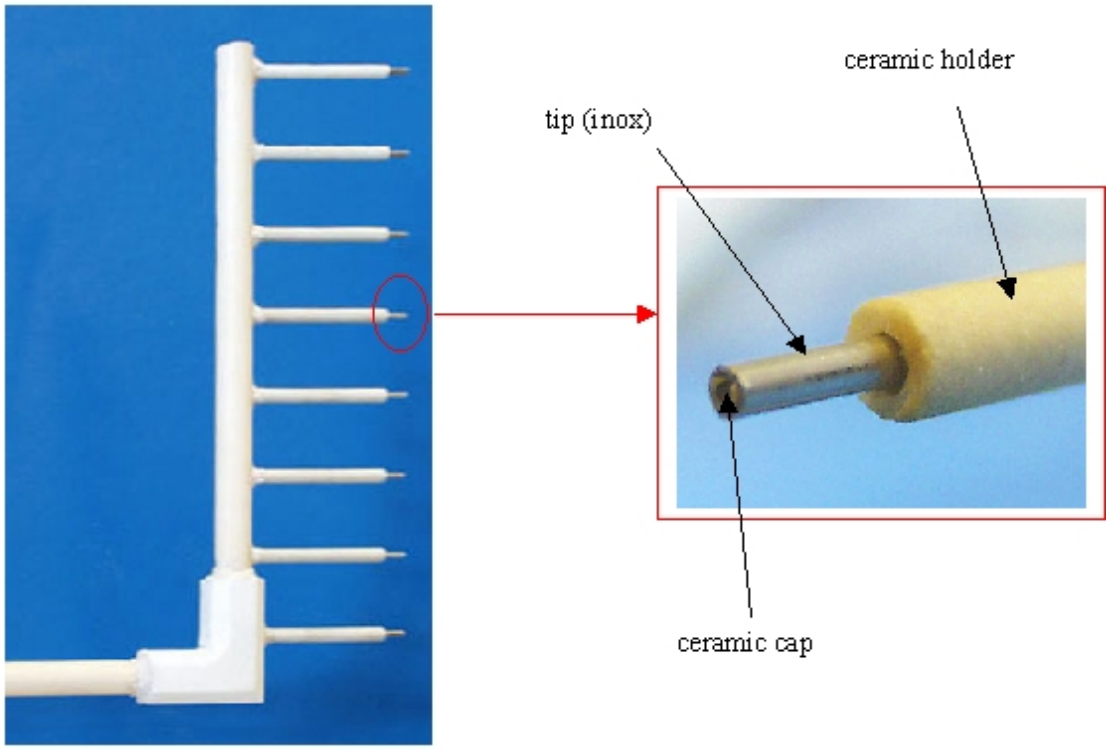

Figure 2.5: SLP.

2.5 IT system

The MDSplus [36] system is used for the data-management. The data acquisition system consists of a D-tAcq dt200 digitizer [37] and two D-tAcq dt196 digitizers [38], one of them is dedicated for the HEXTIP data. Each of these digitizers acquires 96 channels at 250kHz. A Linux based PC with a hardware RAID5 controller, providing a disk capacity of 750Gb, stores all experimental data. This data can be easily retrieved with Matlab. To prevent the loss of data, incremental backups take place daily and full backups once a week.

A BITBUS [39] server-slave based instrument-control system is chosen to be used for TORPEX. Using a graphical user interface, which is installed on the dedicated PC, the user can set values, which are then written to the hardware through BITBUS. The graphical user interface is written in Java with the system configuration stored in XML format. There is one XML file for each device. Thus, to add a new device a new XML file should be written. This system allows relatively easy implementation of new hardware for TORPEX.

Chapter 3

Ohmic system

The TORPEX ohmic system was designed to reach a regime in which TORPEX plasmas can be created and confined within closed magnetic field surfaces. The ohmic system includes magnetic coils that induce a current in the plasma, the power supply for these coils and the diagnostics for the measurement of the plasma current and the magnetic field. Initially, only coils D1, D2, E1, E2 were employed for the ohmic system (Fig.2.3). However, with a current in a coil under 2000A during 60ms, any of the vertical coils can be used for the ohmic assisted discharges.

The power supply used here can deliver up to 4000A, with a ramp up speed of approximately 100A/ms. Another, more powerful capacitor based power supply (625μF, 20kV) is under development. It will allow obtaining a loop voltage of the order of 100V.

3.1 Diagnostics

A dedicated set of diagnostics was developed for the ohmic discharges. These include diagnostics for loop voltage measurements, large rogowskii coils for total plasma current measurements and small mobile rogowskii coils for current density profile measurements.

3.1.1 Loop voltage measurements

The diagnostic for the loop voltage measurements consists of a single toroidal turn wire. This wire is placed between the toroidal coils and the vacuum chamber. This loop encloses

almost the entire magnetic flux from the ohmic coils. The typical loop voltage on TORPEX is of the order of 6V, so the signal can be acquired directly without any additional signal conditioning electronics.

An example of the signal from this diagnostic is presented in Fig.3.1. During the ramp up phase of the current in the ohmic coils the loop voltage has a sawtooth structure due to the characteristics of the power supply.

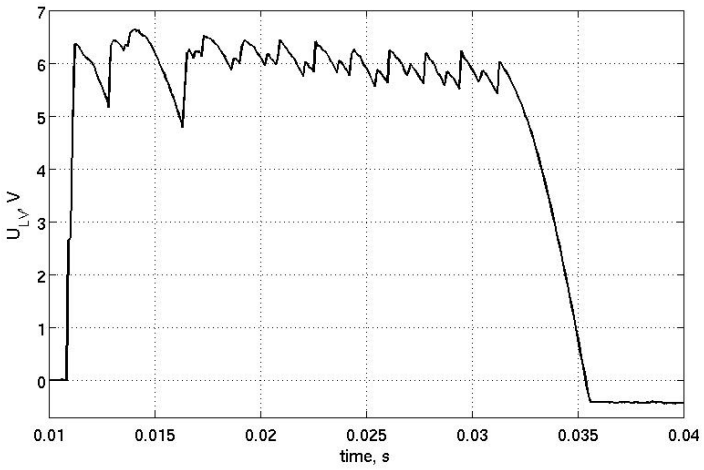

Figure 3.1: Example of the loop voltage measurements during an ohmic discharge on TORPEX.

3.1.2 Rogowskii coils

Two rogowskii coils are used to measure the total plasma current [40]. One is installed inside the vacuum chamber (Fig.3.2) and one is placed outside (Fig.3.3). The internal rogowskii coil is made of four windings, which allows estimating the position of the plasma column. The external rogowskii coil has only one winding, but its location allows easier manipulation. Both diagnostics were calibrated outside of the TORPEX device and feature a flat frequency response up to 30kHz. The calibration factors for the internal and external rogowskii coils are equal to 1.27×10^5A/V and 1.09×10^5A/V, respectively. It was verified that no significant time delay exists between the two rogowskii coils due to the stainless steel vacuum chamber that is in between.

The typical signal from these coils is of the order of several millivolts. Two amplifiers with a gain up to 10000 are used for both diagnostics. The amplified signal is integrated with a 6.3ms integration time. Both the nonintegrated and integrated signals are acquired, so that one can check that the nonintegrated signal is not saturated and perform the integration numerically if needed. The electronics allows an accuracy for both rogowskii coils that corresponds to approximately ±10A of plasma current.

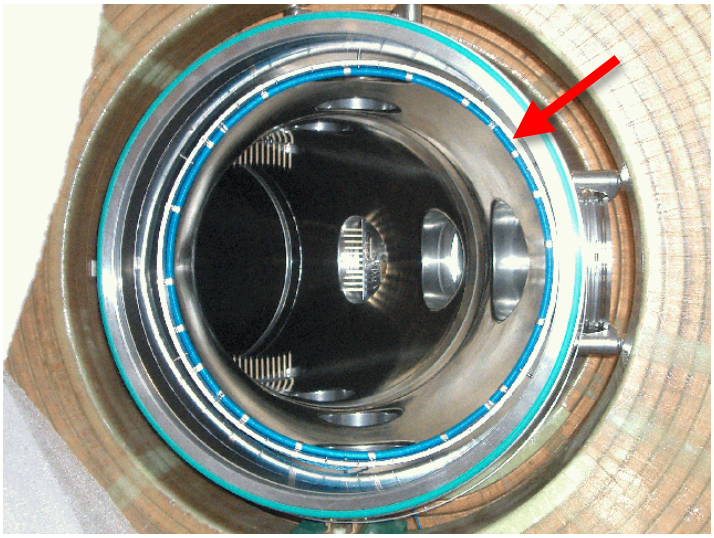

Figure 3.2: Rogowskii coil installed inside the vacuum chamber.

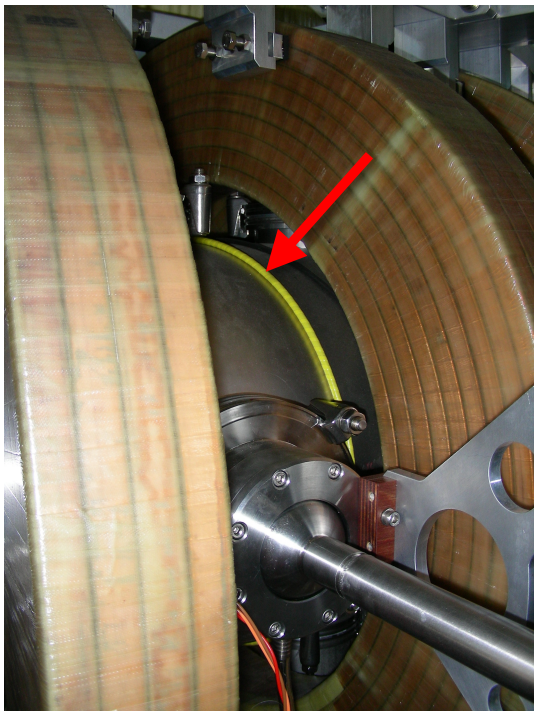

Figure 3.3: Rogowskii coil installed outside the vacuum chamber.

3.1.3 Mobile rogowskii coils

The small and mobile rogowskii coils were constructed to obtain local measurements of the plasma current. These rogowskii coils were installed on a probe positioning system that could move the probe to practically any point of the plasma poloidal cross section. Thus from shot to shot one can measure the local current in different poloidal points and construct the 2D plasma current density profile. The first rogowskii coil (Fig.3.4) has a diameter of 3cm and a thickness of 0.7cm. The cut-off frequency (3kHz) is low because of the large numbers of turns, 3000 (the diameter of the wire is 0.05mm). The calibration factor is equal to 3.30×10^{6}A/V.

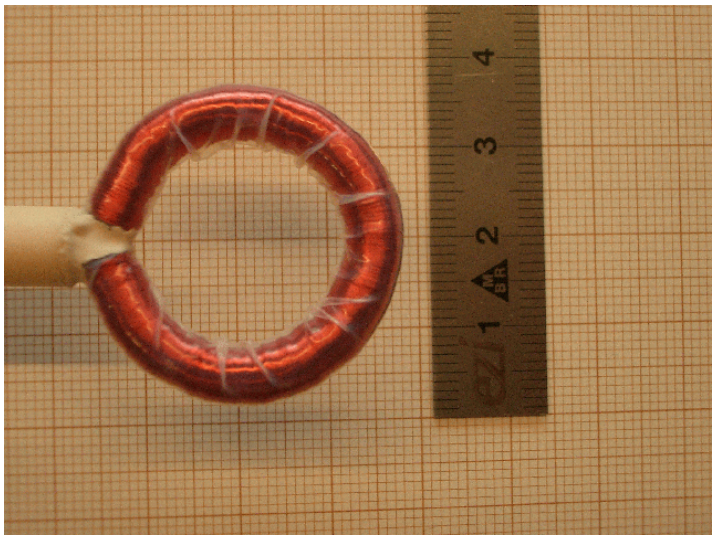

Figure 3.4: First mobile rogowskii coil.

The second mobile rogowskii coil (Fig.3.5) has larger dimensions (diameter ~6cm and thickness ~0.8cm). This modification allowed us to increase the linear response up to frequency of 10kHz. The calibration factor for this rogwskii coil is equal to 2.37×10^{6}A/V. This coil has noncircular shape. Measurements of the current through a wire located in different places within the rogowskii coil were conducted to estimate the errors deriving from a noncircular shape. In Fig.3.5 the current measured with the rogowskii coil in these experiments relatively to the current measured when the wire located at the center of the coil is shown. As it can be seen, the effect of a noncircular shape is practically negligible.

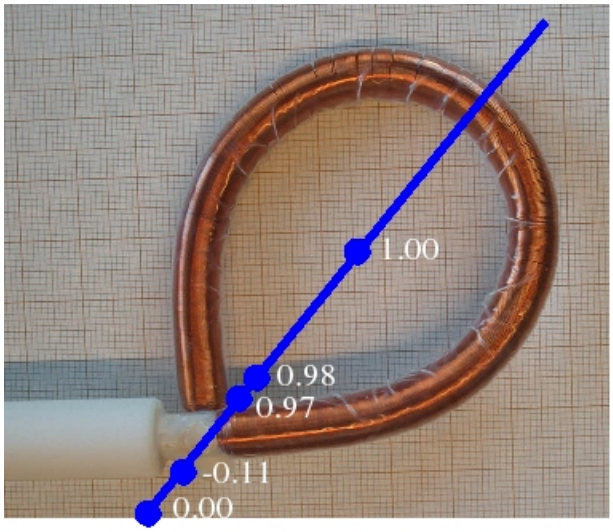

Figure 3.5: Second mobile rogowskii coil. The relative signal measured by this rogowskii coil, when the wire with the current situated in the different position within the coil is presented.

3.2 Original configuration

The original ohmic coil configuration is based on the D1, D2, E1, E2 coils connected in series. These coils produce the poloidal magnetic field in the vacuum chamber shown in Fig.3.6. This field has an X point and a maximum on the high field side. As the plasma has diamagnetic properties this magnetic field pushes out the plasma column toward the low field side.

An example of a time trace of the plasma current and the loop voltage measured in this configuration is presented in Fig.3.7. Although different plasma conditions were used, the duration of the plasma current channel remained almost unchanged. In this experiment the plasma was lost on the wall of the vacuum chamber. With the help of HEXTIP data we determined that in these experiments the plasma column moves from the high field side to the center and subsequently downward to the wall. This result was confirmed by measurements made with the mobile rogowskii coil (Fig.3.8).

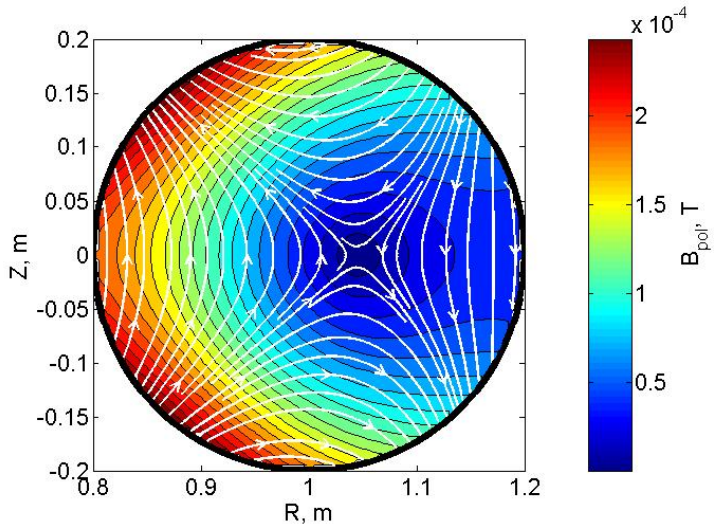

Figure 3.6: Poloidal vacuum magnetic field induced by ohmic coil for the coil current 300A (the color scale shows the absolute value of the field in [T] for the 100A current in the ohmic coils).

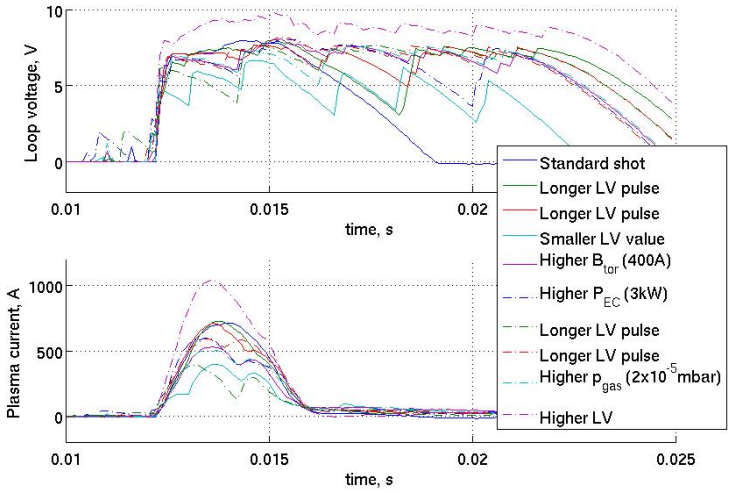

Figure 3.7: Time traces of the plasma current and the loop voltage for different conditions: different lengths of the loop voltage pulse, different values of the loop voltage, different toroidal fields, different injected microwave power, different gas pressures. The conditions are those of the standard shot: the Argon pressure is 1.3×10^{-5}mbar, the microwave power 1kW, and the toroidal field is 72mT.

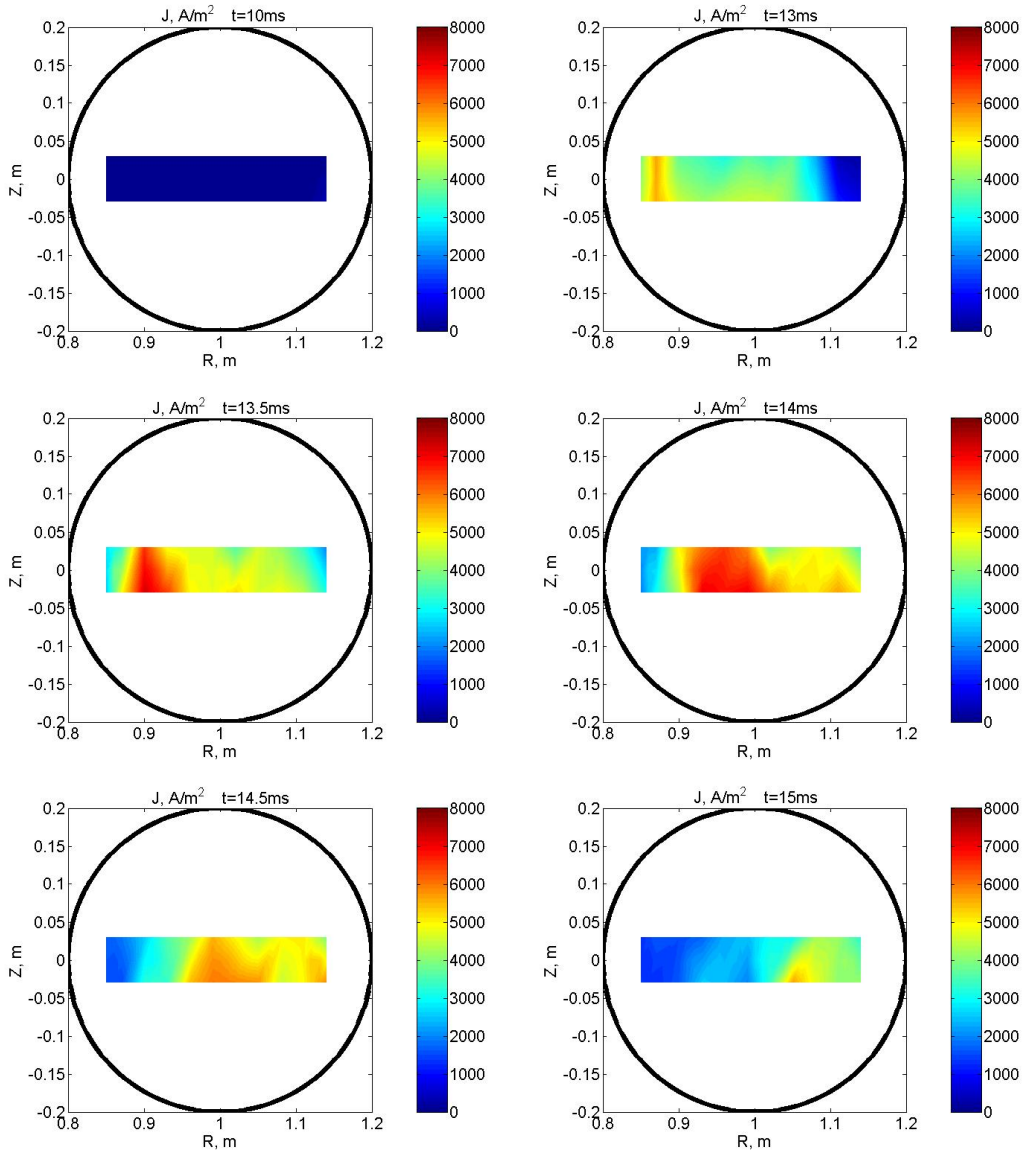

Figure 3.8: Current density profile in [A/m^2] for the time of 10, 13, 13.5, 14, 14.5 and 15ms measured by the mobile rogowskii coil in the same conditions as the standard shot in Fig.3.7.

It is important to stress that, during the stable phase (lasting around 1.2ms), the estimated total poloidal magnetic field has closed magnetic field lines (Fig.3.9).

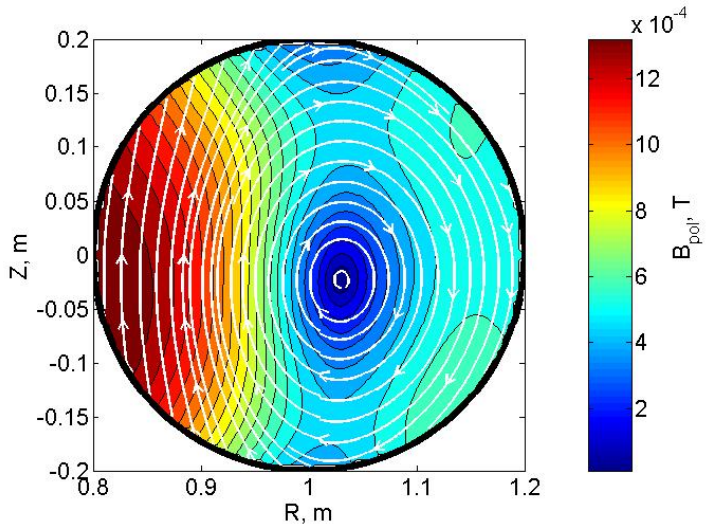

Figure 3.9: Calculated total poloidal magnetic field in [T], using the assumption that the current density profile is proportional to the density profile, which was measured with HEXTIP in the same conditions as the standard shot shown in Fig.3.7.

To optimize the duration of the current channel in these discharges, vertical magnetic field coils were used. In principle, the value of the stabilizing magnetic field depends on the plasma current. Here, for simplicity, a constant magnetic field, irrespective of the plasma current, was used. Experiments showed (Fig.3.10 and 3.11) that negative vertical field (directed downward) has a stabilizing effect on the plasma column. But when the duration of the plasma column increases, the value of the maximum total plasma current decreases.

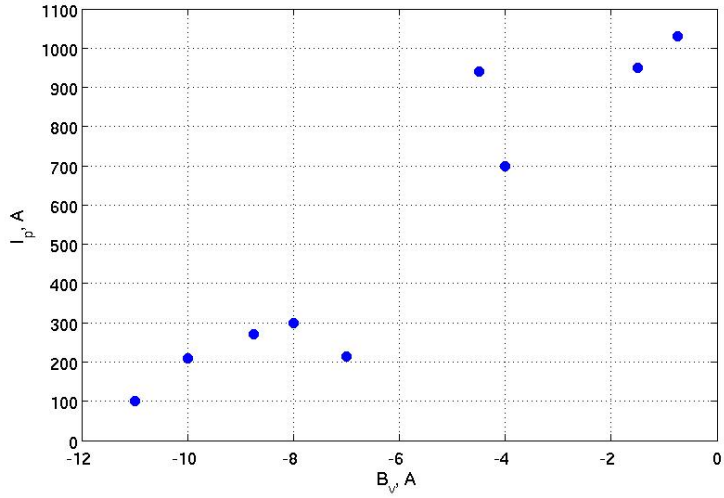

Figure 3.10: Maximum plasma current value as a function of vertical magnetic field measured in the same conditions as the standard shot in Fig.3.7.

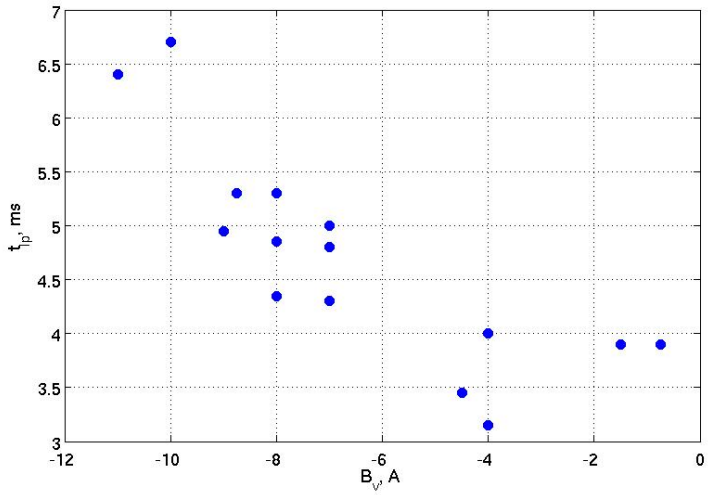

Figure 3.11: Duration of the plasma current channel as a function of the vertical magnetic field measured in the same conditions as the standard shot in Fig.3.7. The duration is defined as the length of the time window when the current measured by the large rogowkii coil is higher than 10A.

3.3 Plasma equilibrium in a tokamak-like configuration

There are at least three reasons why the plasma column tends to increase its major radius and move to the outer wall of the tokamak [41]. First of all, the plasma has diamagnetic properties, which make it tend to go to the low field side, due to charge separation and the $\vec{E} \times \vec{B}$ drift. Second, the plasma torus has pressure, which tends to increase its major and minor radius. Third, the plasma torus is a turn of a conductor with a relatively high current, so it tends to increase his conductance by increasing the major radius.

In order that the plasma column be maintained in equilibrium with a help of approximately homogeneous magnetic field perpendicular to the toroidal plane, this field should have a certain value and curvature [42]:

$$B_{\perp 0} = \frac{\mu_0 I_p}{4\pi R_p}\left(\ln\frac{8R_p}{a} + \Lambda - \frac{1}{2}\right)$$

where μ_0 is the permeability of free space, I_p is the plasma current, R_p and a are the major and minor radii of the plasma column, Λ is the coefficient of asymmetry of the poloidal

field determined by the formula:

$$\Lambda = \frac{8\pi\langle p\rangle}{B_I} + \frac{l_i}{2} - 1$$

where the angle brackets denote averaging over the plasma cross-section; p is the plasma pressure, B_I is the field of the current flowing in the plasma and l_i is the internal inductance of the unit length of the column. The curvature of the vacuum vertical field is quantified by the decay index: $n = -\frac{r}{B_\perp}\frac{dB_\perp}{dr}$. For equilibrium the decay index should comply with the inequality $0 < n < \frac{3}{2}$. The first condition, implying positive decay index, leads to the poloidal magnetic field curved outwards of the main axis. This is the condition of the equilibrium position of the plasma relative to the vertical displacement. When the curvature of the field is high, the poloidal magnetic field decreases strongly from the high field side to the low field side. This is an unfavorable situation for the plasma equilibrium relative to the horizontal displacement, thus one need the second condition, $n < \frac{3}{2}$, that limits the curvature of the field.

According to these formulas for equilibrium, the vacuum poloidal magnetic field should point downwards and have a value of the order of 0.1mT for a plasma current of 1kA.

3.3 Improved configurations

We consider the initial configuration (Fig.3.6) from the point of view of plasma equilibrium, as discussed above. The direction of the poloidal field is incompatible with equilibrium on the low field side, and the curvature is incompatible with equilibrium on the high field side. Thus the plasma column is not in equilibrium with respect to a horizontal displacement on the high field side and with respect to a vertical displacement on the low field side. This can also be proven on the basis of the decay index profile (Fig.3.12).

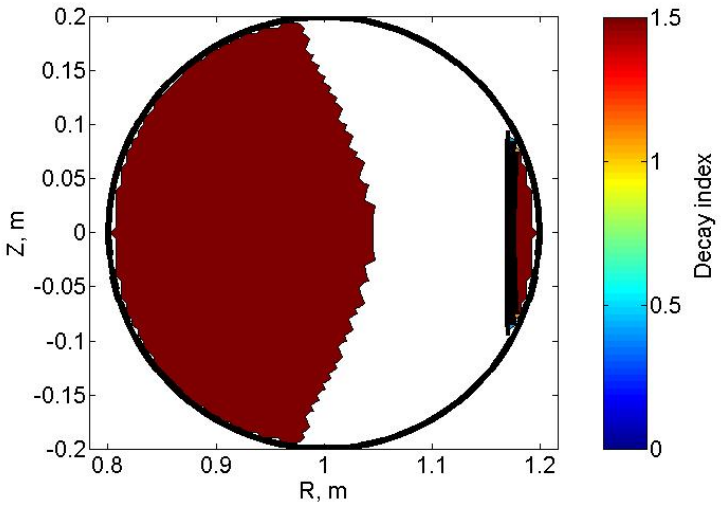

Figure 3.12: Decay index profile for the original ohmic coil configuration (brown means that the decay index is above 1.5 and white that the decay index is negative).

To improve the equilibrium, a coil configuration providing the correct magnetic field direction, curvature and value should be found.

A second configuration that was tested uses coils A1, A2, E1, E2 (Fig.3.13). The advantage of this configuration is that it provides the right magnetic field and curvature direction. On the other hand, the value of the magnetic field is one order of magnitude higher than it should be for the equilibrium. As a consequence, the plasma column is squeezed to the high field side.

A third configuration that was tested uses coils D1, D2, A1, A2, C1 and C2 (Fig.3.14). This configuration leads to a complicated magnetic structure, with a minimum magnetic field in the center of the vacuum chamber.

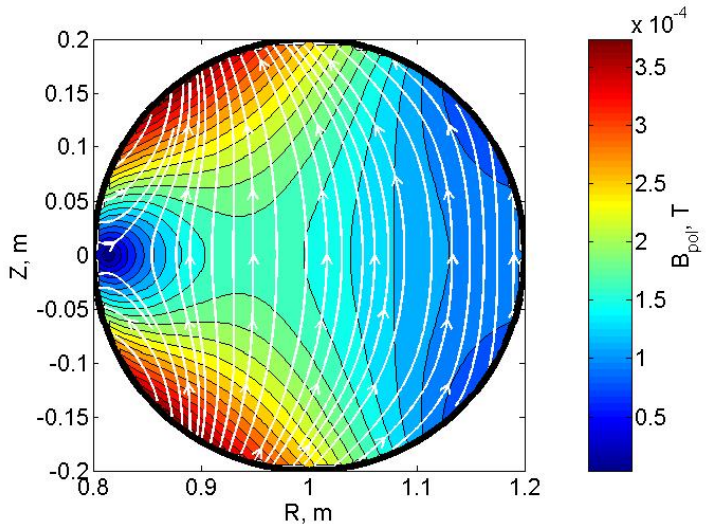

Figure 3.13: Vacuum magnetic field in [T] during the ohmic shot using A1, A2, E1 and E2 coils connected in series with 100A current.

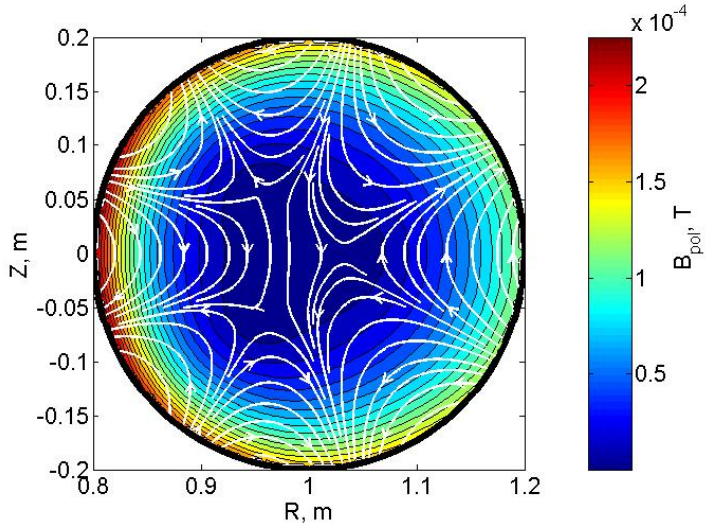

Figure 3.14: Vacuum magnetic field in [T] during the ohmic shot using D1, D2, A1, A2, C1 and C2 coils connected in series with 100A current.

A short (~1ms) stable phase was found in this configuration (Fig.3.15). In the poloidal region, where the plasma column is observed to be stationary, the magnetic field satisfies all conditions for equilibrium.

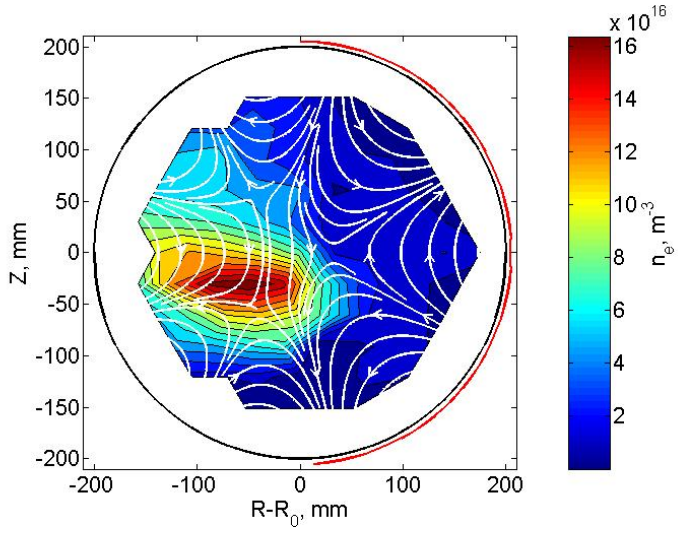

Figure 3.15: Plasma density profile (in [m^{-3}]) in the stationary phase in Hydrogen plasma with a neutral pressure of 6.1×10^{-5}mbar, a toroidal field of 76mT, a microwave power of 1kW and a loop voltage of 7V.

To extend the stable phase of the discharge, the vacuum poloidal magnetic field should satisfy the equilibrium conditions during its entire duration. For this, a second power supply can be used. In [43] the previous configuration (Fig.3.14) was used to minimize the parasitic magnetic field produced by the ohmic coils. A second power supply was connected to the E1 and E2 coils to produce the desired field. The total vacuum poloidal field is presented in Fig.3.16.

Using this complicated configuration, the duration of stable phase of the discharge reached 17ms (Fig.3.17). To further increase it, a system, with feedback control of the current in coils relative to the plasma current, should be used.

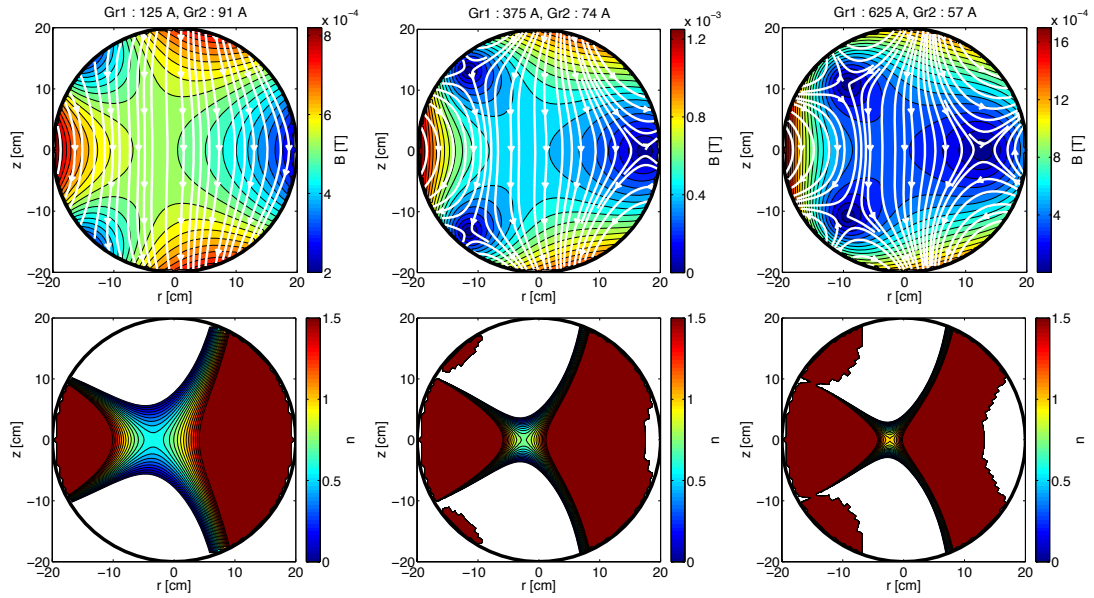

Figure 3.16: Evolution of magnetic field and decay index for three consecutive times during one shot. D1, D2, A1, A2, C1 and C2 coils are referred to as Gr1, E1 and E2 coils are referred to as Gr2.

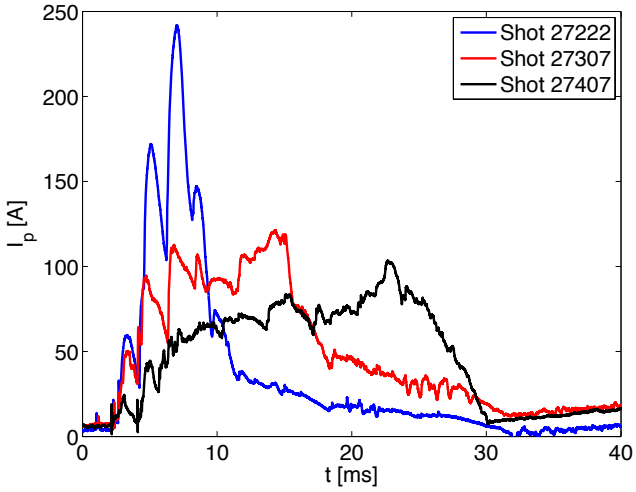

FIG. 50. Time evolution of plasma current for three different currents in the E1 and E2 coils (10A (blue), 70A (red) and 150A (black)).

Chapter 4

Fast ion source

The task to design and build a fast ion source was made challenging by the need to satisfy several constraints: small physical dimensions; a fast ion current higher than 0.5μA; a casing of the source that should be vacuum and plasma compatible; the source should be able to withstand the microwaves present in the plasma; an emitter operates at a temperature about 1100°C, thus all parts should withstand this temperature.

Due to the relatively low energy required (100eV- 1keV), a small cylindrical ion source can be used. Such an ion source can be installed directly inside the TORPEX vacuum vessel [44]. The scheme with a two grid accelerating system with a thermionic emitter [45] was chosen for the fast ion source.

The ion source consisting of two aligned grids (a screen and an accelerating grid), and an ion emitter is schematically presented in Fig.4.1. The screen grid will have the same potential as the plasma to minimize perturbations. The mesh size of this grid should be smaller than the Debye length to prevent penetration of plasma inside the source. The aim of the internal grid is to prevent electrons from reaching the emitter. That is why the potential on this grid is negative and much higher than the electron temperature. The emitter is set at relatively high positive potential (up to 1kV). This potential could be modulated with a frequency up to 10kHz. The modulation of the potential allows synchronous detection of the fast ion beam. The emitted ions in such a configuration have energy equal to the emitter potential minus the external grid potential. By varying the potential on the internal grid, the beam can be focused. The highly negative potential on the internal grid increases the electric field around the emitter, which in turn increases the ion current due to the Schottky effect [46][47][48].

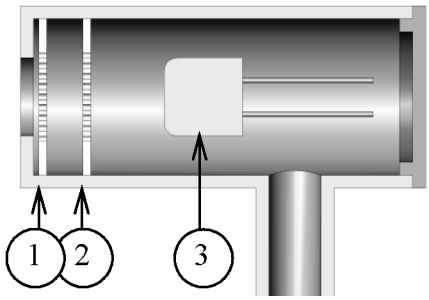

Figure 4.1: Schematics of the fast ion source: (1) external grid; (2) internal grid; (3) emitter.

4.1 Optimization of the electric field inside the source

To maximize the transparency of the accelerating part of the source, the homogeneity of the electric field should be optimized. In fact, an inhomogeneous electric field would lead to fast ion losses inside the source. The electric field optimization was performed in the frame of a collaboration with the University of California at Irvine. The resulting optimized field is shown in Fig.4.2. One of the main features of this optimization is that the emitter was moved as close to the internal grid as possible to increase the electric field in front of the emitter and to make it as homogeneous as possible. Another feature is the smoothing of the edges of the grid supports. In this construction, the grid support edges act as Pierce optics [49][50].

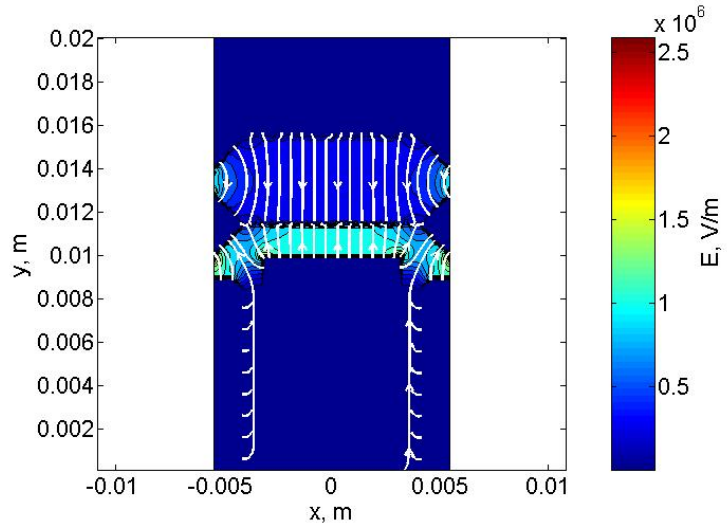

Figure 4.2: Simulated electric field inside the optimized fast ion source (in [V/m]).

4.2 Calculation of the source transparency

In order to estimate the fast ion current one should know the overall transparency of the source. The overall transparency of the source is determined by the transparency of the grids and the transparency of the source itself, which depends on the electrical field inside the source. The results of a simulation calculating this field are shown in Fig.4.3. According to the simulation, the fraction of particles that pass through the source does not depend on the grid structure and mesh size, and is equal to about 0.80. The transparency of the full system is then equal to the transparency of the external grid (0.56) times the transparency of the internal grid (0.74), times 0.80. Thus, only 33% of the emitted ions pass through the source.

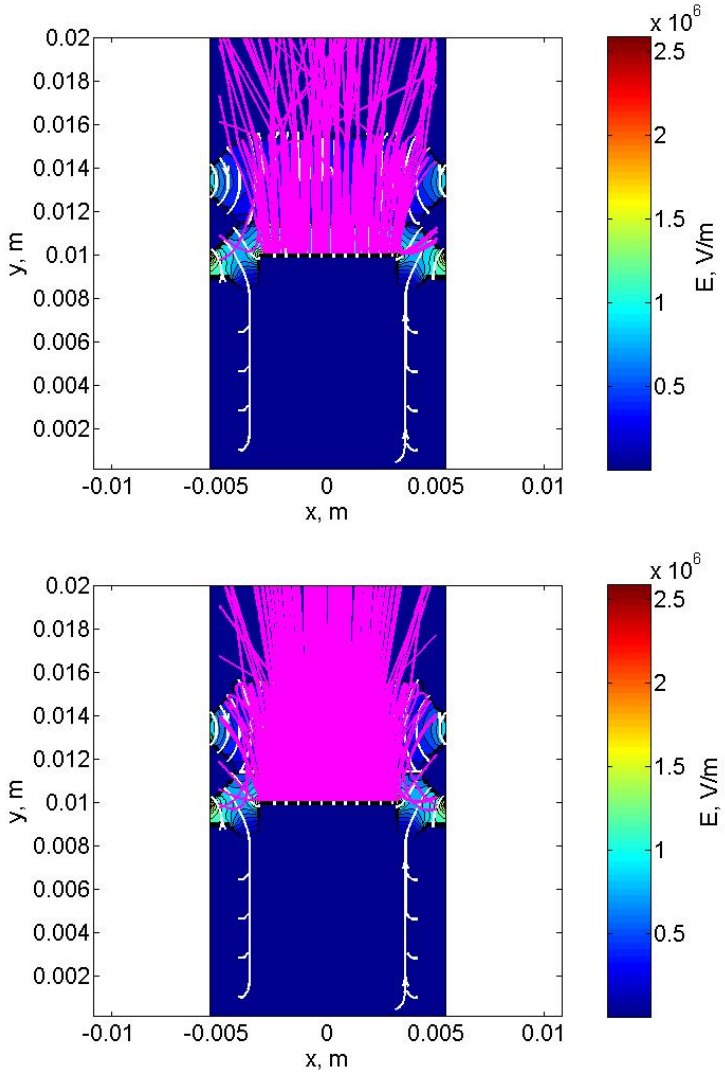

Figure 4.3: Simulated ion trajectories inside the source with the grids (top) and without grids (bottom) (color shows the value of electric field in [V/m]).

4.3 Fast ion source electronics

The electronics for the source consist of three power supplies. The first power supply is for the internal grid, which is set a negative voltage, up to -1kV. The second power supply gives a positive voltage up to 1kV, which could be modulated at a frequency up to 10kHz. The third is used to heat up the emitter, and can deliver up to 16V and 20A.

4.4 Emitter

An aluminosilicate lithium ion emitter was chosen for this experiment (the chemical formula of emitter material is $LiAlO_2SiO_2$) [51]. The advantages of this emitter are a small size, very low gas load and a relative ease to use. The disadvantages are a high operational temperature and a limited lifetime. We used emitters produced by Heat Wave Labs [52][53]. The working principle of the emitter is based on thermionic emission of positive ions from aluminosilicates [54][55].

We used two types of Li-6 emitters. The main difference between them is in the physical dimensions: 0.25inch and 0.6inch diameter Fig.4.4 and 4.5.

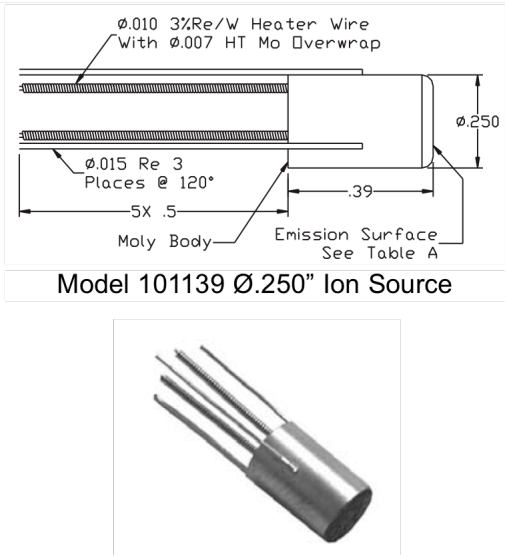

Figure 4.4: 0.25-inch aluminosilicate ion emitter.

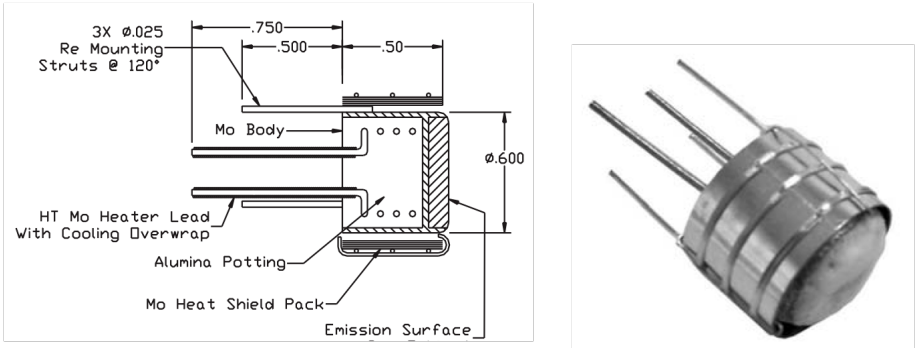

Figure 4.5: 0.6-inch aluminosilicate ion emitter.

A small test bench was especially developed to test these emitters. This consists of a small vacuum chamber kept at a pressure below 10^{-6}mbar. Inside the chamber there is a holder for the ion emitter and a molybdenum collector (Fig.4.6). The distance between the collector and the emitter can be preset in the range from 2 to 15mm. The test bench uses the same electronics as the ion source. The collector is grounded through the ampere meter and the emitter has a positive (repulsive) potential.

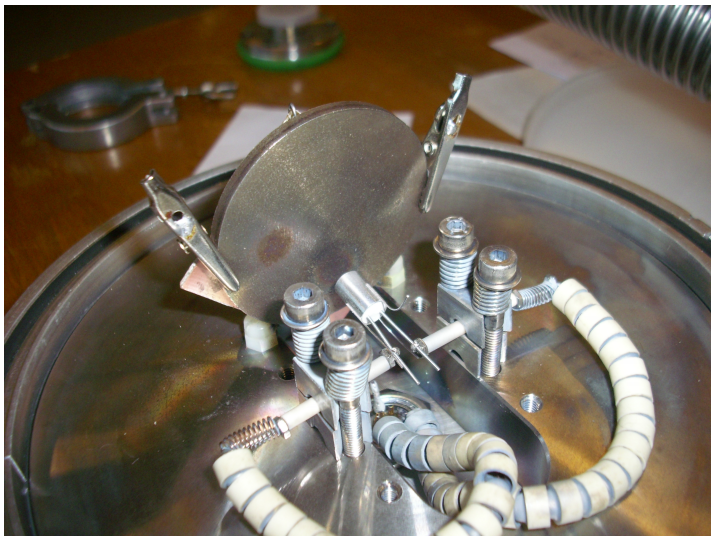

Figure 4.6: The ion emitter mounted on the test bench.

This kind of emitters operates in vacuum, at pressure less than 10^{-5}mbar. To start the emission, the system needs to be heated at a temperature higher than 1100°C. If the emitter is heated quite fast, the adsorbed particles would be released. These particles could be absorbed by the emission surface and the emitter will be poisoned. Thus the heating cycle

must be quite slow. Typically, for its first usage, the emitter is heated from room temperature till 1100°C in about 7 hours, as shown in Fig.4.7. During this heating phase the vacuum pressure is kept lower than 10^{-6}mbar. The ion current depends nonlinearly on the heating power, as shown in Fig.4.8, which was compiled from a large number of experimental tests. When the emitter is heated, it emits light, whose brightness depends on the temperature. Fig.4.9 illustrates the dependence of ion current upon the emitter brightness.

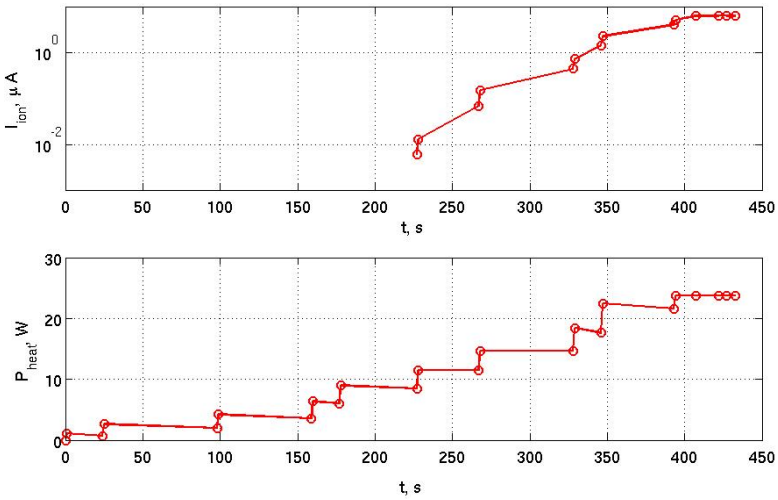

Figure 4.7: Examples of the slow heating of emitter.

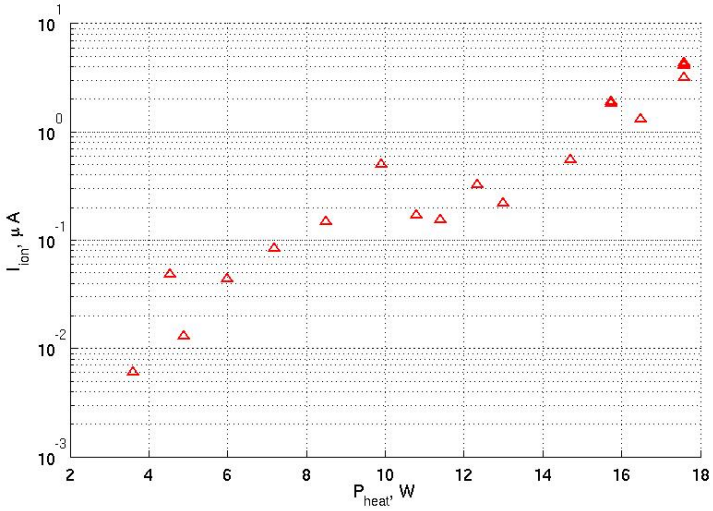

Figure 4.8: Ion current as a function of heating power.

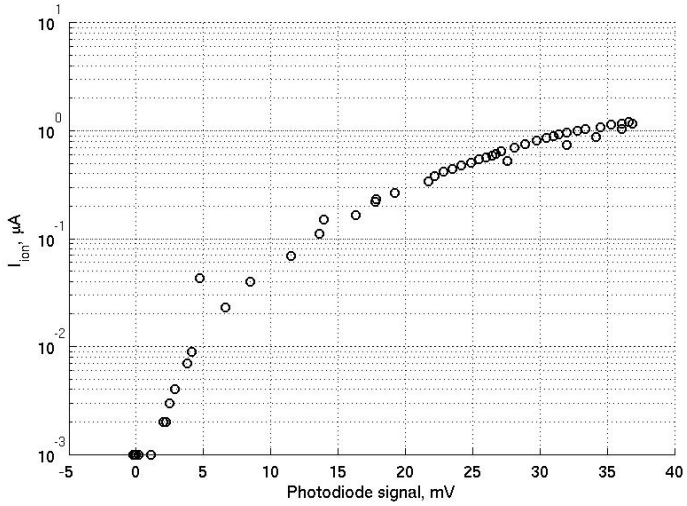

Figure 4.9: The ion current as a function of light intensity emitted by the hot emitter.

The significance of the Schottky effect was checked on the dedicated test bench, Fig.4.10. Due to this effect, when the accelerating voltage is increased in the source, the fast ion current also increases.

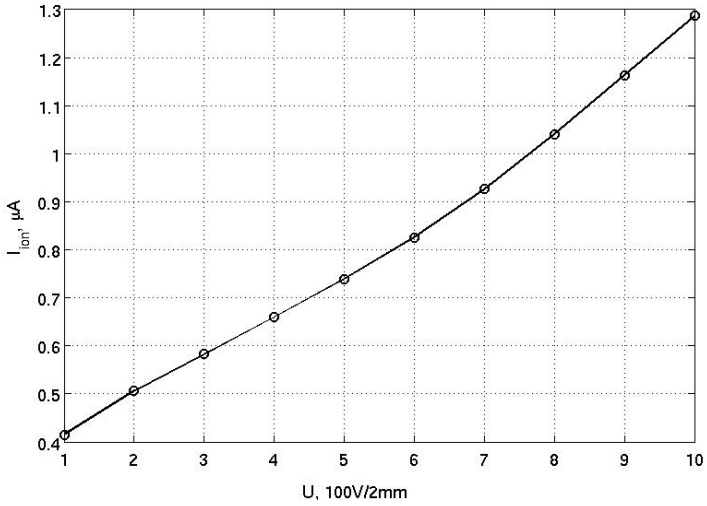

Figure 4.10: The ion current rises when the accelerating voltage increases, due to the Schottky effect.

4.5 Source design for 0.25” emitter

The emitter operates at a temperature of about 1100°C, thus all parts of the fast ion source

should sustain this temperature. For the source material we chose molybdenum and boron nitride for the dielectical parts. To solve the problem of grid support a design with the grids squeezed between two rings was chosen, Fig.4.11. Three stainless steel screws squeeze each pair of rings. Two rings fabricated from boron nitride isolate the grids between them.

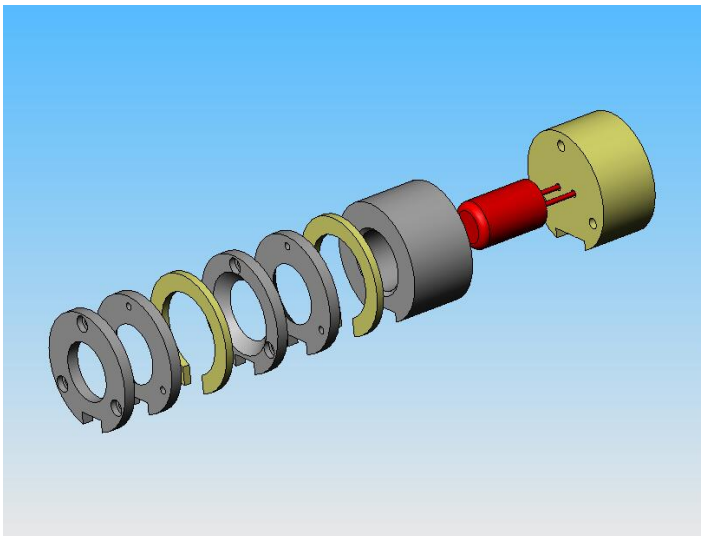

Figure 4.11: Main parts of the fast ion source (red is ion emitter, grey parts are made from molybdenum and yellow parts from boron nitride).

The grid and emitter supports are all placed inside a boron nitride casing, Fig.4.12, 24mm in diameter and 50mm in length. The source is glued to the ceramic tube with the glue "Resbond 989" [56], which can sustain temperature up to 1600˚C. A picture of the complete incased fast ion source is presented in Fig.4.13.

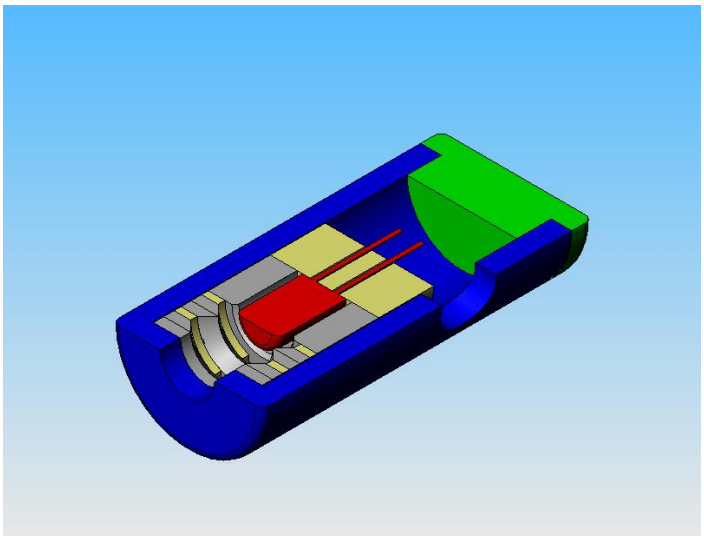

Figure 4.12: The schematics of the source.

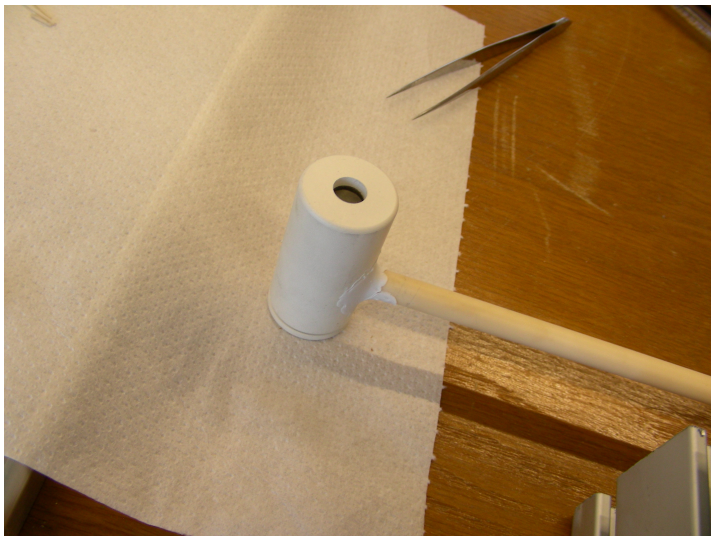

Figure 4.13: The incased fast ion source.

4.6 Source design for 0.6” emitter

To increase the ion current, a fast ion source with a 0.6” emitter was developed, Fig.4.14, and constructed Fig.4.15. The main design principles are the same as for a smaller source. Its dimensions are 43mm in diameter and 70mm length. The interest of this source is to extend operation to higher density plasmas, both in TORPEX and other devices. Naturally, increased dimensions imply a trade-off on the spatial resolution of the fast ion scan injection point.

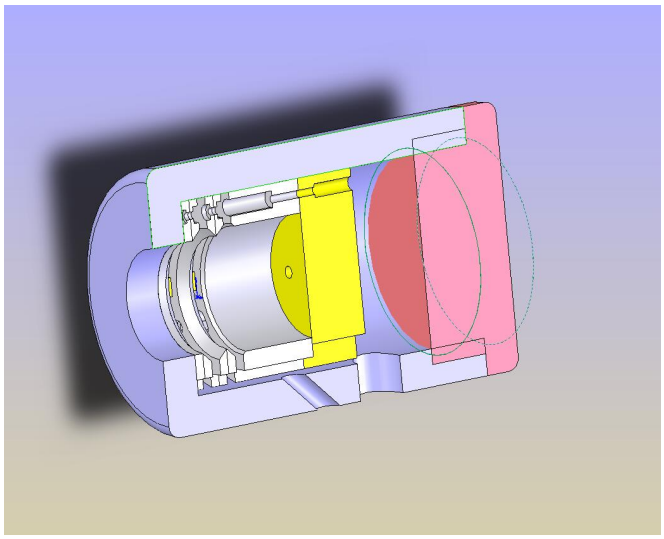

Figure 4.14: Schematics of the fast ion source with 0.6” emitter.

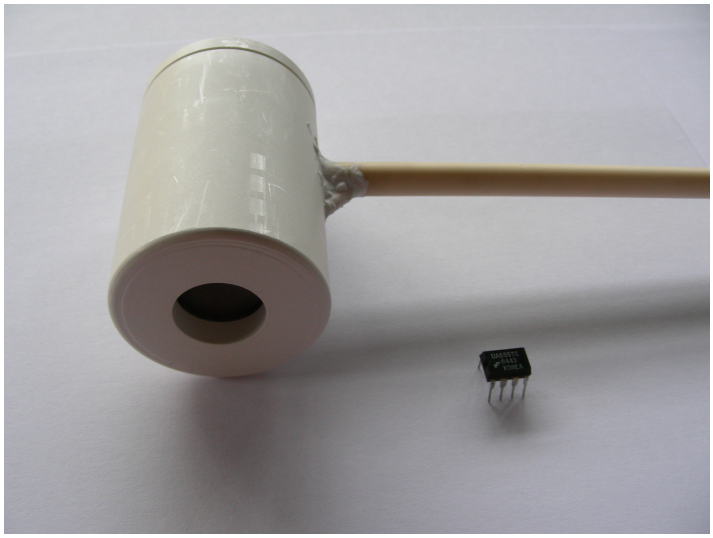

Figure 4.15: The incased fast ion source with 0.6" emitter.

4.7 2D probe positioning system

The fluctuation and turbulence level strongly depends on background plasma profiles e.g., on the position of the pressure gradient, and for different regimes the region of interest may vary in the poloidal cross section. Thus, it is necessary to install both the fast ion source and the gridded energy analyzer on a 2D poloidally moving system to be able to change the fast ion deposition radially and vertically and to measure the fast ion current profile over the whole plasma cross section. Considering the high price and the limited lifetime of conventional bellows, for both motions we have chosen to use sliding seal feedthroughs with differential pumping (Fig.4.16), a solution similar to that adopted on the large plasma device LAPD [57]. The design of the angular feedthrough based on a steel ball allows an angular excursion of up to 70°. Ceramic tubing supports the probe inside the plasma column. As a consequence, the linear feedthrough placed approximately 40 cm away from the ball see Fig.4.16. Such construction gives us the possibility to cover almost the entire poloidal cross section, except for a small upper-right part, a limitation caused by outside structures mounted on TORPEX. The positioning of the detector is achieved remotely using DC motors and controlled through software.

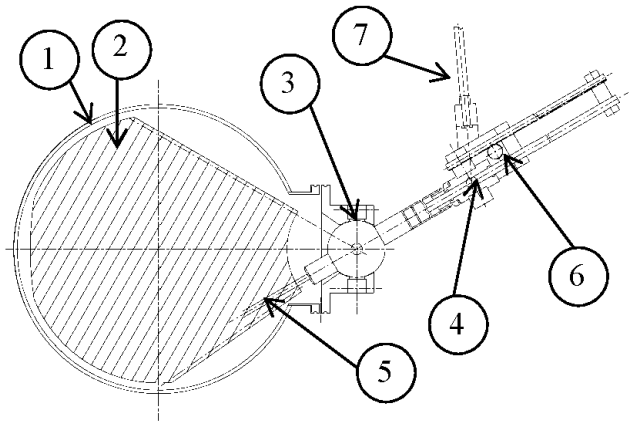

Figure 4.16: Drawing of 2D poloidally moving system. The main elements of the drawing are (1) vacuum vessel, (2) coverage area, (3) angular and (4) linear motion feedthroughs, (5) ceramic tube, (6) remote linear motion system, and (7) arm for remote angular motion.

These 2D moving systems are now widely used on TORPEX, including for triple probes, mach probes, mobile Rogowskii coils, gas-puffing systems, the fast ion detector and the fast ion source themselves.

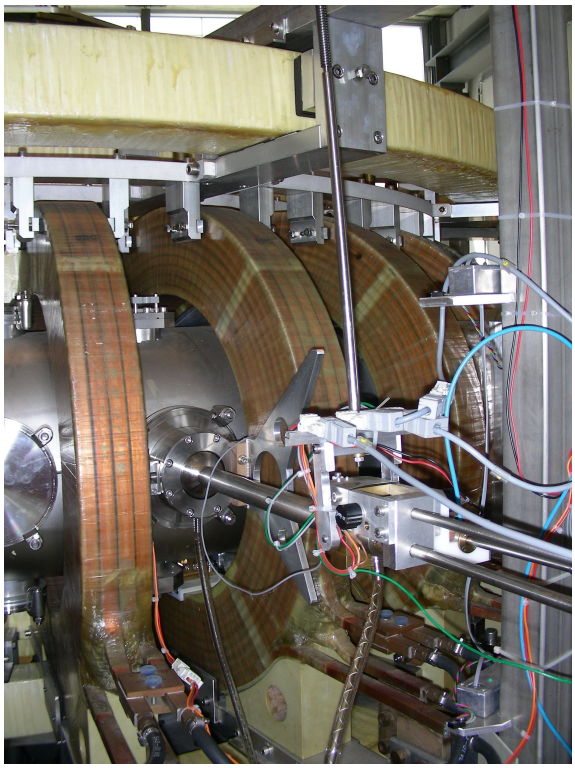

Figure 4.17: Photo of 2D poloidally moving system installed on TORPEX.

Chapter 5

Double gridded energy analyzer

A fast ion detector should have small physical dimensions, should be able to measure a fast ion current as small as 0.1μA; the casing of the detector should be vacuum and plasma compatible and the detector should be able to withstand microwaves. We chose to use a miniaturized gridded energy analyzer [58]. This detector can measure fast ion energy and current density profiles. To improve the signal to noise ratio, a design with two gridded energy analyzers was chosen. The advantage of this configuration is that one GEA measures the fast ion beam together with the background signal and the other GEA measures only the background noise. Thus the actual signal from fast ions can be obtained by a subtraction of signals from the two parts of the detector.

5.1 Design of the double gridded energy analyzer

Each gridded energy analyzer consists of two grids and a collector (Fig.5.1). The external grids are usually set at plasma potential to minimize the plasma perturbation. The size of the grid mesh was chosen to be smaller than the Debye radius to impede penetration of plasma into the detector. The aim of the internal grids is to prevent electrons from reaching the collector. That is why the potential on these grids is set negative and much higher than the electron temperature. Another feature of this detector is to have movable collectors. By moving the collectors one can choose the sensitivity angle of the detector: when the collector is close to the internal grid, the detector is sensitive to particles coming from a wide angular distribution.

Collectors should have positive potential, so that they capture all ions with energy higher than the set potential. Sweeping the collector potential allows one to measure particles with energy higher than the potential of the collector with respect to the plasma potential. Using this data one can obtain the energy distribution function.

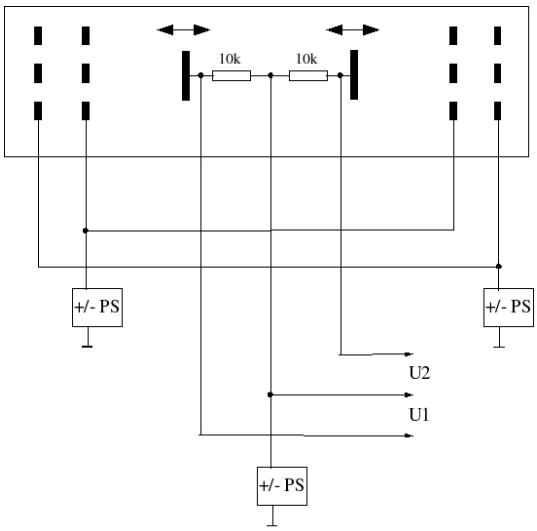

Figure 5.1: Schematics of the double gridded energy analyzer.

To measure the electron energy distribution the polarities of potentials on the internal grid and collector should be simply inverted.

An exploded view of the detector is shown in Fig.5.2. The dimensions of the detector are 15x70mm^2. The spatial resolution is determined by the inlet diameter of the analyzer, 6 mm, and by the accuracy of the 2D system positioning, about 5 mm. An energy resolution of ~1V is enough to measure the fast ion beam energy distribution, in order to investigate transport both in real and velocity space that could be caused by interactions with the plasma.

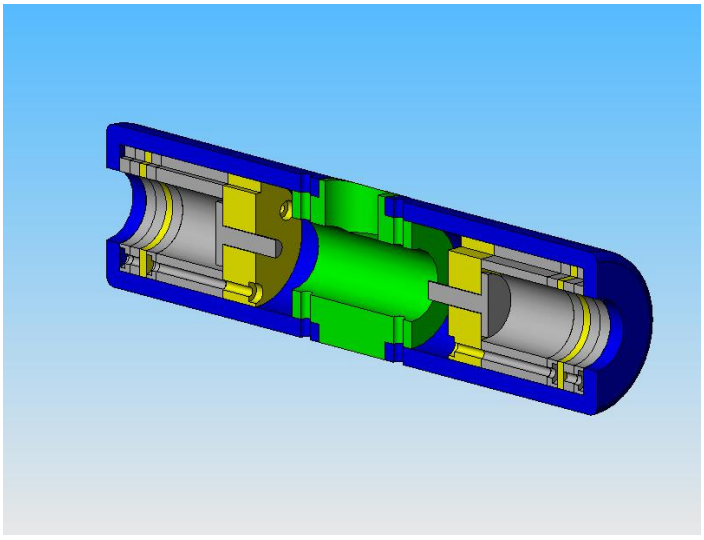

Figure 5.2: An exploded view of the fast ion detector (grey parts – rings with grids and collectors; yellow – insulators from plastic; blue and green – macor casing).

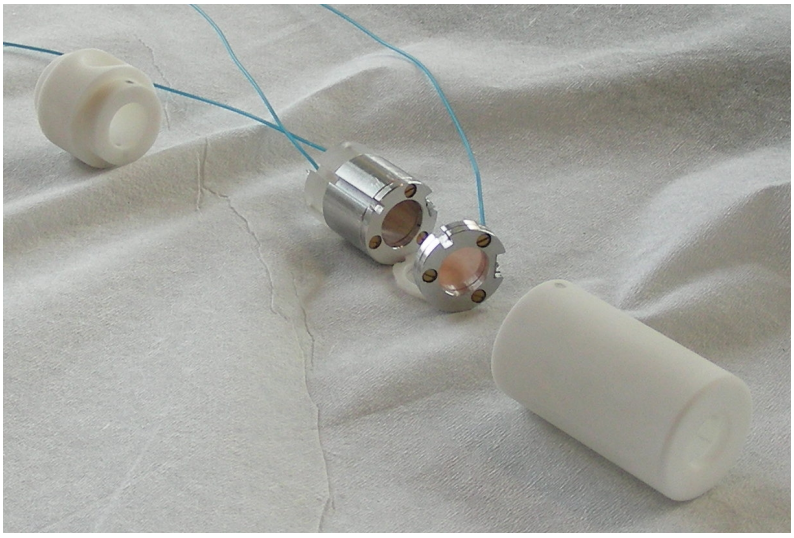

Figure 5.3: Assembeling one of the two identical parts of the detector. The macor casing and the grids squeezed between aluminum rings can be seen.

5.2 Electronics for double gridded energy analyzer

The electronics for the detector consists of three 100V power supplies (Fig.5.1). The signals from the collector can be measured in one of three ways: 1) from one side of the detector (U_1); 2) from the other side (U_2); 3) differentially (U_1-U_2). These regimes can be chosen

before each experiment. Two resistances of 10kOhm are installed inside the detector, whose purpose is to convert current into voltage. They are installed inside the detector to minimize the noise level. Isolated preamplifiers with a gain at 1, 10 or 100 are then used. After there is a main amplifier with a gain 2, 4, 10, 20, 40 or 100. The amplified signal is acquired with a sampling frequency of 250kHz. This electronics allows us to measure a fast ion current of the order of 0.1μA. It also allows sweeping the voltage with an arbitrary waveform at the grids and/or collectors with a frequency up to 3kHz. This frequency is limited by the parasitic capacitance of the detector.

5.3 Electron distribution function measurements

Measurements of the electron energy distribution function were performed to test the detector and the electronics. In these experiments we measure the electron distribution function from each part of the detector separately. The detector was aligned toroidally. Thus, one part of the detector was measuring the distribution function of electrons with a velocity collinear to the toroidal magnetic field, and another part was measuring the opposite directed electron distribution function. The voltage on the collectors was swept at a frequency of 330Hz. An example of the temporal evolution of the measured signal (U_1) and of the voltage (U_{col}) on the collector is shown in fig.5.4.

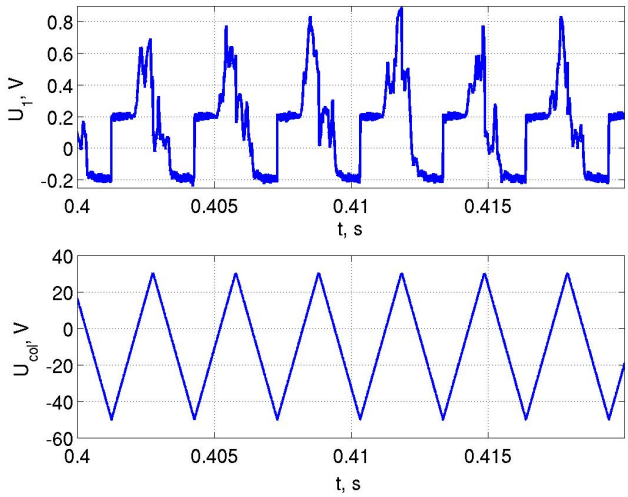

Figure 5.4: The example of temporal evolution of measured signal (U_1) and tension (U_{col}) on collector.

The step in each period on a measured signal can be explained by the internal capacity of the detector and of the wires between the detector and preamplifiers. To analyze this data an average over each period of the signal was performed. The averaged electron distribution function for each part of the detector was obtained. Electron energy distribution functions were measured at different radial detector positions in the Z=0 horizontal plane, as presented in Fig.5.5.

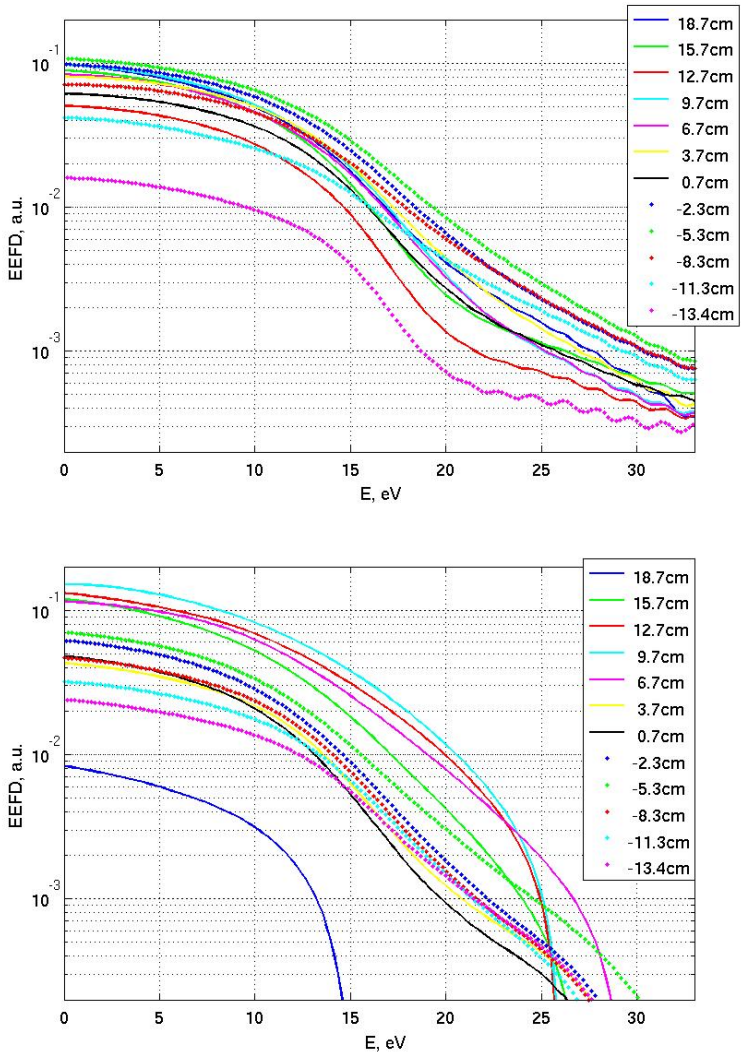

Figure 5.5: The electron energy distribution function as a function of radial detector position (in cm) on the Z=0 horizontal plane for the collinear to the toroidal magnetic field part (top) and opposite to the toroidal field part (bottom). The conditions of the discharges are: the Argon pressure is 1.1×10^{-5}mbar, the microwave power 10kW, and the reversed toroidal field is 76mT.

Using these data one can estimate the temperature of the fast and thermal electron populations. We assume that in the high electron energy range we do not have any contribution from the thermal part, hence the slope of the distribution function in this range provides the temperature of the fast electron population. Based on this temperature, we could find the temperature of the thermal electron population. The results of this analysis are shown in Fig.5.6.

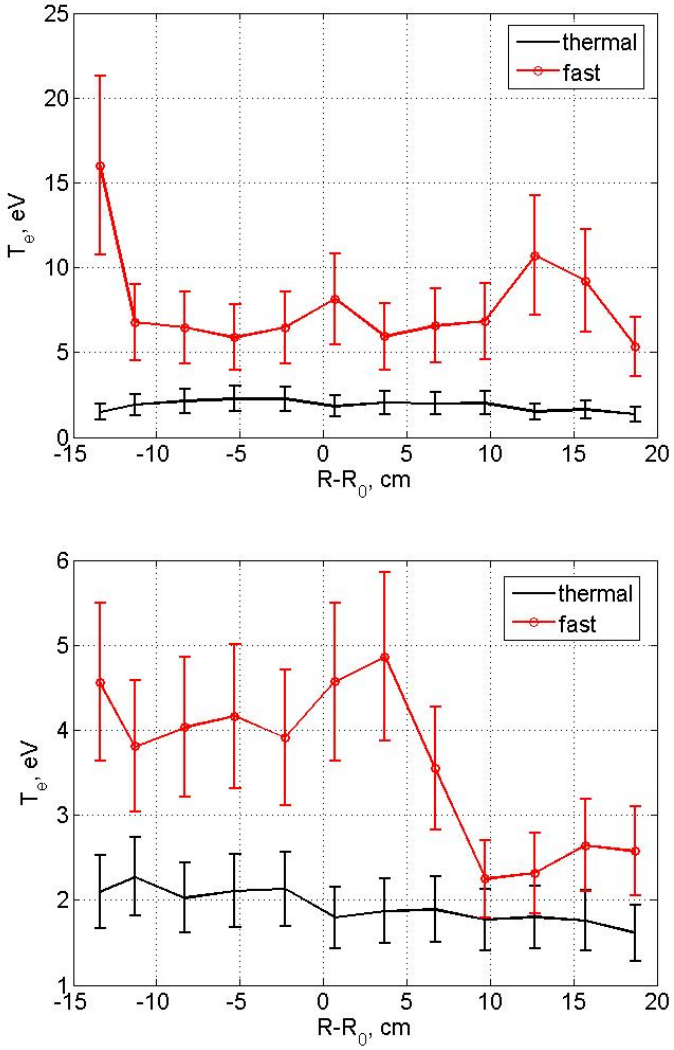

Figure 5.6: The temperature of fast (red) and thermal (black) electron population as function of radial position for collinear to the toroidal magnetic field part (top) and opposite to the toroidal field part (bottom).

The two peaks on the left of Fig.5.6 are situated at the same radial position as the electron cyclotron and lower hybrid resonances, where plasma production via electron acceleration and impact ionization takes place. The thermal population temperature is not significantly different from that of the fast electron population. This means that the most of the fast electrons have one preferred toroidal direction in TORPEX.

5.4 Analysis method used for ion current measurements

A synchronous detection [59] is necessary to extract the fast ion signal from noise. For this, the fast ion beam should be modulated. An example of the temporal evolution of the measured signal (U_1-U_2) and of the modulation voltage (U_{ref}) is shown in Fig.5.7.

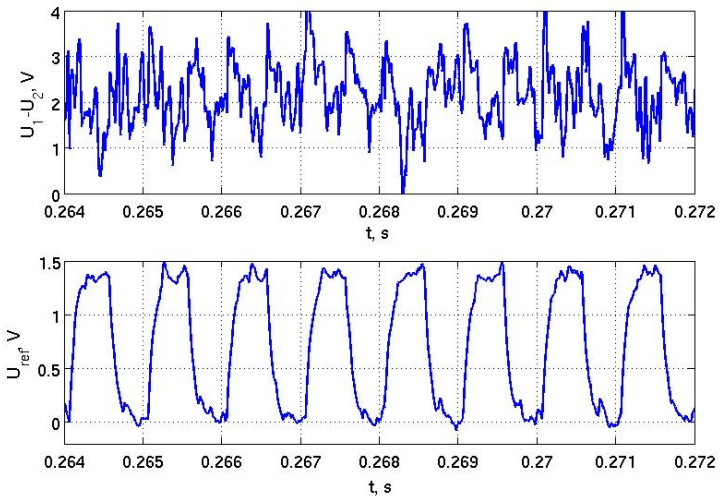

Figure 5.7: Example of temporal evolution of the measured signal (U_1-U_2) and the voltage (U_{col}) on collector.

For example, if the reference is sinusoidal and the actual signal is sinusoidal with a phase shift, θ, then the detection process consists of multiplying these two components together: $V_{out} = A\cos(\omega t)B\cos(\omega t + \theta) = \frac{1}{2}AB\cos\theta + \frac{1}{2}AB\cos(2\omega t + \theta)$. Thus, the output is: proportional to the magnitude of the input signal; proportional to cosine of the angle, θ, between it and the reference signal; and modulated at $2\omega t$. In a practical situation the signal is usually accompanied by noise, but it can be removed by the output filter.

Chapter 6

Specific set-up for the fast ion beam experiment

To investigate fast ion-turbulence interactions on TORPEX we should have a controllable fast ion source and diagnostics appropriate to measure the fast ion beam parameters, the background plasma profiles, and the turbulence properties. TORPEX plasmas are characterized by electrostatic fluctuations and turbulence originating from drift-interchange instabilities, driven by the pressure gradient and the magnetic curvature, i.e., mechanisms relevant to magnetic fusion [28]. The fast ion energy should be significantly higher than the plasma temperature, but low enough that fast ions are confined by the toroidal magnetic field. For TORPEX these conditions are satisfied for fast ion energies from 100eV to 1keV for Li-6 single ionized particles. The Li-6+ ion with 100eV energy has a Larmor radius of about 3.5cm for $B_T = 0.1T$.

6.1 Classical transport

The following formula for the slowing down rate of ion beam was derived [60]:

$$\frac{dE}{dt} = -\frac{2E}{\tau_s}\left(1 + \frac{E_{crit}}{E}\right)^{3/2}$$

where E is the energy of the fast ion, τ_s is the characteristic Spitzer slowing down time and E_{crit} is the critical energy. Below this energy the exchange from collisions with ions dominated over the exchange on the electron population. These two quantities are defined as:

$\tau_s = \frac{3\sqrt{2\pi}T_e^{3/2}}{\sqrt{m_e}m_i A_D}$, with

$A_D = \frac{ne^4 \ln\Lambda}{2\pi\varepsilon_0^2 m_i^2}$, and

$E_{crit} = \left(\frac{3}{4}\sqrt{\pi}\right)^{2/3}\left(\frac{m_i}{m_e}\right)^{1/3}\frac{m_i}{m_p}T_e$

where T_e is the electron temperature, m_e, m_i, m_p are the electron, fast ion and plasma ion masses, n is the plasma density, e is the electron charge, and $\ln\Lambda$ is the Coulomb logarithm.

A Li-6 fast ion with 100eV of energy makes one toroidal turn in 0.11ms. The slowing down time for typical TORPEX plasma parameters due only to classical collisions is 30ms. Thus the ion beam is expected to remain essentially monoenergetic during one toroidal turn. The critical energies for typical hydrogen and argon plasmas are equal to 440 and 180eV, respectively. Below these energies the collisions of the fast ions with thermal ions dominate over fast ion-electron collisions.

6.2 Space charge

After injection, the beam tends to diverge, due potentially to at least six mechanisms: particle drifts, space charge [61][62], classical transport, poloidal electric field, turbulent transport, and interaction with Alfvénic modes [6]. Experiments with and without plasma but with magnetic field will help us separate the first two from the last four mechanisms.

The divergence of the fast ion beam due to the space charge can be explained by the formula [63]:

$\frac{z}{r_0} = \sqrt[4]{\frac{e}{2m}}\frac{E^{3/4}}{I^{1/2}}\int_1^{r/r_0}\frac{dx}{\sqrt{\ln x}}$

where z is the distance covered by the fast ion beam, r_0, r are the initial and final radii of the fast ion beam cross section and I is the fast ion current. Assuming that $\left(\frac{r}{r_0}-1\right) << 1$, this

equation can be simplified:

$$\frac{z}{r_0} \approx \sqrt[4]{\frac{e}{2m}} \frac{E^{3/4}}{I^{1/2}} 2\sqrt{\frac{r}{r_0} - 1}$$

For typical TORPEX parametres for $z = 2\pi R_0$, where $R_0 = 1m$ is the major radius of the machine, this gives $\left(\frac{r}{r_0} - 1\right) \sim 3 \times 10^{-6}$ which is compatible with the assumption. Thus the divergence due to the space charge can be neglected. This statment is true as long as the ion current is below, or of the order of 1μA.

6.3 Fast ion trajectory

Both the source and the analyzer are installed on 2D poloidally moving systems in two different cross sections (Fig.6.1), to change the fast ion current deposition and to measure the fast ion current profile. The beam is launched toroidally.

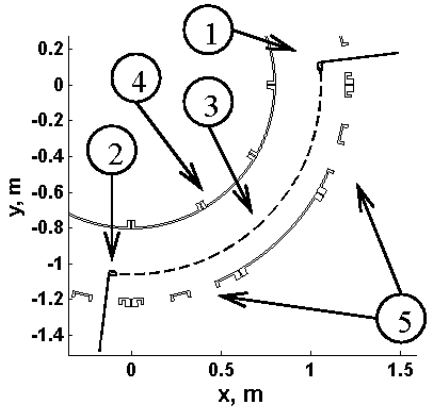

Figure 6.1: Toroidal cross section of TORPEX with (1) fast ion source with support, (2) gridded energy analyzer, (3) trajectory of fast ions, (4) vacuum vessel, and (5) ports.

The simulation of the single particle trajectory in a magnetic field configuration equivalent to that of TORPEX shows the possibility to control the beam trajectory and the particle drift divergence by varying the vertical magnetic field intensity. The vertical and horizontal displacements of the beam from initial poloidal position are shown in Fig.6.2 and 6.3. From this simulation one can conclude that the horizontal displacement is negligible with respect to the vertical one.

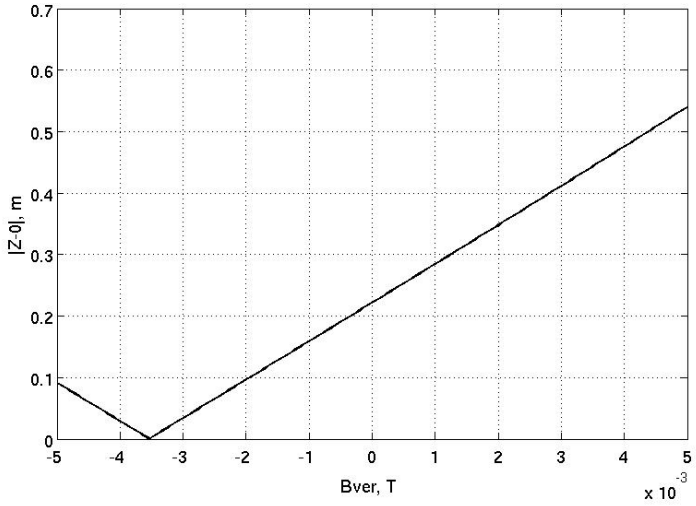

Figure 6.2: Vertical displacement of the fast ion beam from the initial poloidal position. The fast ion energy is equal to 100eV, the toroidal field is 0.1T.

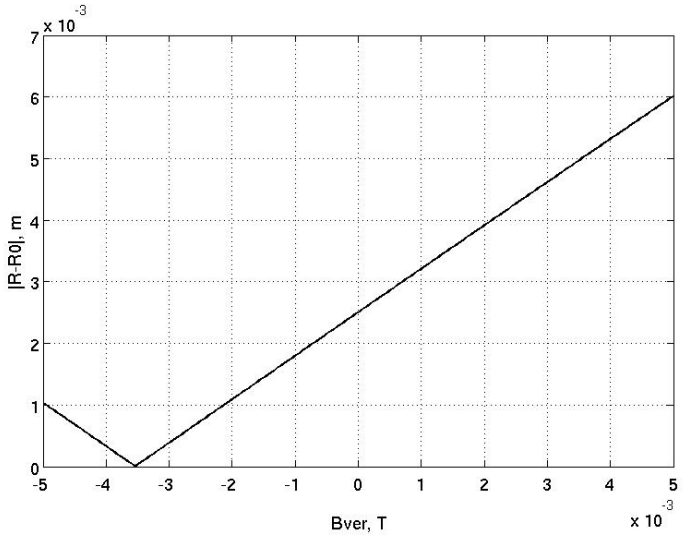

Figure 6.3: The horizontal displacement of the fast ion beam from the initial poloidal position. The fast ion energy is equal to 100eV, the toroidal field is 0.1T.

The simulations show that for a specific value of the vertical magnetic field the fast ion beam remains at the same poloidal position. To understand this effect one could consider the vertical and toroidal component of magnetic field separately. In this special case the velocity of fast ions remains all the time parallel to the toroidal field, which therefore does not influence the fast ion orbits. The circular motion of the ions corresponds to a gyration motion with a Lamor radius equal to the main radius of TORPEX. The value of this Lamor radius is defined by the vertical magnetic field.

Chapter 7

Simulation model of the fast ion interaction with turbulence

To interpret the experimental data two models were used. The first model is based on equations of motion and is written in MATLAB. It takes into account the magnetic field of TORPEX and the collisions with ions from the background plasma. In this model it was assumed that plasma influence on the beam only through collisions and static homogeneous on the scale of beam electric field. The second model does not take into account the collisions but considers the turbulent electric field. It is written in C++.

7.1 MATLAB based model

In this model we assume that the fast ion current is quite small. Thus the divergence of the beam due to space charge effects is negligible. We also assume that the interaction between fast ions is negligible, and neglect electron collisions. Hence one can use the equations of motion separately for each fast ion, taking into account the magnetic field of TORPEX, the electric DC field from the plasma and collisions with ions.

The equations of motion in the cylindrical coordinates with the z-axis coinciding with a symmetry axis of TORPEX are:

$$m\left(\frac{du_r}{dt}-\frac{u_\varphi^2}{r}\right)=q\left(u_\varphi B_z-u_z B_\varphi\right)$$

$$m\left(\frac{du_\varphi}{dt}+\frac{u_r u_\varphi}{r}\right)=q\left(-u_r B_z\right)$$

$$m\frac{du_z}{dt}=q\left(u_r B_\varphi\right)$$

where m and q are the mass and the charge of a fast ion, u_r, u_φ and u_z are components of the ion velocity, B_φ and B_z are the toroidal and a vertical components of the magnetic field (R_0 is the main radius of TORPEX, B_{tor} is the toroidal magnetic field on $R = R_0$):

$$B_z = const$$

$$B_\varphi = B_{tor}\frac{R_0}{r}$$

The Euler method [64] was used to solve these equations:

$$\frac{r_{i+1}-2r_i+r_{i-1}}{\Delta t}=\frac{q}{m}\left(u_{\varphi i}B_z-u_{zi}B_{tor}\frac{R_0}{r_i}\right)+\frac{u_{\varphi i}^2}{r_i}$$

$$\frac{u_{\varphi i+1}-u_{\varphi i}}{\Delta t}=\frac{q}{m}\left(-\frac{r_{i+1}-r_i}{\Delta t}B_z\right)-\frac{r_{i+1}-r_i}{\Delta t}\frac{u_{\varphi i}}{r_i}$$

$$\frac{u_{zi+1}-u_{zi}}{\Delta t}=\frac{q}{m}\left(\frac{r_{i+1}-r_i}{\Delta t}B_{tor}\frac{R_0}{r_i}\right)$$

where:

$$r_{i+1} = r_i + u_{ri}\Delta t$$

$$\varphi_{i+1} = \varphi_i + u_{\varphi i}\Delta t$$

$$z_{i+1} = z_i + u_{zi}\Delta t$$

with the initial conditions:

$$r_1 = r_0$$

$$\varphi_1 = 0$$

$$z_1 = 0$$

$$u_{r1} = 0$$

$$u_{\varphi 1} = v_0$$

$$u_{z1} = 0$$

where r_0 and v_0 are the initial radial position and velocity of the particles.

In reality the ion source has finite physical dimensions, thus the ion beam has finite initial dimensions. Thus r_1 and z_1 are homogenously distributed on the circular surface around a point on poloidal cross section $(r = r_0, z = 0)$. One should also take into account the angular distribution and the energy distribution of the emitted ions. This modifies the initial condition for the fast ion velocity:

$$u_{r1} = \left(v_0 + 2\sqrt{\frac{2T_b e}{m}} R_n(1) \right) \cdot \sin\left(\sigma \cdot a\cos\left(R(1)\right)\right) \sin(2\pi R'(1))$$

$$u_{\varphi 1} = \left(v_0 + 2\sqrt{\frac{2T_b e}{m}} R_n(1) \right) \cdot \cos\left(\sigma \cdot a\cos\left(R(1)\right)\right)$$

$$u_{z1} = \left(v_0 + 2\sqrt{\frac{2T_b e}{m}} R_n(1) \right) \cdot \sin\left(\sigma \cdot a\cos\left(R(1)\right)\right) \cos(2\pi R(1))$$

Here T_b is the fast ion temperature, $R_n(1)$ are normally distributed random numbers with mean 0 and variance 1, $R(1)$ and $R'(1)$ are homogeneously distributed random numbers in a range from -1 to 1, σ is a width of angular distribution. In these expressions the term in brackets takes into account the ion energy Gaussian distribution. The first multipliers in these equations take into account the energy distribution and the second multipliers account for angular distribution in such a way that $\left\|\vec{u}\right\| = v_0 + 2\sqrt{\frac{2T_b e}{m}} R_n(1)$ does not depend on the angle.

To take into account the collisions with the plasma particles the method proposed in [65] was used to modify particle velocity in each step:

$$u_{ri}^{new} = u_{ri}^{old} + u_{th}\sqrt{\frac{\nu\Delta t}{2}K} \cdot R(6)$$

$$u_{\varphi i}^{new} = u_{\varphi i}^{old} - \nu\Delta t u_{\varphi i}^{old} H + u_{th}\sqrt{\nu\Delta t H} \cdot R(6)$$

$$u_{zi}^{new} = u_{zi}^{old} + u_{th}\sqrt{\frac{\nu\Delta t}{2}K} \cdot R(6)$$

with

$$K = \frac{1}{x^3}\left(\left(x^2-1\right)\frac{2}{\sqrt{\pi}}\int_0^{x/\sqrt{2}} e^{-t^2}dt + \sqrt{\frac{2}{\pi}}xe^{-\frac{x^2}{2}}\right)$$

$$H = \frac{1}{x^3}\left(\frac{2}{\sqrt{\pi}}\int_0^{x/\sqrt{2}} e^{-t^2}dt - \sqrt{\frac{2}{\pi}}xe^{-\frac{x^2}{2}}\right)$$

$$\nu = \frac{ne^4\Lambda\left(m_i + m_p\right)}{4\pi\varepsilon_0^2 m_i^2 m_p u_{th}^3}$$

and $x = \frac{u_{\varphi i}^{old}}{u_{th}}$, where u_{th} is thermal velocity of the plasma ions, and $R(6)$ indicates homogeneously distributed random numbers in a range from -6 to 6

The simulated fast ion current profile with and without collisons and the velocity distribution function after one toroidal turn are shown in Fig.7.1, Fig.7.2 and Fig.7.3. The folowing conditions were used: a fast ion beam energy of 100eV with a standard deviation of 0.1eV, a toroidal field of 0.1T, a vertical field of -3.5mT, a plasma density of 10^{16}cm^{-3}, and a standard deviation of angular distribution of 0. These figures show that for the particles that travel one toroidal turn around TORPEX, the collisions with plasma ions become important and play an essential role in the beam divergence.

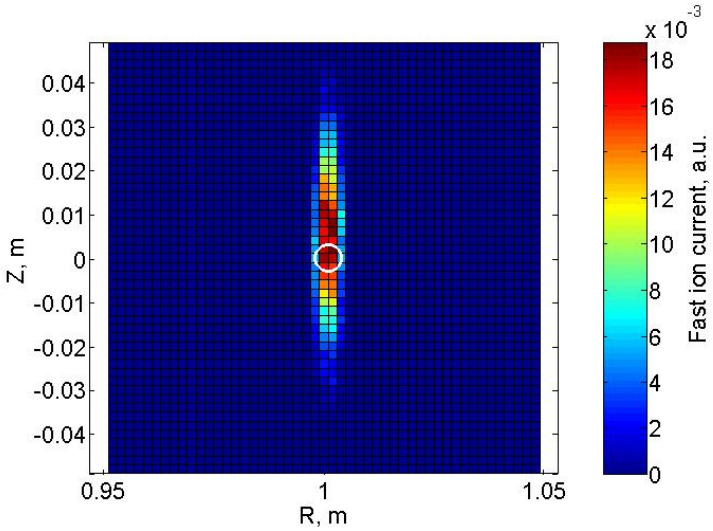

Figure 7.1: Histogram of the simulated fast ion current profile without taking into account Coulomb collisions (the white circle shows an initial beam position).

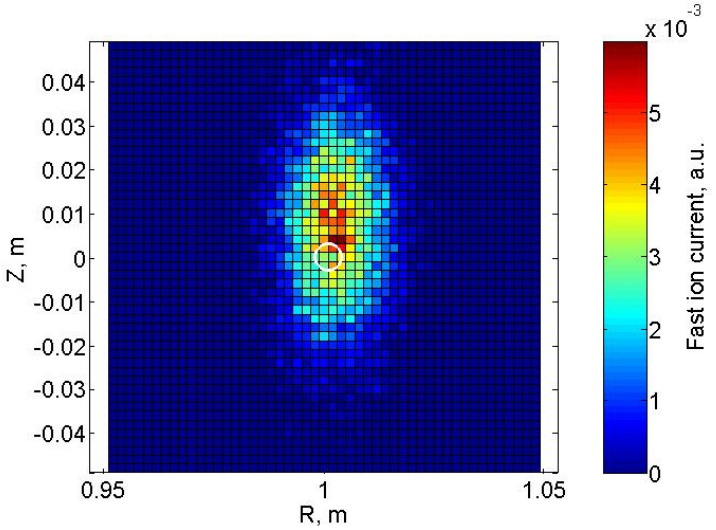

Figure 7.2: Histogram of the simulated fast ion current profile taking into account Coulomb collisions (the white circle shows an initial beam position).

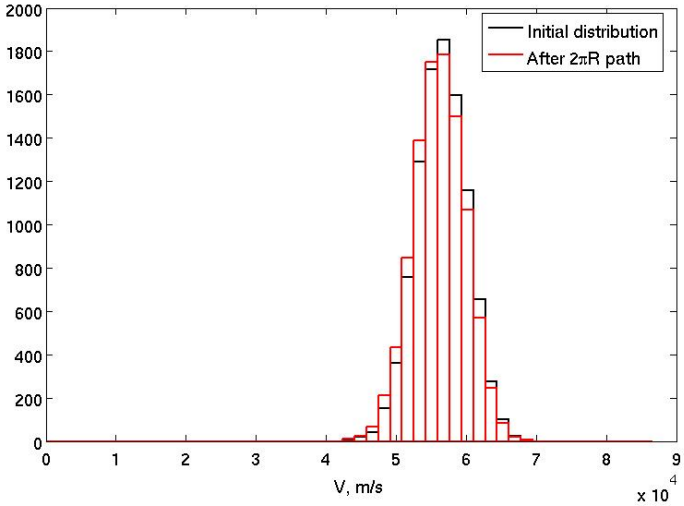

Figure 7.3: Histogram of the initial (black) and final (red) velocity distribution functions.

7.2 C++ based model

The equations of motion are used in this simulation with a turbulent electric field to describe the fast ion behavior in TORPEX plasma [66]. A Cartesian coordinate system is used:

$$\begin{cases} \dfrac{d}{dt}\vec{r} = \vec{v} \\ m\dfrac{d}{dt}\vec{v} = q\left(\vec{E}(\vec{r},t) + \vec{v}\times\vec{B}(\vec{r},t)\right) \end{cases}$$

To simplify these equations, a normalization scheme was used. The natural choice for the normalization of time is the ion cyclotron frequency, $\omega_B = \frac{qB_0}{m}$, where $m = 6 \cdot 1.67 \cdot 10^{-27} Kg$ is the mass of the Lithium ion. The velocity is normalized to the value $\upsilon_0 = \sqrt{\frac{2E_0}{m}}$ corresponding to fast ion energy of $E_0 = 1keV$. The $\vec{r}$ is normalized on the ion Larmor radius, $\rho_L = \frac{\upsilon_0}{\omega_B}$. The value of toroidal field is used for the normalization of the magnetic field. With these normalized units, the equations of motion had:

$$\begin{cases} \dfrac{d}{dt}\vec{r} = \vec{\upsilon} \\ \dfrac{d}{dt}\vec{\upsilon} = \vec{E}(\vec{r},t) + \vec{\upsilon} \times \vec{B}(\vec{r},t) \end{cases}$$

These equations in a discretized form:

$$\begin{cases} \dfrac{\vec{r}^{(n+1/2)} - \vec{r}^{(n-1/2)}}{\Delta t} = \vec{\upsilon}^n \\ \dfrac{\vec{\upsilon}^{(n+1)} - \vec{\upsilon}^n}{\Delta t} = \vec{E}\left(\vec{r}^{(n+1/2)}\right) + \dfrac{\vec{\upsilon}^{(n+1)} - \vec{\upsilon}^n}{\Delta t} \times \vec{B}\left(\vec{r}^{(n+1/2)}\right) \end{cases}$$

The Boris algorithm is used to solve them [67], which helps to separate the effect of electrical and magnetic fields without adding any numerical errors.

The magnetic field in the simulation has a vertical and a toroidal component:

$$\vec{B} = B_0 \frac{R_0}{R} \hat{e}_\varphi + B_z \hat{e}_z$$

Note that the ripple due to the finite number of toroidal coils is not taken into account. In [34], it is shown that in the region where the fast ion experiments were conducted the error in the magnetic field due to the ripple is less than 2%.

The main feature of the simulation is the presence of the electric field, both from the background and from turbulence, which is calculated by deriving the potential:

$$\vec{E}(\vec{x},t) = -\vec{\nabla}\phi(\vec{x},t) = -\begin{pmatrix} \frac{\partial}{\partial r}\phi(\vec{x},t) \\ \frac{1}{r}\frac{\partial}{\partial \varphi}\phi(\vec{x},t) \\ \frac{\partial}{\partial z}\phi(\vec{x},t) \end{pmatrix} = \begin{pmatrix} -\frac{\partial}{\partial r}\phi(\vec{x},t) \\ 0 \\ -\frac{\partial}{\partial z}\phi(\vec{x},t) \end{pmatrix}$$

The potential obtained by the 2D simulation [68] based on drift-reduced Braginskii equations [69] in CGS units:

$$\begin{cases} \frac{\partial n}{\partial t} = \left[\frac{c\phi}{B_0}, n\right] + \frac{2c}{eRB_0}\left(n\frac{\partial T_e}{\partial y} + T_e\frac{\partial n}{\partial y} - en\frac{\partial \phi}{\partial y}\right) + D\nabla^2 n - \frac{\sigma n c_S}{R}\exp\left(\Lambda - \frac{e\phi}{T_d}\right) + S_n \\ \frac{\partial \nabla^2\phi}{\partial t} = \left[\frac{c\phi}{B_0}, \nabla^2\phi\right] + \frac{2B_0}{cm_i R}\left(\frac{T_e}{n}\frac{\partial n}{\partial y} + \frac{\partial T_e}{\partial y}\right) + \nu\nabla^4\phi + \frac{\sigma c_S m_i \omega_{Bi}^2}{eR}\left[1 - \exp\left(\Lambda - \frac{e\phi}{T_d}\right)\right] \\ \frac{\partial T_e}{\partial t} = \left[\frac{c\phi}{B_0}, \nabla^2 T_e\right] + \frac{4c}{3eRB_0}\left(\frac{7}{2}T_e\frac{\partial T_e}{\partial y} + \frac{T_e^2}{n}\frac{\partial n}{\partial y} - eT_e\frac{\partial \phi}{\partial y}\right) + k_e\nabla^2 T_e - \frac{2}{3}\frac{\sigma T_e c_S}{R}\left[1.71\exp\left(\Lambda - \frac{e\phi}{T_d}\right) - 0.71\right] + S_T \end{cases}$$

where n, ϕ and T_e are density, electric potential and electron temperature of the plasma, D is the diffusion coefficient, ν the kinetic viscosity, k_e the thermal conductivity, $\sigma = \frac{RB_y}{B_0}$, $c_S = \sqrt{\frac{T_e}{m_i}}$, $\Lambda = \log\sqrt{\frac{m_i}{2\pi m_e}}$, S_n and S_T are particle and heat source, $[a,b] = \partial_x a\partial_y b - \partial_y a\partial_x b$, x and y are radial and vertical coordinates.

This simulation provides a 2D profile of the electric potential on a grid of 256×64 in the plane perpendicular to the total magnetic field. All profiles in this code are assumed to have symmetry along the total magnetic field. The potential is periodic in the poloidal cross section with a period equal to the distance between the return of one magnetic field line. The simulation time resolution, chosen to be 2.7μs, is enough for turbulence investigation but insufficient for simulating the fast ion dynamics. A linear interpolation was used to solve this problem.

The initial conditions of the simulation were similar to those used in the MATLAB simulation, with a difference that for the angular distribution a Gaussian distribution was chosen instead of a cosine distribution. The travel time of the fast ions (~2.5μs for the present experiments) is usually much less than the characteristic time of the turbulence (<10ms). Thus one should average the effect of turbulence on fast ions in order to eliminate

the effect of individual fluctuations. To do that, all fast ions are divided into bunches of 100 particles. Each bunch is launched with a time shift of 135μs. At the end of the run, we analyze all particles from all bunches.

In Fig.7.4, an example simulation is presented. Here the beam energy equals 300eV, the standard deviation of the energy is 0.3eV, the standard deviation of the angular distribution is 0.2rad, the electric field equals 0. First, the beam drifts in the vertical direction due to the toroidal drift (diamagnetic and curvature drift). Second the beam has ripples, due to the cyclotron motion.

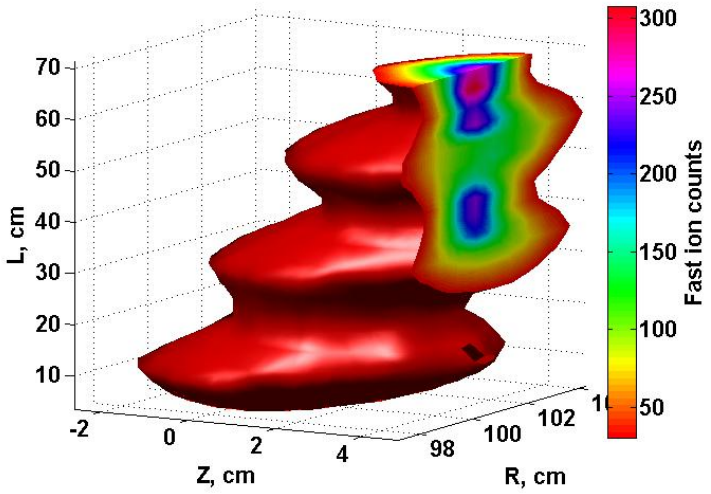

Figure 7.4: Isosurface of a fast ion beam (L is a coordinate along the toroidal direction)

Thus the C++ simulation provides full information about the fast ions (coordinates and velocity of each particle). However the simulation is not self-consistent because the fields produced by the fast ions themselves are not taken into account, nor are the collisions with plasma ions and neutrals.

7.3 Benchmarking the simulations.

In order to validate both simulations we launched them with similar initial conditions: the initial beam energy equals 300eV, the spread in energy equals 0.3eV, the spread in angle equals 0.2rad, the electric field equals 0 and no collisions. Here we compare the profiles moving away toroidally at L=26cm from the ion source position.

The fast ion current density profile simulated with the simple Matlab model is presented in Fig.7.5. The centre of mass is at R=1.01m, Z=1.8cm and the full width half maximum equals 3.6cm. The same profile simulated with the C++ model is shown in Fig.7.6. It has a similar centre of mass position of R=1.009cm, Z=1.8cm and identical full width half maximum of 3.7cm. The form of both profiles differs because of different functional angular distributions used in both models. The vertical displacement of 1.8cm could be also verified by drift theory [70]:

$Z_d = \frac{L}{\upsilon_{ion}}\upsilon_d = L\sqrt{\frac{m}{2E}}\frac{m}{eBR}\upsilon_{ion}^2 = 2.1cm$, where $L = 26cm$ is the toroidal displacement, υ_{ion} and υ_d are ion velocity and drift velocity.

Thus, both simulations with similar initial conditions have similar results, which are compatible with drift theory.

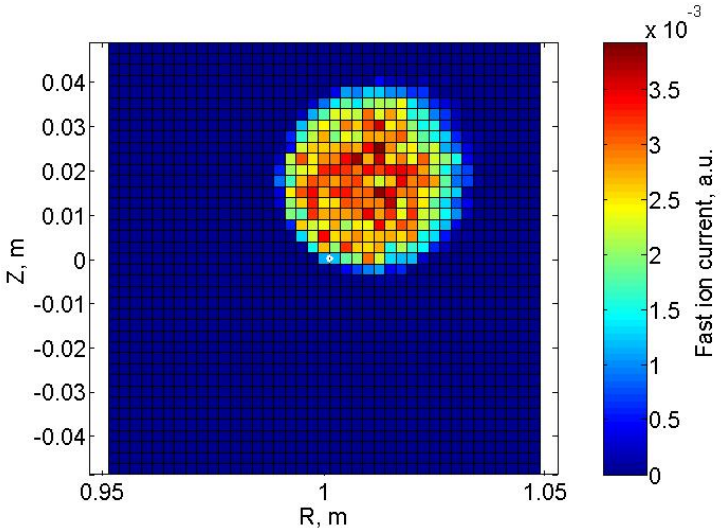

Figure 7.5: The fast ion current density distribution simulated using a simple MATLAB model at L=26cm.

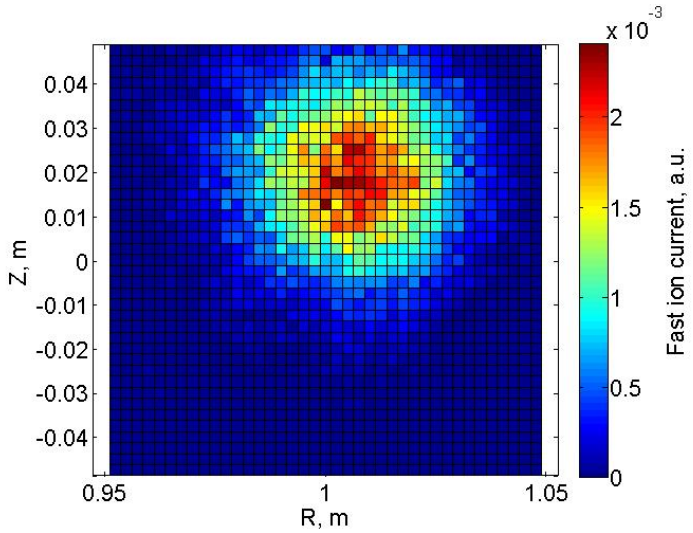

Figure 7.6: The fast ion current density distribution simulated using the C++ model at L=26cm.

Chapter 8

Experimental measurements

First of all, the experiments without plasma but with different magnetic configurations were conducted to establish the fast ion beam behavior. Then, in order to investigate the interaction of turbulence on the fast ion beam we compared fast ion profiles in the presence and absence of turbulent well characterized plasma.

8.1 Basic plasma scenario

Most of the experiments presented here were conducted using hydrogen plasmas produced by means of magnetron-generated microwaves in the electron cyclotron range of frequencies with a maximum power of 400W. The magnetron (2.45GHz) is set to deliver the maximum power during the first second, then during the next 0.6 seconds it delivers a residual power of approximately 200W (Fig.8.1). As a consequence, during each shot we have three stages, one with the maximum power value, another one with only the residual value and the third one without any power, i.e. no plasma but with all magnetic fields and neutral gas.

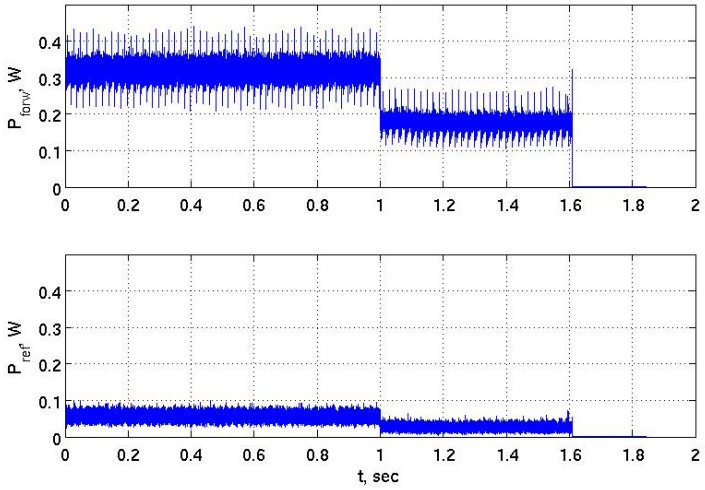

Figure 8.1: The evolution of the forward and reflected electron cyclotron power during the chosen TORPEX discharges.

The magnetic field has a dominant toroidal component of 76mT, on which a small vertical component of 2.3mT is added, resulting in helical magnetic field lines. The background gas pressure is fixed at 4×10^{-5}mbar. The temperature, density and plasma potential profiles in such a plasma are presented in Fig.8.2, 8.3 and 8.4.

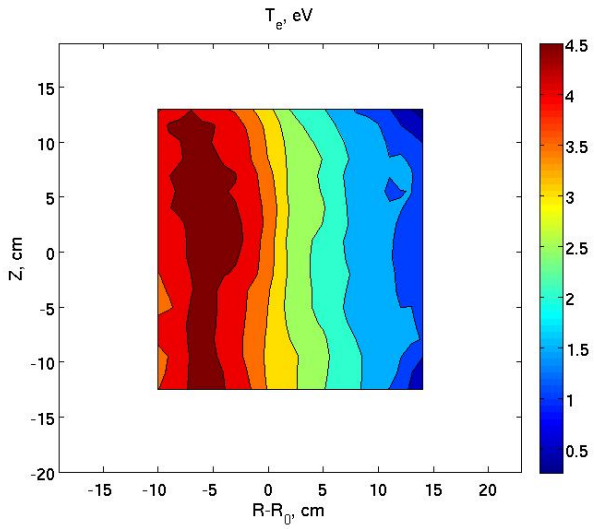

Figure 8.2: The temperature profile measured with an SLP Langmuir probe.

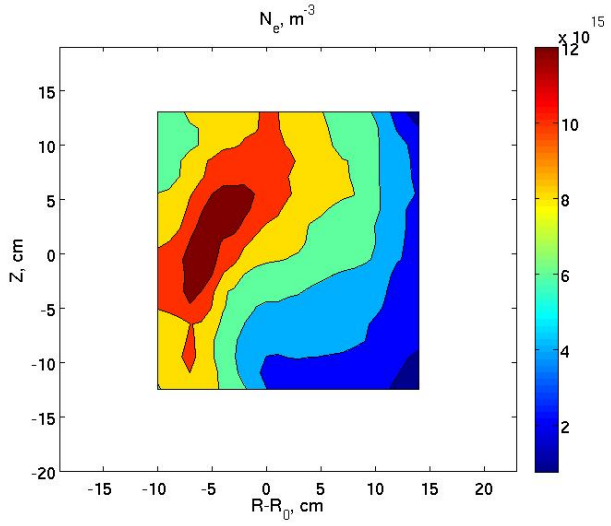

Figure 8.3: The density profile measured with an SLP Langmuir probe.

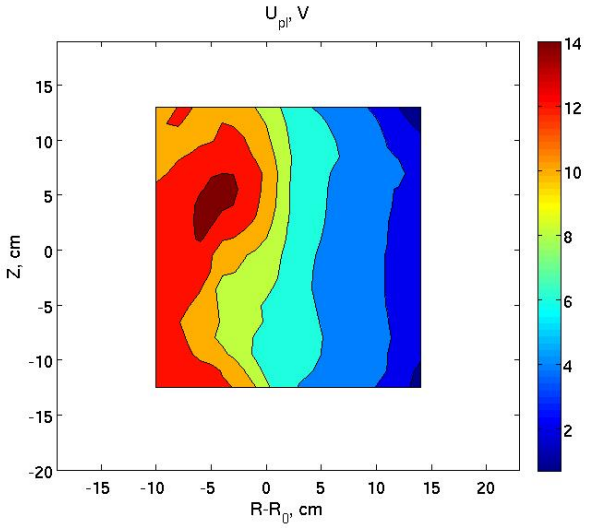

Figure 8.4: The plasma potential profile measured with an SLP Langmuir probe.

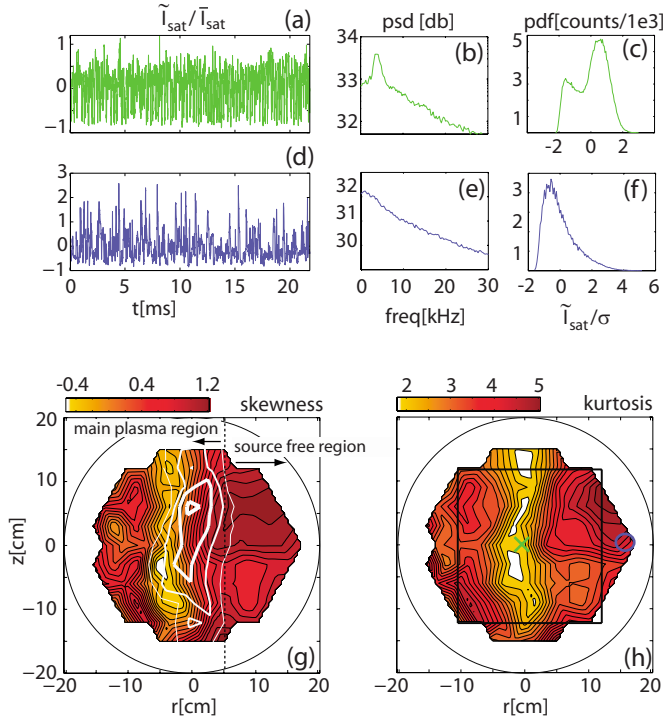

Figure 8.5: Figure extracted from [71]. Time series of ion saturation signals (a), (d) at the two locations indicated in (h) show coherent fluctuations in the main plasma region (mode region) (cross) and intermittent bursts at the edge (circle). Also shown are the respective probability distribution functions in frames (c), (f) and the power spectral densities in frames (b), (e). (g), (h) 2D poloidal profiles of skewness and kurtosis of ion saturation signals. In (g) the profile of the fluctuation power in the frequency range 3.9±0.5kHz is shown in white and localizes the interchange wave.

Two main poloidal regions characterize this plasma [71]. The first region, $-5cm \le (R - R_0) \le 5cm$, is referred to as the mode region, as it is dominated by a coherent interchange wave. The second region, $5cm < (R - R_0) \le 15cm$, is characterized by the propagation of blobs, i.e. structures generated by turbulence corresponding to the region of enhanced plasma pressure, hence it is called the blob region. The properties of the density fluctuations obtained with HEXTIP are shown in Fig.8.5.

8.2 Fast ion source and detector set-up

The fast ion beam is launched at the equatorial plane along the toroidal direction. The detector is installed in the nearest vacuum port, resulting in a toroidal distance between the detector and the source of 12.86˚ (Fig.8.6). This corresponds to a fast ion path of 22.4cm, when the source and the detector are at the center of the vacuum chamber.

An important parametric dependence to understand of the interaction between fast ions and turbulence is that of the fast ion transport as a function of the fast ion energy. To perform these studies and compare the results quantitatively, one should make sure that the angular and energy distribution of the fast ion beam remains unchanged. It is therefore not sufficient to increase the emitter potential to increase the fast ion energy, because this will change the focal length of the accelerating system.

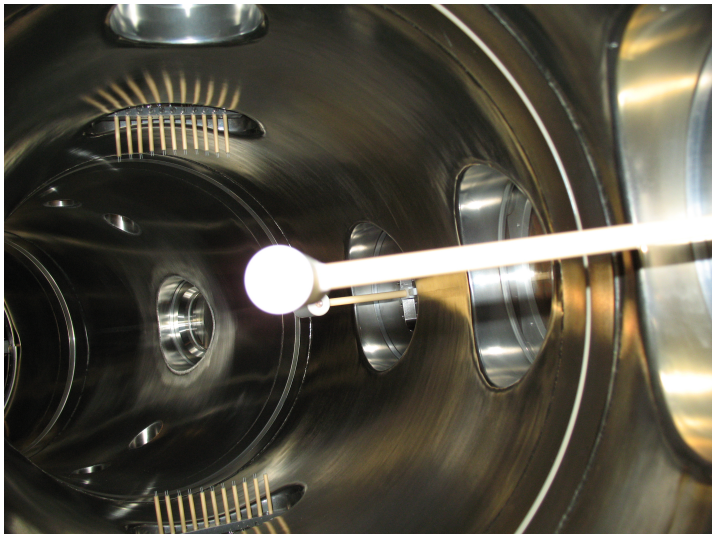

Figure 8.6: Fast ion source and double gridded energy analyzer installed on TORPEX.

To solve this problem let us consider the case when the fast ion source is aligned with the magnetic field so that one can neglect the magnetic field influence. Using the axial symmetry of the source, the electric field in cylindrical coordinates inside the source can easily be calculated [72]:

$$E_r = -\frac{\partial U(z)}{\partial r} \approx -\frac{r}{2}\frac{d^2U(z)}{dz^2}$$

$$E_\varphi = 0$$

$$E_z = -\frac{\partial U(z)}{\partial z} \approx \frac{dU(z)}{dz}$$

Here the z-axis coincides with the symmetry axis of the source and $U(z)$ is the electric potential. Using these assumptions the equation of motion is:

$$\sqrt{U(z)}\frac{d}{dz}\left(\sqrt{U(z)}\frac{dr}{dz}\right) = -\frac{r}{4}\frac{d^2U(z)}{dz^2}$$

This equation is linear with respect to the potential. As Maxwell's equations are also linear, by increasing the potential of all grids and the metallic parts inside the source simultaneously by the same fraction the trajectory of the ions should remain the same. Table8.1 presents the values of the potential applied on the external, internal grids and on the emitter as a function of the fast ion energy.

Table 8.1. Potentials on the grids and the emitter.

Fast ion energy, eV	External grid, V	Internal grid, V	Emitter potential, V
300	0	-100	300
600	0	-200	600
900	0	-300	900

In the detector the potential was set to 0V on the external grids, -50V on the internal grids and +50V on the collectors. These values remain unchanged during all discharges. The detector is thus sensitive to all ions with energies above approximately 50eV.

The double gridded energy analyzer measures the 2D ion current density profile. To quantify the profile shape we used several quantities. First, we evaluate the radial and vertical positions of the profile maximum. Second, we measure the full width at half maximum (FWHM) along both the R and Z directions. A third type of values is needed to quantify the asymmetry of the profile along both directions. To illustrate these quantities we plot the R cut of the arbitrarily chosen profile in Fig.8.7. The FWHM along the R direction is equal of $R_B - R_A = 1.13cm$. Point D is a maximum, and point C divides AB by two equal parts (AC=CB). The value $\delta = R_D - R_C = R_E - R_C = -0.09cm$ characterizes the asymmetry of

the profile along the R direction. A negative value means that the maximum is shifted to the left, i.e. to the high field side. These values do not completely quantify the profile, but they help quantifying the comparison between theory and experiment.

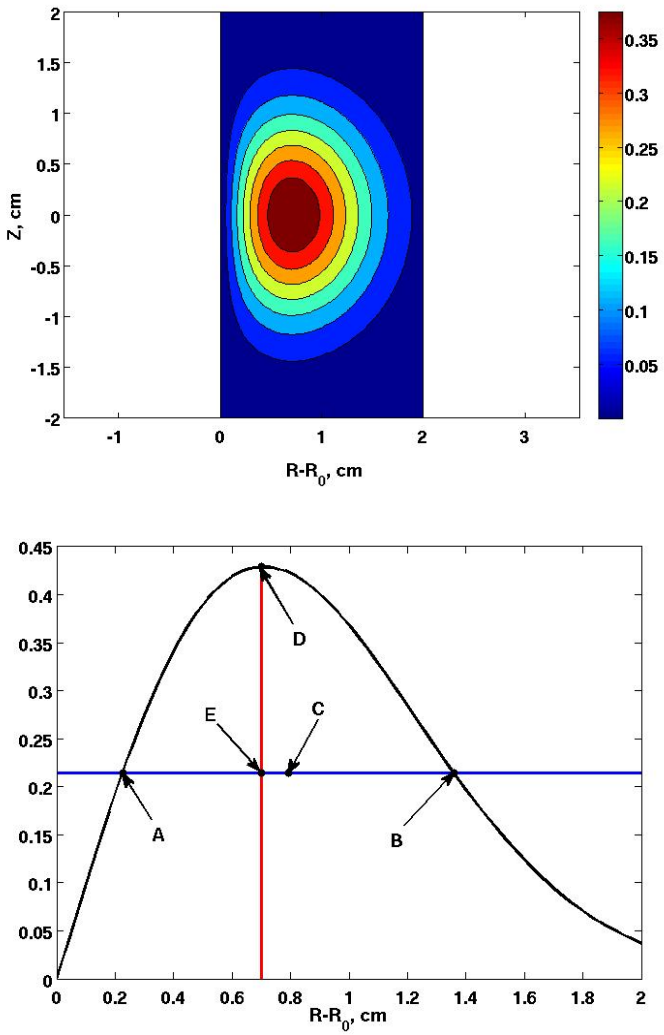

Figure 8.7: An illustration of the FWHM and δ (asymmetry measure) calculation.

8.3 Experiments without plasma

To establish the behavior of the fast ion source and double gridded energy analyzer and to understand the fast ion beam behavior in the presence of magnetic fields and plasma a first set of experiments was conducted without any magnetic fields and without the plasma. In these experiments the vacuum chamber was filled with hydrogen at pressure 1.9×10^{-5}mbar. The modulation frequency of the source was equal to 125Hz. The source was placed in the poloidal position $R-R_0=0cm$, $Z=0cm$, the fast ion energy was 300eV and the ion current

on the external grid amounted to 0.85μA. First we put the double gridded energy analyzer in a poloidal plane 25.7º away toridally from the source. At such large distance the signal on the analyzer was comparable with the noise level. The main source of the noise in the absence of plasma is coupling with the modulated voltage on the source. In the presence of plasma, in spite of the fact that the grids of the detector have smaller cells than the Debye length, some electrons of the background plasma, from the Maxwellian tail and from fast electrons accelerated by microwaves (Fig.5.6), can penetrate into the detector and perturb the signal. To increase the signal we placed the analyzer and the source in the two nearest ports that have a toroidal separation of 12.9º. This separation corresponds to 22.4cm of toroidal distance for the case when the detector and the source are both at $R - R_0 = 0cm$.

The double gridded energy analyzer was moved discharge by discharge to cover most of the poloidal plane. 75 discharges were conducted to make the fast ion current density profile presented in Fig.8.8. The width of the measured profile is much larger than the outlet diameter of the source (0.6cm). The beam current density profile has a maximum at $R - R_0 = 3cm$, $Z = 0.5cm$. As we will see further this displacement can be simply explained by the fact that fast ion beam propagates in straight lines. The profile has almost circular shape. The FWHM in the radial direction of 2.7cm is similar to that in the vertical direction, which is of 2.6cm. The asymmetry measure along the radial (0.1±0.1cm) and vertical directions (0.0±0.1cm) is negligible.

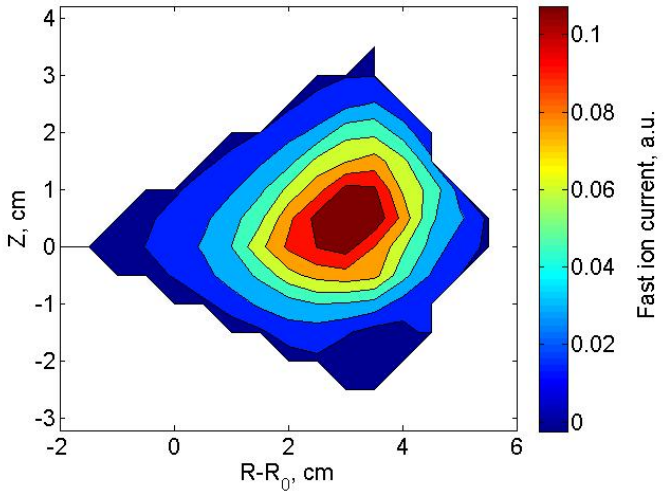

Figure 8.8: The fast ion current density profile (arbitrary units) for the case without plasma and without magnetic fields.

The beam current density profile in the presence of an inverted toroidal magnetic field, with respect to the usual configuration, of 79mT is shown in Fig.8.9. The other parameters of the experiment remained unchanged. The maximum of the profile shifts vertically downward (in the direction of the toroidal drift for ions), resulting in a maximum at $R - R_0 = 3cm$, $Z = -1cm$. One can also notice that the width of the profile decreases, with a radial FWHM equal to 2.3cm and a vertical one of 2.3cm. The asymmetry of the profile increases, but remains small, -0.3 cm in radial and -0.4cm in vertical direction.

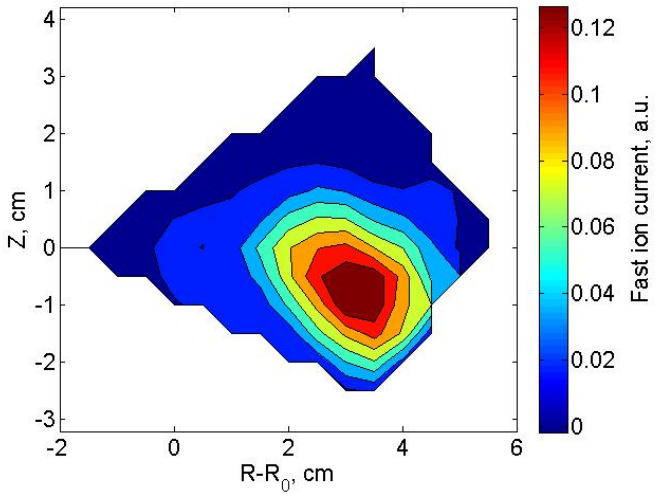

Figure 8.9: The fast ion current density profile for the case without plasma and with only the toroidal magnetic field.

We then added to this configuration a vertical magnetic field of 0.8mT, oriented downwards. 57 shots were used to construct the fast ion current density profile presented in Fig.8.10. The position of the maximum remains the same as without vertical field. Nevertheless, the FWHM in the radial and vertical directions differ and are equal to 2.0cm and 3.3cm, respectively. The asymmetry measures in the radial and vertical directions are 0.2cm and -0.8cm, respectively.

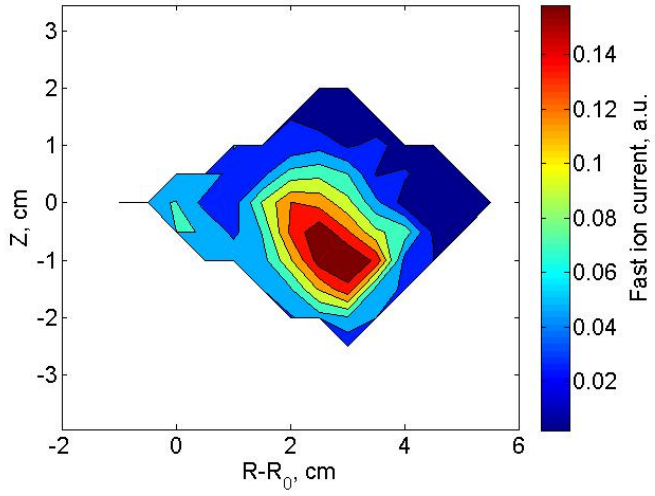

Figure 8.10: The fast ion current density profile for the case without plasma, with toroidal and vertical magnetic fields.

The next natural step was to see how this profile is modified in the presence of plasma (Fig.8.11). A microwave power of 400W was used to ionize the hydrogen. The profile shifts upward by 0.75cm and inward by 0.5cm, and the maximum of the profile is at $R - R_0 = 2.5cm$, $Z = -0.3cm$. The profile becomes more circular, the FWHM in radial and vertical directions are 2.4cm and 2.3cm respectively. The asymmetry measures in the radial and vertical directions are negligible and equal to 0.0cm and 0.1cm, in that order.

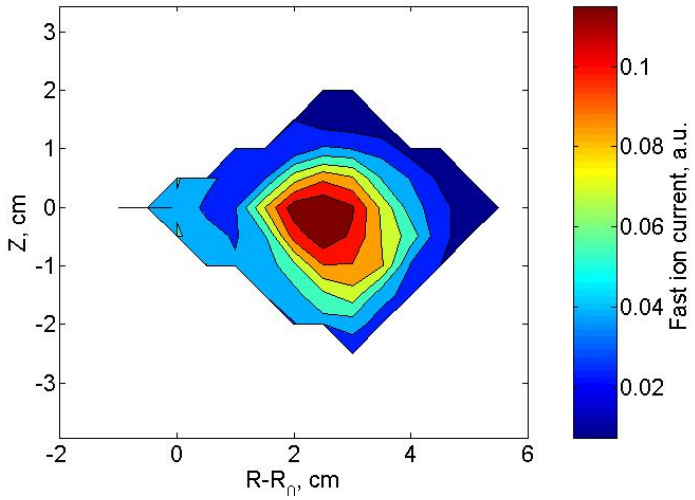

Figure 8.11: The fast ion current density profile for the case with plasma and with all magnetic fields.

These first calibration experiments show that reliable measurements of the fast ion current profile can be obtained using the fast ion source and double gridded energy analyzer when the distance between them is of the order of 25cm. The experiments also show that the plasma interacts with and modifies the fast ion beam even over this short distance. The integral in a.u. of the presented profiles is equal to 0.98, 0.93, 1.04 and 0.88 for Fig.8.8, 8.9, 8.10 and 8.11. Thus within 13% of accuracy, there is conservation of the particles between these profiles. It is very unlikely that the density and velocity of the fast ions both vary to give the same current because for this to happen, the fast ion velocity or density should increase, which is difficult to imagine. That means that the plasma does not significantly slowdown the fast ions and that no significant volume losses occur between the source and detector.

8.4 Experiments with plasma in the blob region

A series of experiments was conducted in a blob-dominated region. The following configuration was used: an inverted toroidal magnetic field of 79mT, a downward vertical field of 0.8mT, a background pressure of 3.5×10^{-5}mbar, an ion current on the external grid of the source of 3.01μA and a microwave power of 400W in the first second of the discharge then 200W during the next 0.6s. To measure each profile, 51 shots were run. With three different levels of microwave power (Fig.8.1), during each shot we measured the fast ion current in a case without plasma (microwave power of 0W), in the case we refer to as the main plasma (microwave power of 400W), and in the case we refer to as the residual plasma (microwave power of 200W). The profiles for these three cases could be constructed. The modulation frequency of the source was equal to 1kHz.

The fast ion current density profile in the case without plasma is presented in Fig.8.12. The source was not perfectly aligned with the toroidal direction, as a consequence only part of the profile was measured. The maximum of the profile is situated at $R-R_0=13cm$, $Z=-4cm$, and its position is similar to the case with the residual value of power (Fig.8.13). In the case with the plasma, the position of the maximum shifts slightly upwards by 0.5cm (Fig.8.14) with respect to the case without plasma. If we assume symmetry of the profile

along the vertical direction, we can calculate the FWHM. In the cases without plasma, with main plasma and with residual plasma, the FWHM along the vertical direction is equal to 4.1cm, 6.0cm and 6.9cm, respectively. These values significantly differ from the FWHM in the previous series of experiments. This can be explained by the different poloidal position and as a result different toroidal distance between the source and the detector. The integral in a.u. of the presented profiles equals 1.75, 1.56, and 1.41 for Fig.8.12, 8.13 and 8.14. However, this difference can be easily explained by the fact that the profiles are not complete and only part of the particles and of the current are taken into account.

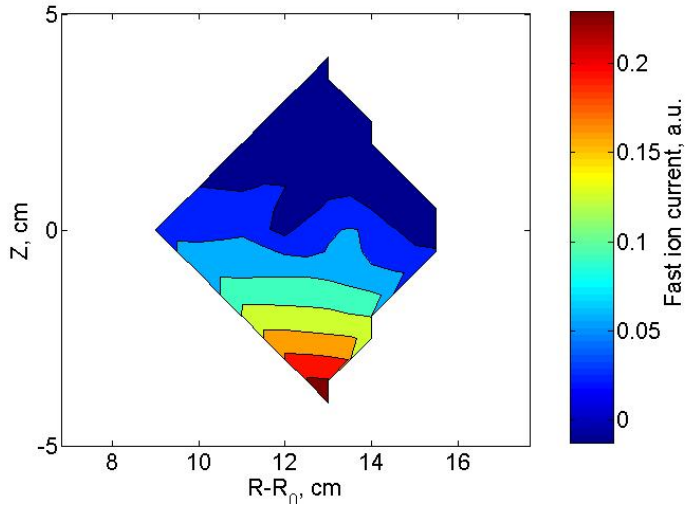

Figure 8.12: The fast ion current density profile in the case without plasma.

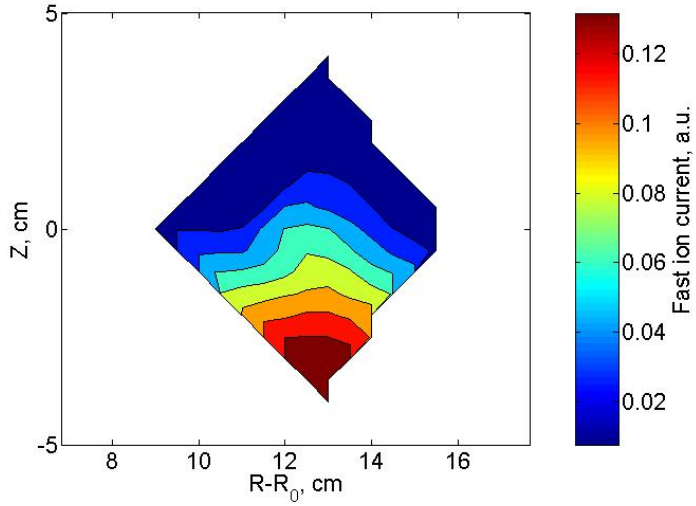

Figure 8.13: The fast ion current density profile in the case with 400W microwave power.

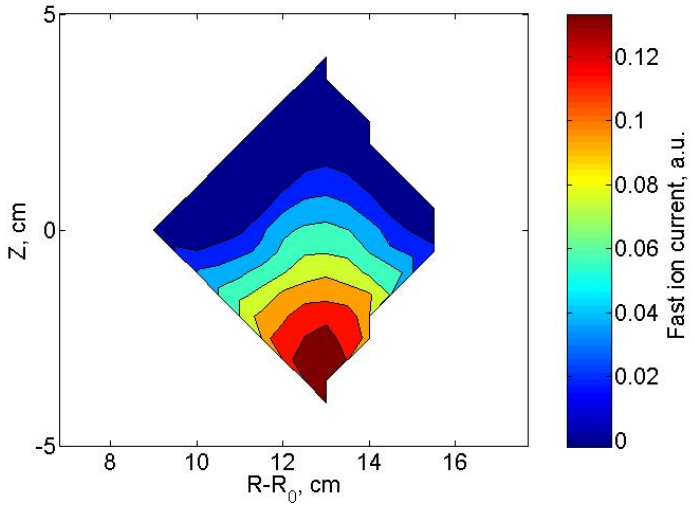

Figure 8.14: The fast ion current density profile in the case with residual value of power 200W.

After these two sets of experiments, the emitter was completely depleted and needed to be replaced. Also the parts of the source, which were made of aluminium, were changed with parts made of molybdenum. All these changes could lead to a slightly different geometry, and as a result to slightly different angular and, probably, energy distributions compared with the first set of experiments.

The rest of the experiments were conducted in the specific conditions described at the beginning of this chapter.

In the next experiment, the energy of the fast ions remained fixed at 300eV and the ion current on the external grid of the source was equal to 1.9μA. 98 discharges were operated for the scan, to obtain an almost full coverage of the profiles. The fast ion current density profile in the case without plasma is presented in Fig.8.15. The profile is not perfectly centered because of a small misalignment of the source relative to the toroidal direction. The maximum is situated at $R - R_0 = 12.5cm$, $Z = 6cm$. The profile is elongated vertically: the vertical FWHM is equal to 4.7cm and the radial one to 2.7cm. The asymmetry measures for radial and vertical directions are -0.4cm and 0.4cm.

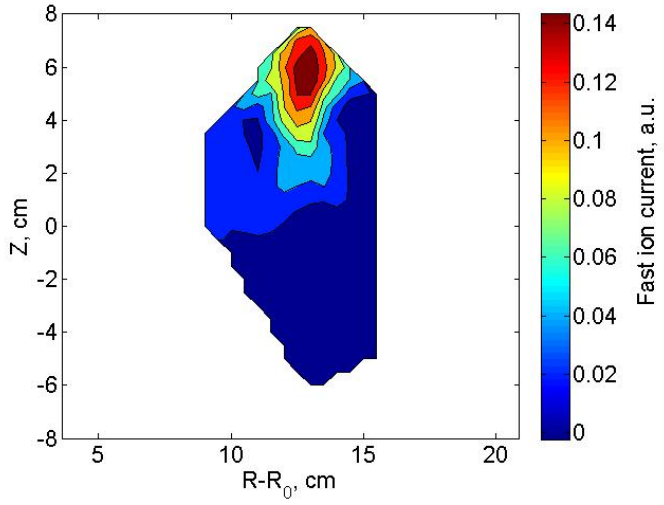

Figure 8.15: The fast ion current density profile in the case without plasma, the fast ion energy is equal to 300eV.

The fast ion current density profile with the presence of plasma created by 400W of microwaves is shown in Fig.8.16. The maximum of the profile shifts downward by 2.5cm, resulting at $R - R_0 = 12{,}5cm$, $Z = 3.5cm$. The profile is broader than in the case without plasma: the radial FWHM is 3.0cm and vertical one is 6.0cm. The asymmetry measures are still small: 0.3cm radially and -0.5cm vertically.

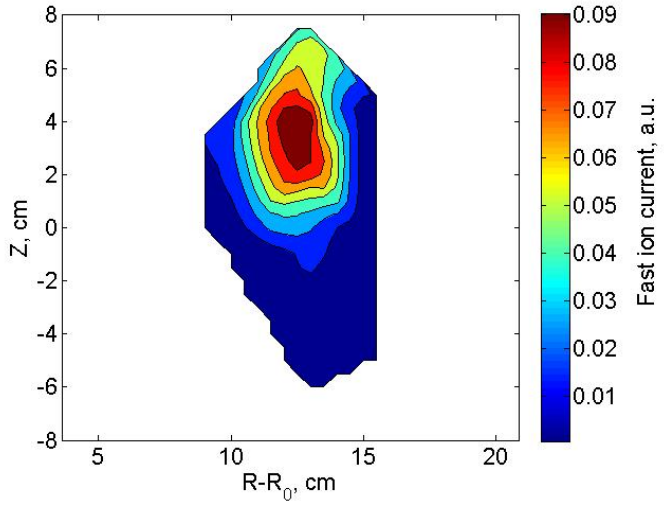

Figure 8.16: The fast ion current density profile in the case with 400W microwave power, the fast ion energy is equal to 300eV.

In Fig.8.17 the fast ion current density profile in the case with the presence of plasma produced by residual 200W microwave power is presented. The maximum of the profile remains at the same poloidal position as in the previous case ($R - R_0 = 12.5cm$, $Z = 3.5cm$). The width of the profile, on the other hand is slightly smaller: radial FWHM is 2.9cm and vertical one is 5.7cm. The asymmetry measure along the vertical direction increases: -0.6cm, while along radial direction it remains small (0.2cm).

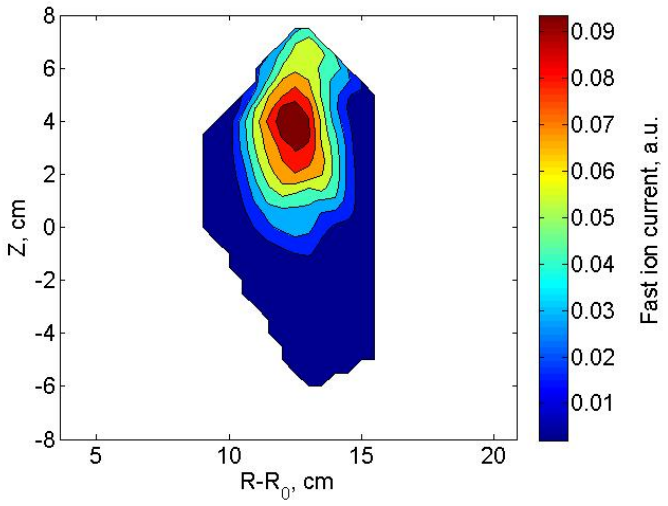

Figure 8.17: The fast ion current density profile in the case with residual value of power 200W, the fast ion energy is equal to 300eV.

The integrals of the profiles presented in Fig. 8.15, 8.16 and 8.17 are equal to 2.1, 1.96 and 1.89 in a.u.. Thus within 21% accuracy, there is conservation of the particles between these profiles.

To investigate the effect of the fast ion energy on the interaction with the plasma, in the next set of discharges we increased the fast ion energy up to 600eV. As a consequence, the fast ion velocity and current are increased. The ion current on the external grid of the source was equal to 2.8μA. 93 discharges were run in this scenario to construct the profiles.

Fig.8.18 shows the profile of fast ion current density in the case without plasma. The maximum is moved, with respect to the previous series of shots, because the source was turned a little for better toroidal alignment, and situated at $R - R_0 = 13.5cm$, $Z = 2cm$. The profile is more vertically elongated: the vertical FWHM is 5.3cm and the radial FWHM is

2.5cm. As we will conclude later the higher elongation can be explained by the higher spread in the fast ion velocity distribution function. The profile is almost symmetric vertically $\delta_Z = 0.2cm$ and has small radial asymmetry $\delta_R = 0.5cm$.

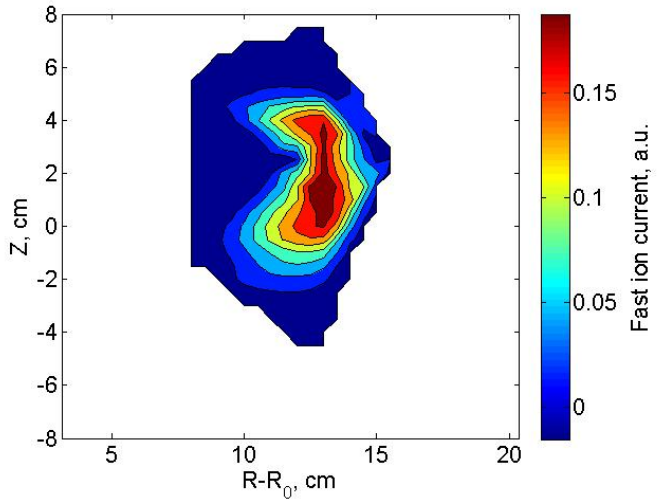

Figure 8.18: The fast ion current density profile in the case without plasma, the fast ion energy is 600eV.

On the next figure (Fig.8.19) the fast ion current density profile in the presence of plasmas produced with 400W of microwave power is presented. The maximum of the profile slightly shifts inwards: $R - R_0 = 13cm$, $Z = 2cm$. The width of the profile is increased, and the profile becomes even more elongated: the vertical FWHM is 9.0cm, and the radial one is 3.1cm. The asymmetry measure along the vertical direction is increased to 0.5cm, along the radial direction it is reduced to -0.4cm.

The last fast ion current density profile in this series of discharges was obtained with the residual power, 200W of microvawes (Fig.8.20). The maximum of the profile shifts slightly: $R - R_0 = 13.5cm$, $Z = 2.5cm$. As could be expected, the spread of the profile is between the case with the main plasma and the case without plasma: the radial FWHM is equal to 2.6cm and the vertical one to 7.5cm. The profile has a vertical asymmetry of $\delta_Z = 0.7cm$, and a radial asymmetry measure equal to 0.3.

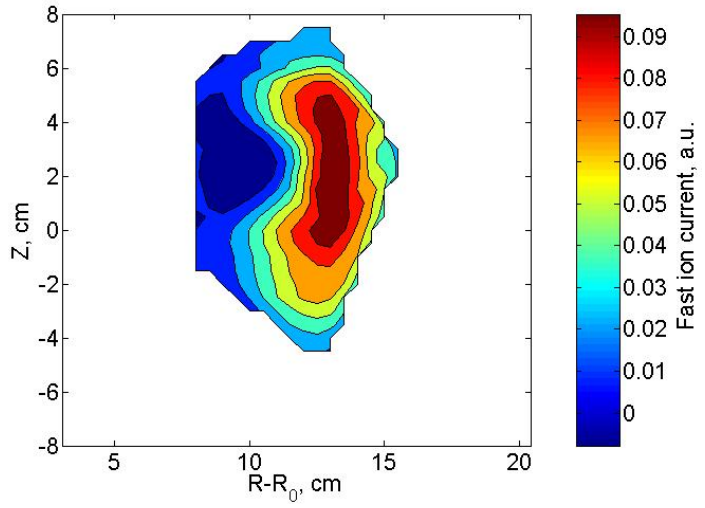

Figure 8.19: The fast ion current density profile in the case with 400W microwave power, the fast ion energy is 600eV.

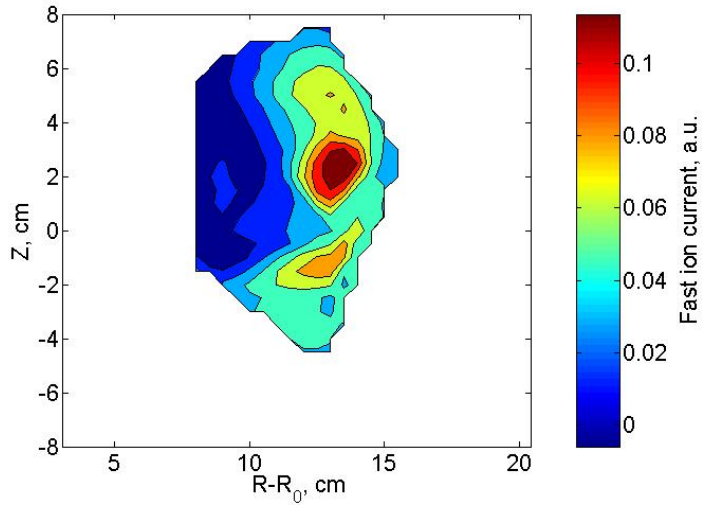

Figure 8.20: The fast ion current density profile in the case with residual value of power 200W, the fast ion energy is 600eV.

Within 33% accuracy the integral of these three profiles (Fig.8.18, 8.19 and 8.20) is conserved (2.94, 3.23 and 2.93 in a.u. correspondingly).

After these two series of discharges, the emitter was depleted. We changed it, leaving all other parts untouched, nevertheless imperfect positioning of the emitter inside the source could lead to small changes in angular and energy distribution of the fast ions.

The new emitter showed higher ion current than the previous two. The ion current on the external grid of the source was about 16.8μA. To verify the efficiency of the source with the new emitter we repeated the experiments in a blob region with a fast ion energy of 300eV. 65 discharges were run to this aim. The fast ion current density profile for the case without plasma is presented in Fig.8.21. Note that the profile is not complete due to a slight misalignment of the source in the toroidal direction. The maximum of it is at $R - R_0 = 11cm$, $Z = -0.5cm$. The radial FWHM is equal to 1.6cm.

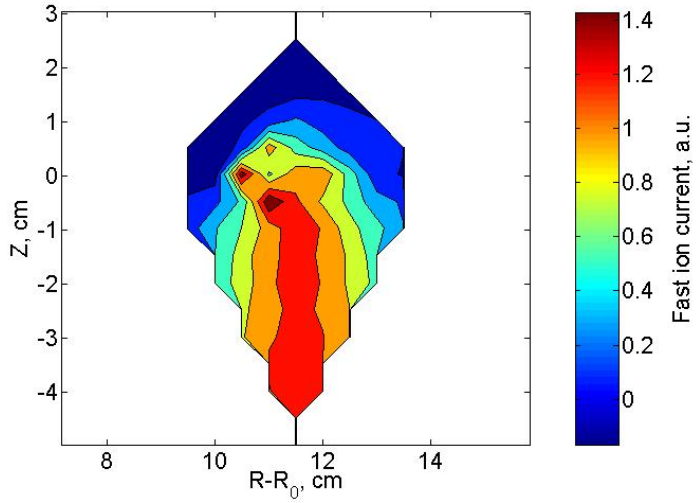

Figure 8.21: The fast ion current density profile in the case without plasma, the fast ion energy is equal to 300eV.

In the case with the main plasma the fast ion current density profile (Fig.8.22) shifts downwards by 3.5cm. Thus the maximum is situated at $R - R_0 = 11.5cm$, $Z = -4cm$. Unfortunately, as the profile is not complete, we cannot calculate the profile width.

In a case with plasma created by residual magnetron power the fast ion current density profile remains almost unchanged (Fig.8.23).

The integrals of these profiles (Fig.8.21, 8.22 and 8.23) are equal to 13.81, 10.81 and 10.47 in a.u.. The next experiment was conducted in a mode region.

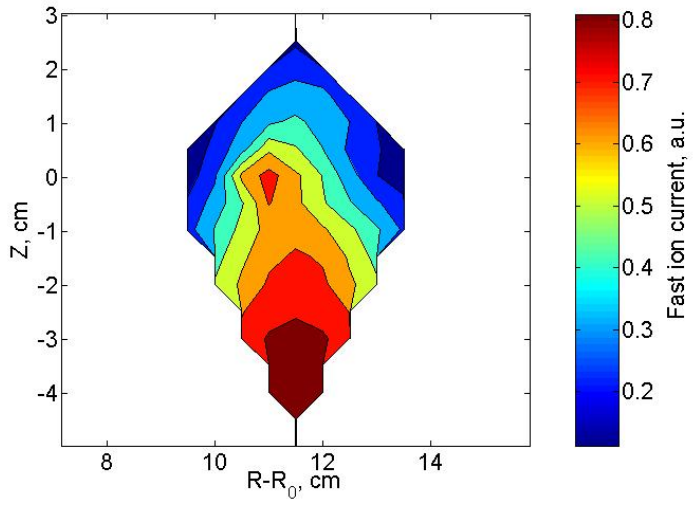

Figure 8.22: The fast ion current density profile in the case with value of power 400W, the fast ion energy is equal to 300eV.

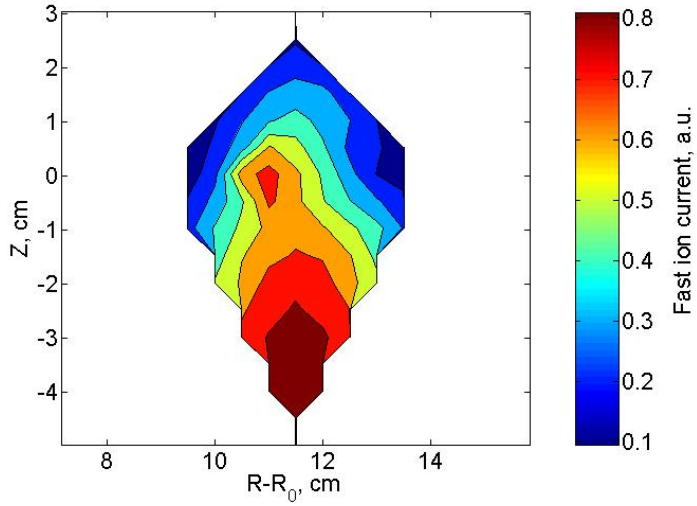

Figure 8.23: The fast ion current density profile in the case with residual value of power 200W, the fast ion energy is equal to 300eV.

The experiments in a blob region show that the fast ion current density profile is elongated and that the elongation depends on the fast ion energy. The maximum of the profile for the 300eV fast ion energy shifts downward with respect to the case without plasma with the normal direction of the magnetic field and upward with an inverted field. For the 600eV the maximum stays in the same poloidal position. The vertical and radial width increase for both 300eV and 600eV with respect to the cases without plasma.

8.5 Experiments in the mode region

The second interesting region of the plasma poloidal cross-section is the mode region, where density fluctuations are dominated by coherent oscillations. To compare the fast ion behavior in this region with the behavior in the blob region we performed experiments with 300eV fast ion energy near $R = R_0$.

A higher current from the third emitter made it possible for us to conduct these experiments in the mode region, where the plasma higher temperature and density (Fig.8.2 and 8.3) increase the noise on the double gridded energy analyzer, which is roughly 5 times higher than in the blob region.

59 discharges were run to construct the fast ion density profiles. The profile in the case without plasma (Fig.8.24) has a maximum at $R - R_0 = 0.5cm$, $Z = 0.3cm$, and is less elongated than in the blob region. This observation could be due to the shorter distance traveled by the fast ions between the source and detector (22.4cm instead of 24.7cm). The radial FWHM is equal to 1.5cm and the vertical one to 2.0cm. The ratio of vertical FWHM to the radial one is 1.4, this ratio for the blob region is 1.7. This ratio quantifies the elongation of the profile. It is equal to 1 for the circular profile. The profile is skewed vertically upwards ($\delta_Z = 0.69cm$) and has a small radial asymmetry of $\delta_R = -0.26cm$.

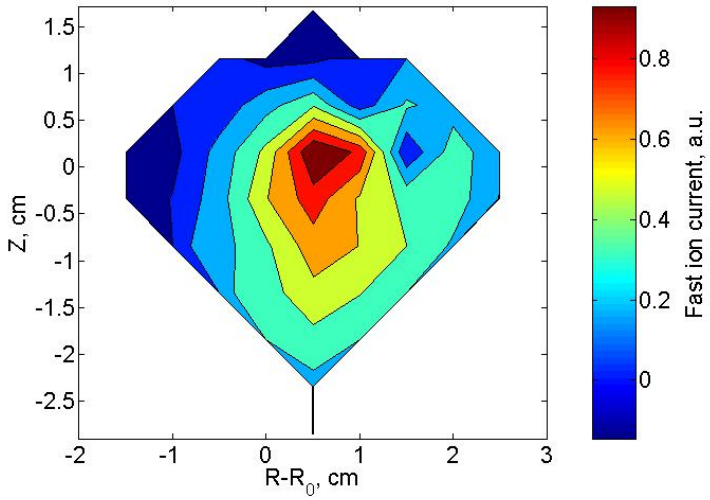

Figure 8.24: The fast ion current density profile for the case without plasma, the fast ion energy is equal to 300eV.

The fast ion density profile during the main plasma phase is shown in Fig.8.25. The maximum of the profile slightly moves vertically, $R - R_0 = 0.3cm$, $Z = 0.0cm$. The width of the profile increases significantly: the radial FWHM is equal to 1.8cm and the vertical of 3.2cm. The elongation of the profile is also large: the ratio of vertical to radial FWHM is equal to 1.7. The vertical asymmetry is large, $\delta_Z = 1.0cm$, and the radial one is negligible, $\delta_R = 0.0cm$.

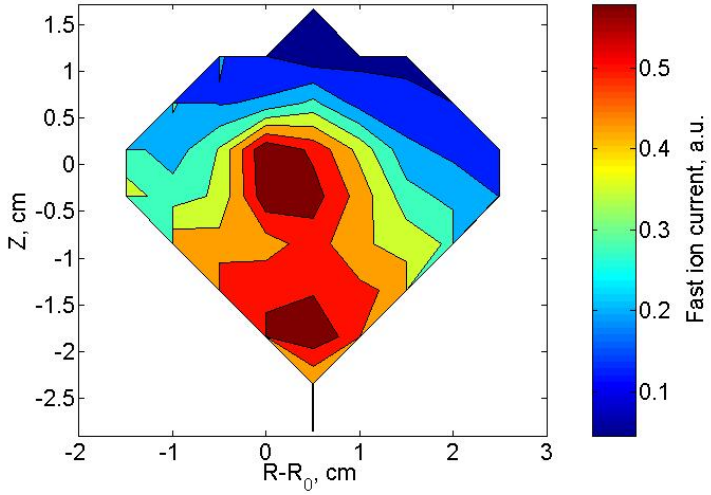

Figure 8.25: The fast ion current density profile for P_{EC}=400W, the fast ion energy is equal to 300eV.

The fast ion current profile in the presence of residual plasma is shown in Fig.8.26. The maximum of the profile does not change significantly with respect to the previous cases (Fig.8.24 and 8.25) $R - R_0 = 0.0cm$, $Z = 0.3cm$. The width of the profile is intermediate between that of the profiles with main plasma and of those without plasma. The radial FWHM is equal to 1.7cm and the vertical one is 2.8cm. The asymmetry measures along the radial and vertical directions are -0.3 and 0.7, respectively.

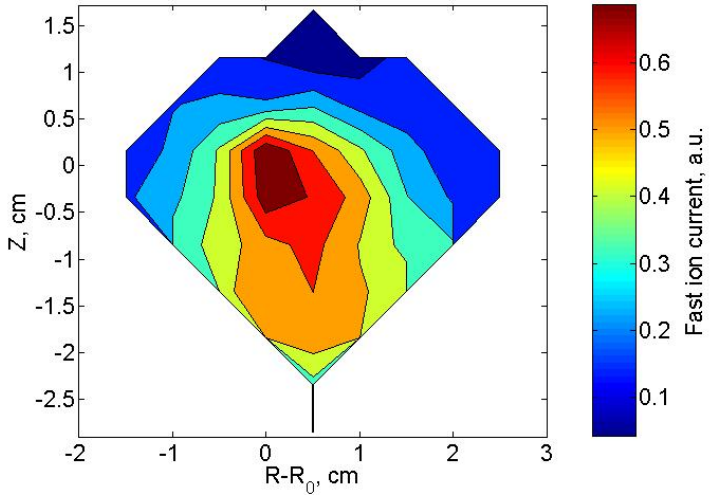

Figure 8.26: The fast ion current density profile for P_{EC}=200W, the fast ion energy is equal to 300eV.

The integral of these profiles is conserved within ~40% accuracy. They are equal to 3.86, 4.22 and 4.22 in a.u. for profiles in Fig.8.24, 8.25 and 8.26, in that order. In general, the experiments in the mode region show that profiles are less spread and less elongated with respect to the experiments in the blob region.

8.6 Summary

The FWHM, poloidal position of the maximum (R_M, Z_M) and asymmetry measure (δ_R, δ_Z) for profiles measured in the different conditions are summarized in table8.2. In all these experiments the plasma clearly affects the fast ion current density profile: the vertical and radial spread of the profiles is larger in the case with plasma than without plasma. The vertical position of the maximum in the plasma shifts downwards with respect to the case without plasma when the fast ion beam propagates in the blob region and the fast ion energy is equal to 300eV. In the other cases the vertical position of the maximum remains unchanged. The effect of the plasma on the asymmetry measure is not clear, but remains rather small in most of these experiments.

About 44% of the accelerated ions are trapped by the external grid of the source. The other particles fly through the plasma and are measured by the double gridded energy analyzer.

The integrals of the measured profiles should be propotional to the fast ion current on the external grid of the detector, asuuming no losses (e.g. charge exchange etc.). The measured dependence of the integrals under the measured profiles upon the ion current on the external grid is presented in Fig.8.27. For all profiles this dependence is linear except for two experiments in which the profiles were not completely reconstructed and, as a result, only a fraction of the fast ions were captured by the detector.

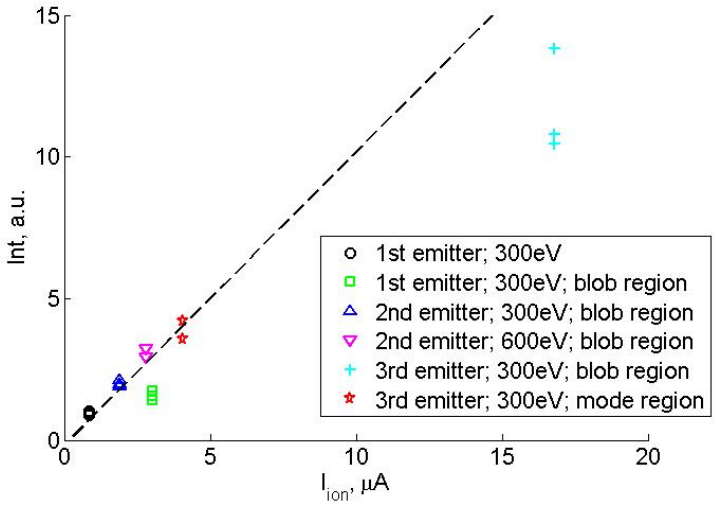

Figure 8.27: The integrals of the measured current density profiles vs fast ion current on the external grid of the source.

Table 8.2

# emitter	P_{EC}, W	E, eV	Note	Figure	ICEG, μA	Integral, a.u.	Radial FWHM, cm	Vertical FWHM, cm	R_M, cm	Z_M, cm	δ_R, cm	δ_Z, cm
1	0	300		8.8	0.85	0.98	2.7	2.6	3.0	0.5	0.1	0.0
1	0	300	B_T	8.9	0.85	0.93	2.3	2.3	3.0	-1.0	-0.3	-0.4
1	0	300	B_T+B_V	8.10	0.85	1.04	2.0	3.3	3.0	-1.0	0.2	-0.8
1	400	300	B_T+B_V+P_{EC}	8.11	0.85	0.88	2.4	2.3	2.5	-0.3	0.0	0.1
1	400	300	B	8.13	3.01	1.56		6.0*	13.0	-3.5		0*
1	200	300	B	8.14	3.01	1.41		6.9*	13.0	-4.0		0*
1	0	300	B	8.12	3.01	1.75		4.1*	13.0	-4.0		0*
2	400	300	B	8.16	1.9	1.96	3.0	6.0	12.5	3.5	0.3	-0.5
2	200	300	B	8.17	1.9	1.89	2.9	5.7	12.5	3.5	0.2	-0.6
2	0	300	B	8.15	1.9	2.1	2.7	4.7	12.5	6.0	-0.4	0.4
2	400	600	B	8.19	2.8	3.23	3.1	9.0	13.0	2.0	-0.4	0.5
2	200	600	B	8.20	2.8	2.93	2.6	7.5	13.5	2.5	0.3	0.7
2	0	600	B	8.18	2.8	2.94	2.5	5.3	13.5	2.0	0.5	0.2
3	400	300	B	8.22	16.8	10.81			11.5	-4.0		
3	200	300	B	8.23	16.8	10.47			11.5	-4.0		
3	0	300	B	8.21	16.8	13.81	1.6*		11.0	-0.5	-0.4*	
3	400	300	M	8.25	4.06	4.22	1.8	3.1	0.3	0.0	0.0	1.0
3	200	300	M	8.26	4.06	4.22	1.7	2.8	0.0	-0.3	-0.3	0.7
3	0	300	M	8.24	4.06	3.59	1.5	2.0	0.5	0.3	-0.3	0.7

* - the profiles were not complete. Note: B_T and B_V mean the presence of toroidal and vertical field; B and M mean experiment in the blob and mode region.

Chapter 9

Comparison with the simulations

To understand the fast ion beam behavior in the presence of plasma turbulence we compare the measured profiles with the simulated ones. Following the experiments, we will start the simulation in the absence of plasma, then we will simulate profiles in the blob region for fast ion energies of 300eV and 600eV, and we will finish with the simulation of the fast ion beam (at 300eV) in the mode region.

9.1 Simulations of the ion beam behavior in the case without plasma

Let us start with the experiment without plasma and without magnetic fields. Here we can use the Matlab simulation with electric and magnetic fields equal to the 0 and the collisional term switched off. We assume that the energy spread of the beam is equal to 0. This is a reasonable assumption, as the spread in energy is defined by $2kT \sim 0.2eV$ [73], where k is the Boltzmann constant and T is the temperature of the emitter. First, we choose the angular spread in the simulation to match the experimental profile presented on Fig.8.7. We obtain a simulated FWHM of 2.5cm for both directions that is very close to the experimental values, 2.7cm and 2.6cm for the radial and vertical FWHM, respectively.

The simulated profile of the fast ion current density is shown in Fig.9.1. The position of the simulated profile centre is shifted outwards by 2.8cm from the initial position in the centre of the vacuum chamber, due to the fact that the vacuum chamber has a toroidal shape and the fast ion beam propagates in this case along straight lines. The simulated profile centre at $R - R_0 = 2.8cm$, $Z = 0cm$ is close to the experimentally determined position at $R - R_0 = 3cm$ $Z = 0.5cm$. This small difference could be simply explained by an error in the source

alignment with the toroidal direction.

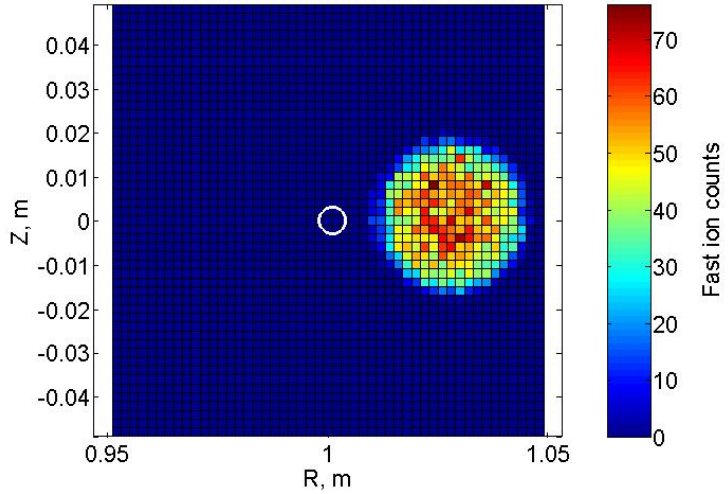

Figure 9.1: The fast ion current profile for the case without magnetic fields and without plasma for the fast ion energy of 300eV.

As a second step, as it was done in the experiment, we included the toroidal field in the simulation (Fig.9.2). This shifts the profile centre downward in the direction of the ion toroidal drift by 1.7cm and inward by 1.5cm, because in this case the ion beam follows the toroidal direction. In the experiment (Fig.8.9) the radial shift with respect to the case without magnetic fields was 0.0cm and the vertical shift 1.5cm, similar to the simulation. The vertical displacement of 1.7cm could be also verified by drift theory: $Z_d = \frac{L}{\upsilon_{ion}}\upsilon_d = L\sqrt{\frac{m}{2E}}\frac{m}{eBR}\upsilon_{ion}^2 = 1.7cm$, where $L = 22.4cm$ is the toroidal distance, υ_{ion} and υ_d are the ion velocity and the drift velocity, respectively.

In the case with toroidal field, the fast ions that have a finite velocity component perpendicular to the magnetic field are subject to cyclotron motion. As a result, these ions deviate less from the centre of the profile and thus the width of the profile should decrease. In the simulation of this case, both radial and vertical FWHM decrease by 0.7cm. In the experiment the FWHM decreases by 0.4cm in the radial and by 0.3cm in the vertical direction.

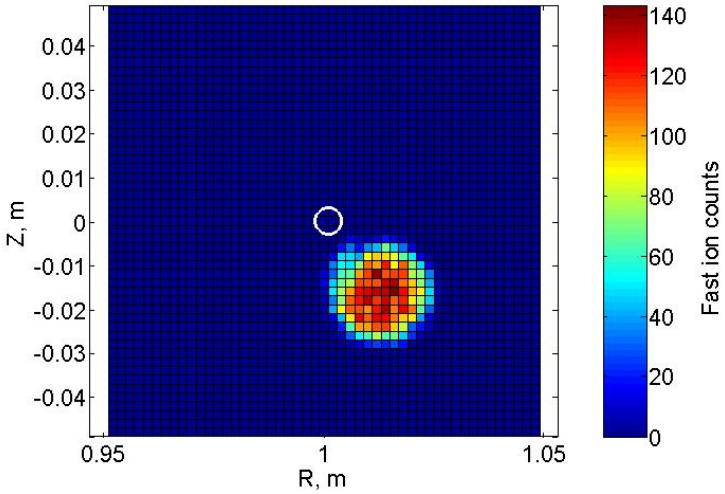

Figure 9.2: The fast ion current profile for the case with toroidal magnetic fields and without plasma.

The next step is to run simulations with toroidal and upward vertical magnetic fields (Fig.9.3) to simulate the profile presented in Fig.8.10. The addition of the vertical field does not change the FWHM, which is reasonable because the vertical field is small compared to the toroidal one, and has only minor effect on the cyclotron motion. On the other hand, the vertical field is observed in the simulation to shift the beam inward by 0.1cm and the additional radial velocity to shift the beam upward by 0.3cm. In the experiment, the maximum of the profile has the same position as in the case without vertical field, but its shape becomes elongated in the inward and upward direction.

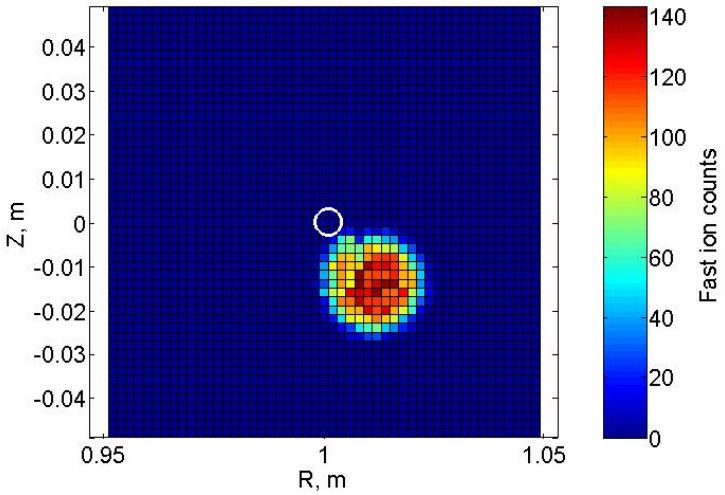

Figure 9.3: The fast ion profile (with toroidal and vertical magnetic fields, no plasma).

In the experiment the next step was the addition of plasma created by microwaves. To simulate the plasma interaction with the fast ion beam, we added in the simulation the collisions of fast ions with the ions from the background plasma (chapter 8.1). The results of this simulation are presented in Fig.9.4. The collisions increase the FWHM only by 0.1cm in both directions. In the experiment, the radial FWHM increases by 0.4cm and the vertical one decreases by 1.0cm. In addition, the position of the profile maximum moves upward in the experiment by 0.8cm.

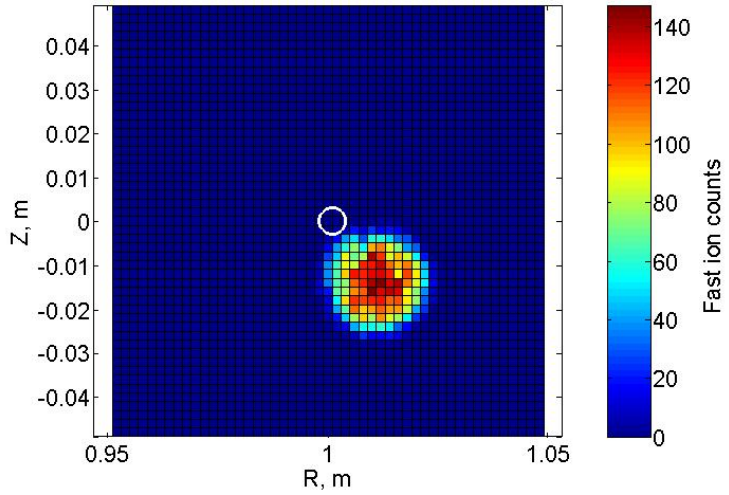

Figure 9.4: The fast ion current profile for the case with toroidal and vertical magnetic fields with taking into account collisions between fast ions and ions from the background plasma.

The addition of a constant radial electric field of 40V/m comparable with the experimentally measured shifts the profile outward by 0.1cm and downward by 0.1cm but does not change the width of the profile (Fig.9.5) and cannot explain the experimental profile.

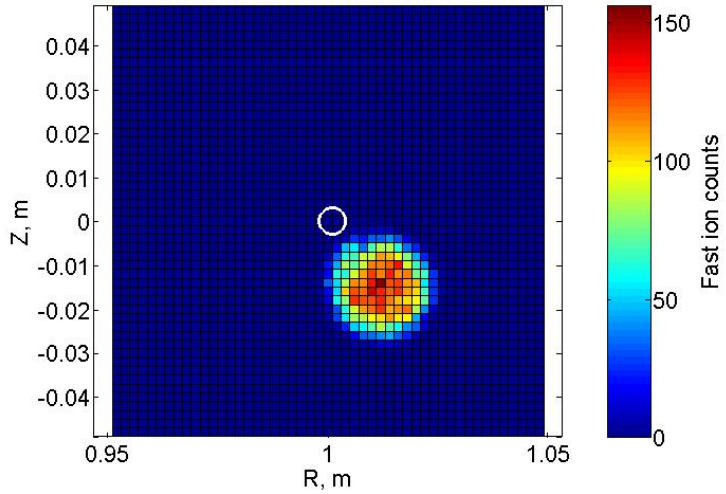

Figure 9.5: The fast ion current profile for the case with the toroidal and vertical magnetic fields taking into account collisions between fast ions and ions from the background plasma and with a constant radial electric field of 40V/m.

Thus this Matlab model can qualitatively explain the behavior of the fast ion beam only in the absence of plasma, but not in the presence of plasma.

We can put forward a few reasons why the collisions with neutrals cannot explain the disagreement between the simulation and experiments. First of all, the mean free path for fast ions in the neutral background gas for the pressure of 2×10^{-5}mbar is approximately 1m, which is much smaller than the distance traveled by the ions. Second, all experiments (with and without fields) were conducted with background gas, so the spreading from the collision with neutrals is already taken into account in the simulation when the angular spreading is chosen to match the experiment. Another effect that is not taken into account in the simulation is the electrostatic sheath between the external grid of the source and plasma. However, the effect of the sheath should be negligible because the plasma potential is much smaller than the fast ion energy and the electric field in the sheath is parallel to the toroidal magnetic field. Thus there remains no other explanation but turbulent electric fields that can account for the experimentally observed behavior of the fast ion beam in the presence of plasma.

9.2 Simulations of the fast ion beam behavior in the blob region

Contrary to the Matlab model, the C++ simulation takes into account the turbulent electric field. First of all, for the conditions described at the beginning of this chapter and for the fast ion source situated at $R - R_0 = 10cm$, $Z = 0cm$ we calculated the radial and vertical FWHM of the simulated profiles as a function of angular and velocity spread (Fig.9.6 and 9.7). The radial FWHM remains almost unchanged when the standard deviation of the angular distribution varies from 0.2rad to 0.8rad, and the standard deviation of the velocity distribution varies from $0.2\upsilon_0$ to $0.8\upsilon_0$, where $\upsilon_0 = \sqrt{\frac{2E}{m}}$ is the fast ion velocity which corresponds to a fast ion energy of $E = 300eV$. The vertical FWHM varies from 2cm to 4cm when the angular and velocity spread varies from 0.2rad to 0.8rad and from $0.2\upsilon_0$ to $0.8\upsilon_0$. The vertical FWHM has a maximum for an angular standard deviation equal to 0.2rad and a velocity standard deviation of $0.8\upsilon_0$. These values were used for the simulation of the experiment as they give FWHM that are the closest to the measured ones (Fig.8.16).

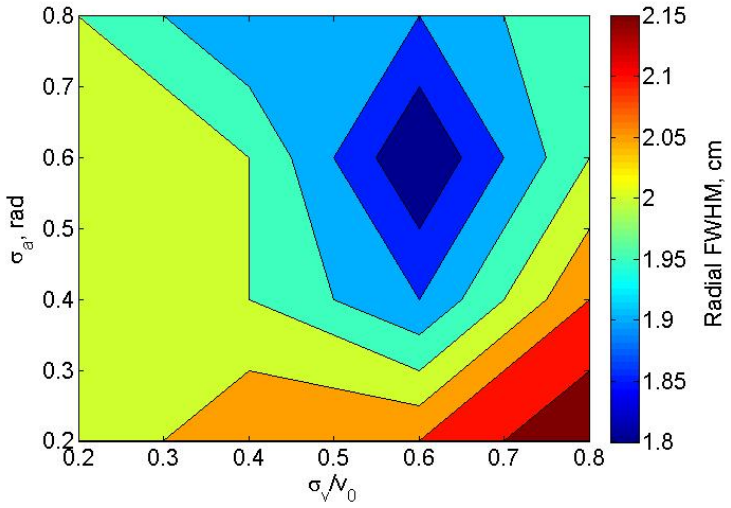

Figure 9.6: The radial FWHM (in [cm]) as a function of the angular standard deviation and velocity standard deviation.

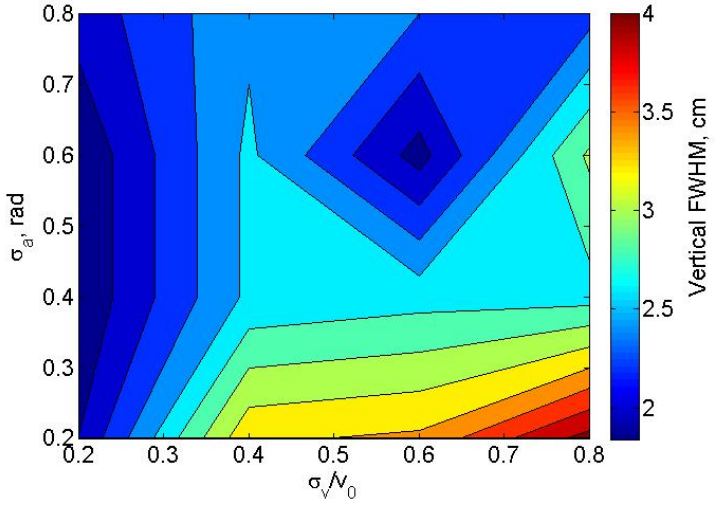

Figure 9.7: The vertical FWHM (in [cm]) as a function of the angular standard deviation and velocity standard deviation.

Thus, to simulate the fast ion current density profile that is elongated vertically one should assume a rather large spread in the initial velocity distribution. Theoretically, in ideal conditions the spread in energy is defined by the two temperatures of the emitter (~0.2eV). In reality, the energy spread can be modified by the plasma potential and by the fact that the potential of the emitter is modulated during the discharge.

On Fig.9.8 the modulated potential on the output of the power supply is presented. The frequency of the modulation is 1kHz. With this high frequency we have 1000 periods during one discharge, obtaining adequate statistics for the data analysis. The modulation period of 1ms is comparable with the rise time of the modulated high voltage power supply, which is used in the source electronics. The disadvantage of the fast modulation is that the potential on the emitter is not perfectly rectangular and as a consequence we have intermediate values of the potential between 300V and 0V. This effect can significantly modify the spread in the velocity distribution.

The second effect that can modify the velocity distribution is connected with the plasma potential. The external grid of the source is at ground potential, which is different from the plasma potential by 4V in the blob region and by 15V in the source region, thus fast ions decelerate in the region between the external grid and the plasma. The velocity distribution

then shifts to the left by the plasma potential, changing the relative spread in the velocity distribution. However, for fast ion energies much higher than the plasma potential, this effect should be negligible.

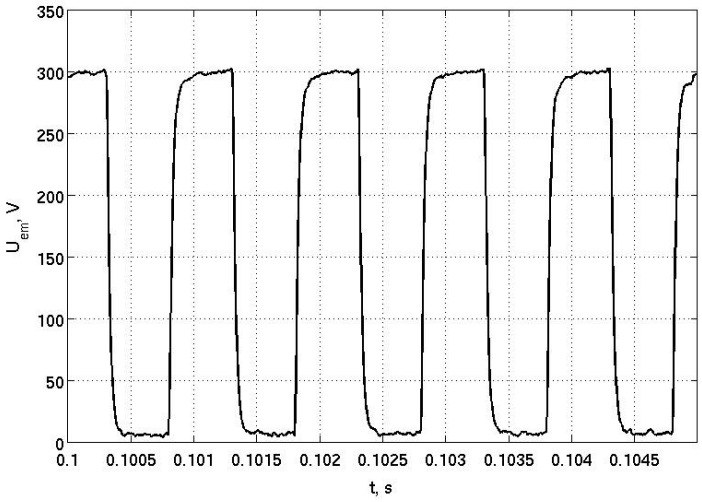

Figure 9.8: The modulated potential on the emitter during the discharge.

The first scenario we considered for the simulation of the experiment is the case without plasma, in the blob region, and with the fast ion energy equal to 300eV (Fig.8.15). For this we set the electric field equal to 0. As the standard deviation of the velocity profile is relatively large, we cannot compare the shape of the simulated particle distribution with the experimental fast ion current density profile like we did in the previous simulations. In Fig.9.9 the fast ion current density profile is presented. The radial and vertical FWHM are equal to 1.2cm and 3.6cm. Thus the simulated profile has smaller widths in both directions than the experimental profile. The maximum of the profile is situated at $R - R_0 = 10cm$, $Z = 0.3cm$. The asymmetry measures in the radial and vertical directions are equal to 0.0cm and -1.4cm, respectively. In the experiment the asymmetry measure is different: -0.4 for the radial direction and 0.4 for the vertical one. Thus, in the vertical direction, the asymmetry measures in the experimental and simulated profiles have opposite signs.

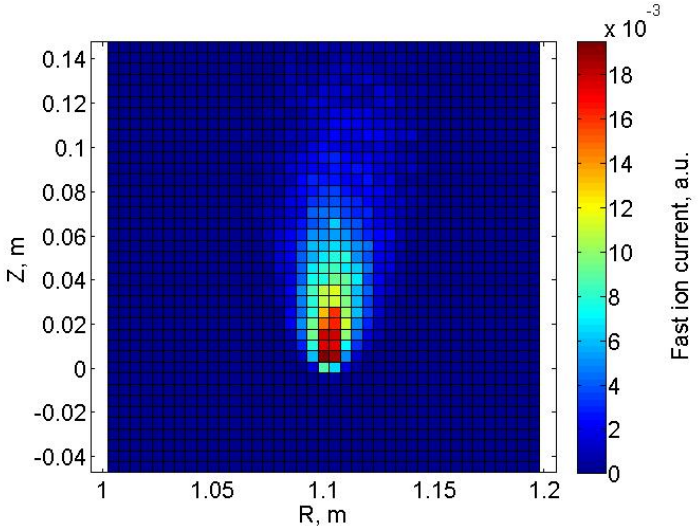

Figure 9.9: The simulated fast ion current density profile in the blob region for the case when the electric field is equal to 0 and the fast ion energy of 300eV.

To see the effect of turbulence, we run the simulation with a turbulent electrical field obtained by the simulation of interchange turbulence based on the Braginskii equations and developed for the exact same TORPEX scenario [74] (Fig.9.10). The maximum of the profile shifts upwards, in the direction of the $\vec{E} \times \vec{B}$ drift, by 0.5cm. In the experiment (Fig.8.16) the maximum shifts downwards by 2.5cm. One of the possibilities to explain this disagreement is the fact that the simulation is not self-consistent, thus the effect of the fast ions on the plasma is not taken into consideration. The radial FWHM increases by 0.9cm and the vertical FWHM remains almost unchanged (3.9cm). In [66], it was concluded that the radial spread is the key element in the study of the effect of the turbulence on the distribution of the fast ions. In the experiments both the radial and vertical FWHM increase by 0.3cm and by 1.3cm, respectively, with respect to the profile without plasma. One of the possible explanations of the vertical FWHM increase in the experiment is a modification of the fast ion velocity distribution function by the plasma. The asymmetry measures in the radial direction in the experiment and the simulation are small: 0.3cm and -0.2cm. In the vertical direction they are similar: -0.6cm in the simulation and -0.5cm in the experiment.

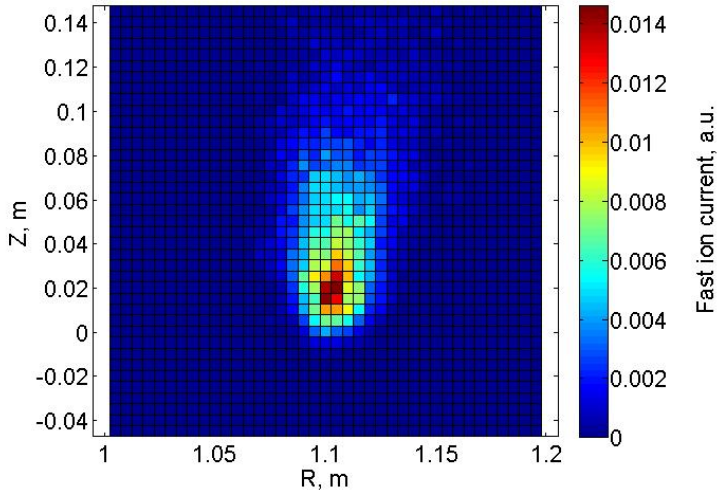

Figure 9.10: The simulated fast ion current density profile in the blob region for the case with the turbulent electric field and the fast ion energy of 300eV.

Simulations with double fast ion energy were run for the two experimental cases with and without plasma presented in Fig.8.18 and 8.19. First of all, let us consider the case when the electric field in the simulation is set to 0 (Fig.9.11). The profile is much more elongated compared with the 300eV case: the radial FWHM increases slightly by 0.2cm and the vertical FWHM increases by more than a factor of two, to 9.1cm. In the experiment, the same qualitative behavior of the vertical FWHM is observed. The simulated profile has a strong vertical asymmetry of $\delta_Z = -3.2cm$, but it is symmetric radially. In the experiment the profile is vertically symmetric and has radial asymmetry.

The simulation with turbulent electric field (Fig.9.12) shows the same qualitative behavior as in the simulation with 300eV fast ion energy. Compared with the simulation with the electric field equal to 0, the maximum is displaced upward by 0.5cm, and the radial FWHM is increased by 0.9cm. In the experiment, with respect to the situation without plasma, the maximum remains in the same poloidal position, and both the radial and vertical FWHM increase. As in the case of 300eV fast ion energy, the experimental and simulated asymmetry measures are not in agreement. In the simulation, the profiles with and without electric field are radially symmetric and have negative vertical asymmetry measure. In the experiment, the profile in the case without plasma is vertically symmetric and has positive radial asymmetry measure, while in the case with plasma the profile has negative radial and

positive vertical asymmetry measures.

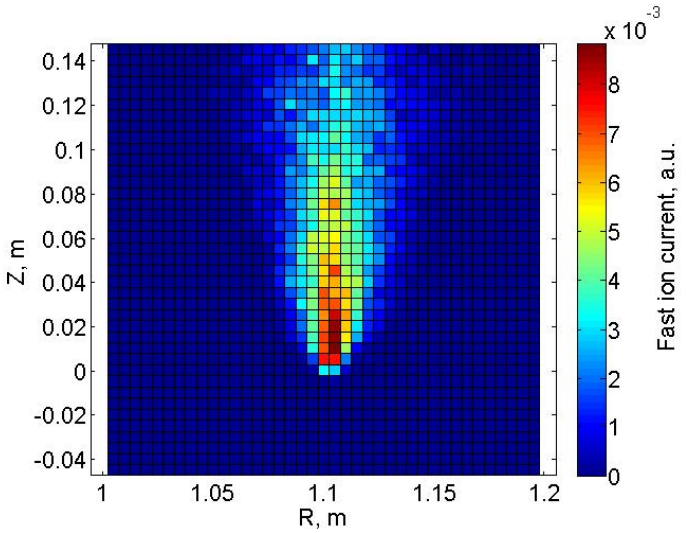

Figure 9.11: The simulated fast ion current density profile in the blob region for the case when the electric field is equal to 0 and a fast ion energy of 600eV.

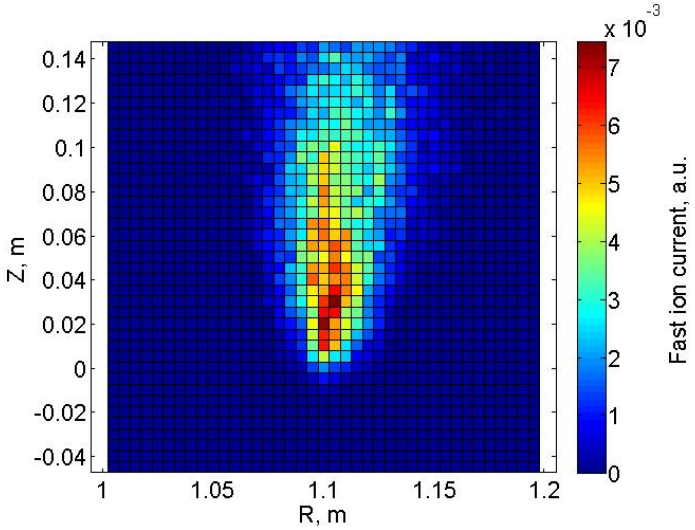

Figure 9.12: The simulated fast ion current density profile in the blob region for the case with the turbulent electric field and a fast ion energy of 600eV.

9.3 Simulations of the ion beam behavior in the mode region

The next simulations were run in the mode region with the fast ion energy of 300eV. The source position in this simulation coincides with the centre of the vacuum chamber. The traveled toroidal distance is shorter by 2.2cm. Although this difference is small compared with the traveled distance of 22.4cm, taking into account the bellows shape of the fast ion

beam due to the cyclotron motion (Fig.7.4), it can significantly change the poloidal profile. The simulation with 0 electric field is presented in Fig.9.13. As in the experiment (Fig.8.24), the profile is less elongated compared to the blob region: the radial and vertical FWHM are equal to 1.5cm and 3.5cm.

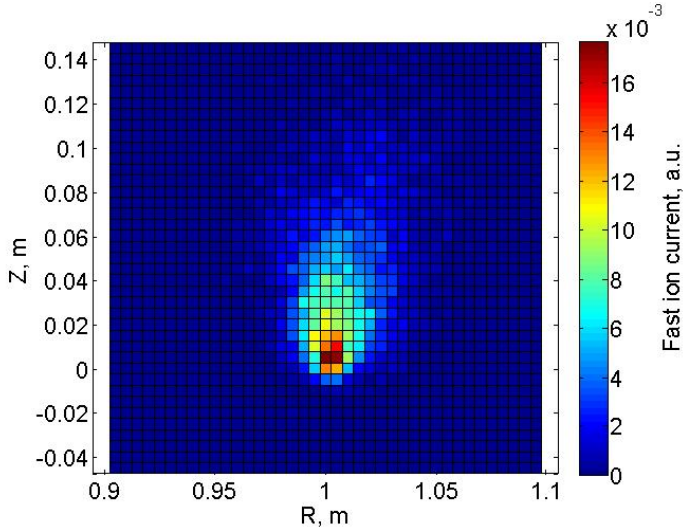

Figure 9.13: The simulated fast ion current density profile in the mode region for the case when the electric field is equal to 0 and the fast ion energy of 300eV.

In the simulation with the turbulent electric field in the mode region (Fig.9.14) the maximum of the profile shifts upward by 0.5cm and outward by 0.5cm, compared to the zero electric field simulation, while the vertical FWHM remains the same and the radial one increases by 1cm. In the experiment with plasma (Fig.8.25) the maximum does not shift significantly and both vertical and radial FWHM increase by 0.3cm and 1.2cm compared to the experiment without plasma.

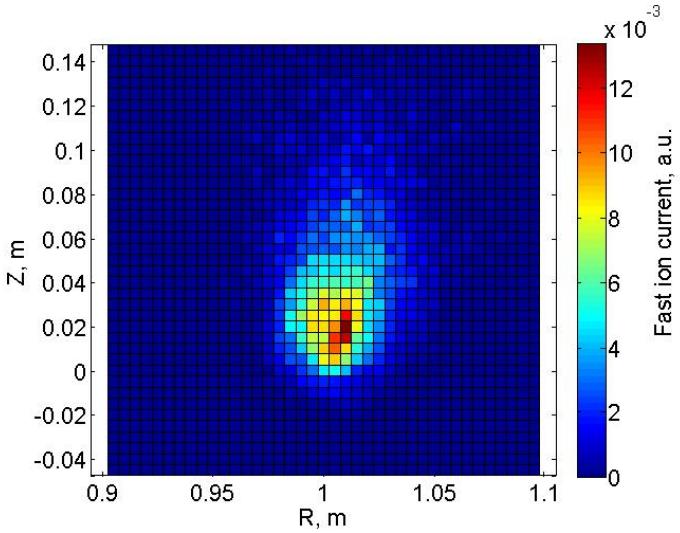

Figure 9.14 The simulated fast ion current density profile in the mode region for the case with the turbulent electric field and the fast ion energy of 300eV.

A summary of the simulation results is presented in Table9.1, which has the same notation as in Table8.2.

Table 9.1.

Electric field	E, eV	Note	Figure	Radial FWHM, cm	Vertical FWHM, cm	R_M, cm	Z_M, cm	δ_R, cm	δ_Z, cm
0	300		9.1	2.5	2.5	2.8	0	0	0
0	300	B_T	9.2	1.8	1.8	1.3	-1.7	0	0
0	300	B_T+B_V	9.3	1.8	1.8	1.2	-1.4	0	0
0	300	B_T+B_V+C	9.4	1.9	1.8	1.2	-1.4	0	0
Constant	300	B_T+B_V+C	9.5	1.8	1.8	1.3	-1.5	0	0
Turbulent	300	B	9.9	2.1	3.9	10	1.8	-0.2	-0.6
0	300	B	9.10	1.2	3.6	10	0.3	0.0	-1.4
Turbulent	600	B	9.11	2.3	8.8	10.3	2.8	0.1	-2.1
0	600	B	9.12	1.4	9.1	10.3	1.3	0.2	-3.2
Turbulent	300	M	9.13	2.5	3.3	0.5	1.8	0.3	-0.1
0	300	M	9.14	1.5	3.5	0	0.3	-0.1	-1.0

Note: B_T and B_V mean the presence of toroidal and vertical field; B and M mean experiment in the blob and mode region and C means that the collisions with background plasma ions are taken into account.

Chapter 10

Discussion of the experimental results

The propagation of the fast ion beam in the vacuum is well characterized by a Matlab based simulation that solves the single particle equation of motion, including an ion-ion collision term, but does not account for plasma collective effects. The simulation qualitatively explains the position of the profile maximum in the case with and without toroidal and vertical magnetic fields. Thus the single particle equation of motion that takes into account only magnetic fields can explain the behavior of the fast ion beam in vacuum.

In the presence of plasma, this simulation cannot explain the experimental profile even when a static electric field and collisions with the background plasma ions are included. Over a toroidal distance of 25cm the collisions of the fast ions with the ions from the background plasma have a minor influence on the fast ion beam. The collisions only increase the FWHM in both directions by 0.1cm. The addition of a constant in time, homogeneous electric field changes only the position of the profile maximum but does not change the profile width. The collisions with neutral gas cannot explain the experimentally observed increase in the beam width in the case with the plasma compared to the case without plasma, because the gas pressure was the same in the experiments with and without plasma. Thus the only factor that can explain the spreading of fast ion beam as it propagates in the plasma is a turbulent electric field.

The C++ simulation, which takes into account a realistic structure and intensity of the turbulent electric field, is used to describe the fast ion beam behavior in the presence of plasma. The simulations show that vertically elongated profiles, which are observed in the experiments in the blob region for a fast ion energy of 300eV and 600eV, and in the mode

region for 300eV, can be explained by a spread in the fast ion velocity distribution. A simple interpretation can be provided: the drift velocity depends on the toroidal ion velocity, $v_d = \frac{m}{eBR} v_{\|}^2$. The spread in the fast ion velocity distribution can be due to the modulation of the source, which in these experiments was not perfectly rectangular (Fig.9.8). This implies that during the modulation the emitter potential takes intermediate values between 0 and the maximum. We should also mention that data presented in Fig.9.8 was taken near the output of the electronics so, due to the resistance of the cable between the electronics and the source and due to the electrical capacity of the cable and the source itself, the modulation potential on the emitter is even less rectangular. Another fact, which supports this explanation of the velocity spread, is the comparison of the experimental profiles obtained with 125Hz modulation frequency (the four first profiles obtained without plasma) and the profiles obtained using 1kHz modulation (the rest of the profiles with and without plasma in blob and mode region). With lower modulation frequency and the same rise time of the high voltage power supply, most of the ions will have the same velocity and the velocity distribution will be narrower. As a consequence, in the experiment, the less elongated profiles are observed with lower frequency modulation.

With the fixed relative velocity spread, the C++ simulation qualitatively explains the shape of the fast ion current density profiles. With the 600eV energy in the blob region the experimental profile has a vertical FWHM a factor of 1.3 higher than in the 300eV case. In the simulation this factor is equal to 2.2. The quantitative disagreement could be explained by the fact that in the simulation the velocity distribution has a Gaussian shape. In the experiment, as discussed above, the velocity distribution has a complicated shape. In the mode region both in the experiment and in the simulation the profile has a more circular shape compared to the blob region.

The C++ simulation qualitatively explains the increase in radial FWHM detected in the experiment with plasma compared to the experiments without plasma. According to [66], such an increase in the radial width of the profile is the key element in the study of the effect of turbulence on the distribution of fast ions. In the experiment, for the cases of 300eV and 600eV fast ion energies in the blob region and 300eV fast ion energy in the mode region, the

increase in the radial FWHM is equal to 0.3cm, 0.6cm and 0.3cm, respectively. In the simulations, for these three cases the increase in the radial FWHM is equal to 0.9cm, 0.9cm and 1.0cm. In [74] it is shown that, the turbulent electric field results in a self-consistent simulation approximately a factor of two higher than the experimental value. Using a more realistic turbulent electric field value one can hope to obtain quantitative agreement with experiments in the increase of the radial FWHM.

The vertical simulated FWHM remains unchanged if we compare the profiles with and without a turbulent electric field. In the experiment, the vertical FWHM increases by 1.3cm, 3.7cm and 1.2cm for the cases: 300eV and 600eV fast ion energies in the blob region and 300eV fast ion energy in the mode region. The most probable explanation is that the plasma modifies the fast ion velocity distribution. In principle the plasma can modify the fast ion velocity distribution by decelerating the fast ions in the sheath between the plasma and the external grid of the source. However, this modification should be negligible because the fast ion energy of 300eV is much higher than the plasma potential (4V in the blob region and 15V in the mode region). An indirect proof for this comes from the observation that the integral of the profiles with and without plasma is approximately conserved (Fig.8.27).

In the experiments, in the case with plasma and 300eV fast ion energy in the blob region, the profile maximum shifts downwards by 2.5cm compared to the case without plasma. In the cases with 600eV in the blob region and 300eV in the mode region, the positions of the profile maximum remain unchanged. In the simulation in these three cases the position of the profile maximum shifts upwards by 0.5cm for all cases compared to the simulation without a turbulent electric field. We have no explanation this disagreement.

The disagreement in the asymmetry measure could be explained by the fact that in the experiment the fast ion velocity distribution has a non-Gaussian shape.

To improve the understanding of the experiment we should use a more realistic electric field in the simulation. A fast ion velocity distribution close to the experimental one should be used. To do this we can measure the velocity distribution experimentally with the double gridded energy analyzer. The effect of all collisions also should be taken into account.

Chapter 11

Conclusions and outlook

This Thesis work addressed the basic question of how a fast (supra-thermal) ion beam interacts with turbulence in a simple magnetized toroidal plasma. The investigation was conducted experimentally using a specially developed miniaturized fast ion source and detector.

As part of this work, possible variations of the plasma and magnetic field topologies were investigated. The first part of the Thesis dealt with the development of ohmic assisted discharges on the TORPEX device. Internal and external rogowskii coils for measuring the total plasma current were developed, calibrated and installed on TORPEX. To measure the plasma current density distribution two small mobile rogowskii coils were constructed. Up to 1kA of plasma current was obtained, although in conditions in which the current channel is unstable. It was shown that the simplest configuration of poloidal coils does not satisfy the equilibrium conditions for the vacuum poloidal magnetic field. Using additional vertical magnetic field coils, discharges with longer plasma current phases were obtained, corresponding to a better match of equilibrium conditions. Future work with ohmic assisted discharges should include the development of an active feedback system, which will control the current in poloidal coils based on measurements of the total plasma current, and experiments with the recently installed more powerful magnetic coil power supply.

The fast ion source was developed using the scheme with accelerating and screen grids. The ions are produced by a source including an aluminosilicate lithium-6 ion emitter having a diameter of 0.6cm. To minimize the divergence of the fast ion beam an optimization of the electric field inside the source was conducted. A simulation of the fast ion motion inside the

source was performed in order to calculate the overall transparency. A second fast ion source, based on the same concept but having a 1.5cm diameter emitter was developed. The larger physical dimensions allow us to obtain a higher fast ion current. The current and life time limitations of the sources are imposed by the emitter. On a dedicated test bench the emitters were characterized and optimized. It was shown that using the Schottky effect the ion current from the emitter can be increased by 2 to 3 times, depending on the extraction electric field.

To detect the fast ion beam we chose to use a detector based on the gridded energy analyzer concept. A scheme with two identical gridded energy alalyzers to better discriminate the signal from background noise extraction was used. The detector allows measurements of the fast ion current density profile and the energy distribution function. A special 2D probe system was developed for the fast ion source and detector to reach practically an entire coverage of the plasma poloidal cross section.

First experiments were conducted without plasma but with different configurations of magnetic fields. Next, the measurements of the fast ion current density profiles were performed in the presence of plasma, in two main poloidal regions: in a blob region, which is caracterized by the propagation of nonlinear structures of higher pressure than the local background plasma, with 300eV and 600eV of fast ion energy, and in a mode region, where the fluctuation spectra are dominated by coherent oscillations, using the 300eV fast ions. In all these experiments the integral of the measured fast ion density current profiles is conserved. Thus on this toroidal path of 25cm the fast ion velocity remains essentially unchanged and no significant particle losses occur.

Using the single particle equation of motion a Matlab based numerical model was developed to help understand the experimental data. This model accounts for the realistic magnetic field and for fast ion collisions with background plasma ions. A homogeneous constant in time electric field can also be introduced. A second model, developed on a C++ platform, incorparates the effects of a turbulent electric field, calculated using a two-fluid code based on the Braginskii equations. This electric field has a realistic structure, but, its fluctuation levels are approximately two times higher than measured.

These models were used to interpret the experimental data. The Matlab based simulation qualitatively describes the fast ion beam behavior with different magnetic configurations in the absence of plasma. The experiments without any magnetic field and without plasma were used to calibrate the model, in particular to find a good estimate of the angular distribution. Under the influence of the toroidal magnetic field the fast ion beam deviates in the direction of the ion toroidal drift and shrinks because of gyromotion. The addition of a weak vertical magnetic field component has negligible effect on the width of the profile and only slightly changes the poloidal position of the profile maximum.

This simple single-particle Matlab model without turbulent fields cannot explain the fast ion current density profiles in the presence of plasma: the collisions with background plasma ions have a negligible effect on the profiles and a static homogeneous electric field can only change the profile maximum position, but does not affect the profile width. The collision with neutrals cannot explain the experimental profiles in the presence of plasma because the neutral pressure remains practically the same in the cases with and without plasma and because the fast ion mean free path for this pressure is around 1m, which is much longer than the toroidal path of the fast ions. The only remaining factor that can affect the profiles in the presence of plasma is a turbulent electric field.

The C++ based simulation, which includes the turbulent electric field, was used to describe the experimental profiles in the presence of plasma. First, it was shown that the elongated fast ion current density profiles can be explained by the spread in the fast ion velocity distribution function. The shapes of the experimental profiles are in qualitative agreement with the simulations. The increase in radial FWHM with respect to the case without plasma predicted by the simulation was experimentally observed.

The vertical FWHM in the simulation remains the same as in the cases without a turbulent electric field. This is in contrast to the experiment, where the vertical FWHM is larger in the presence of plasma. A larger spread of the velocity distribution can in principle explain the increase in vertical FWHM, but we do not have other supporting evidence for such larger

spread. In fact, the conservation of the integral of the measured profile suggests that there are no significant changes in the fast ion energy or velocity distribution.

In the simulation, the position of the profile maximum shifts upwards in the cases with a turbulent electric field with respect to the zero electric field cases. In the experiments, a significant downward shift of the profile maximum is present in the case of the 300eV fast ion beam and in the blob region. The discrepancy in the asymmetry of the simulated and measured profiles can in principle be due to the non-Gaussian shape of the fast ion velocity distribution in the experiments .

A full system for experiments on the interaction between fast ions and the turbulence including the source and detector was built and was successfully tested. Clear effects of the interchange turbulence on the fast ion beam dynamics were observed. These effects understood with the help of the dedicated numerical simulations that use a turbulent electric field from a two fluid simulation of TORPEX plasmas, even though there are aspects that require a better modeling and further experiments.

Simulations with more realistic electric field intensities and fast ion velocity distribution functions could result in a more realistic description of the fast ion behavior, and in particular, could account for the observed profile asymmetry and the measured radial FWHM.

The double gridded energy analyzer allows a reconstruction of the energy distribution function. Further measurements using this system can clarify the question of the vertical profile width increase with plasma. Experiments with different fast ion energies will help establish the energy dependence of the fast ion transport. For the investigation of the fast ion transport the measurements of the fast ion profile spread, σ, at different toroidal postions, i.e. after different times of flight, t, would also be important. One would then be able to verify which mechanism is at play: for the usual diffusion $\sigma^2 \propto t$, while $\sigma^2 \propto t^\gamma$ if $\gamma < 1$ the transport is sub-diffusive, and if $\gamma > 1$ it is super-diffusive.

Experiments with a more powerful fast ion source could show how the turbulence can be modified by fast ions. For this, two different experimental scenarios can be investigated. First, the fast ion source can be installed into a material limiter to minimize the plasma perturbation due to the relatively large physical dimensions of the source. Alternatively, we can place the fast ion source in the poloidal region where the plasma perturbation due to the source dimensions has a negligible effect on the turbulence, and launch the fast ion beam in the region with unperturbed turbulent plasma.

Finally, in tokamaks, the alpha particles are born isotropically. To improve our understanding of the interaction of the alpha particles with turbulence, experiments with different source pitch angles should be conducted.

Bibliography

[1] R. Aymar, P. Barabaschi, Y. Shimomura, “The ITER design”, Plasma Phys. Control. Fusion, **44**, 519 (2002).

[2] L. A. Artcimovich, Nucl. Fusion, **12**, 215 (1972).

[3] H.P. Furth, Nucl. Fusion, **15**, 487 (1975).

[4] H. E. Mynick and S. J. Zweben, Nucl. Fusion, **32**, 518 (1992).

[5] A. N. Karpushov, S. Coda, and B. P. Duval, 30th EPS Conference on Controlled Fusion and Plasma Physics, St. Petersburg, Russia, 7–11 July, (2003).

[6] A. Fasoli et al, Nucl. Fusion, **47,** S264 (2007).

[7] H. E. Mynick and J. A. Krommes, Phys. Rev. Lett., **43**, 1506 (1979).

[8] ITER Physics Base Editors, Nucl. Fusion, **39**, 2137 (1999).

[9] S. J. Zweben, R. V. Budny, D. S. Darrow, S. S. Medley, R. Nazikian, B. C. Stratton, E. J. Synakowski, and G. Taylor, Nucl. Fusion, **40**, 91 (2000).

[10] Günter S. et al, Nucl. Fusion **45**, S98 (2005).

[11] W. W. Heidbrink and G. J. Sadler, Nucl. Fusion, **34**, 535 (1994).

[12] J. R. Myra, P. J. Catto, H. E. Mynick, and R. E. Duvall, Phys. Fluids B, **5**, 1160 (1993).

[13] G. Rewoldt, Phys. Fluids, **31**, 3727 (1988).

[14] R. B. White and H. E. Mynick, Phys. Fluids B, **1**, 980 (1989).

[15] G. Manfredi and R. O. Dendy, Phys. Rev. Lett., **76**, 4360 (1996).

[16] G. Manfredi and R. O. Dendy, Phys. Plasmas, **4**, 628 (1997).

[17] S. V. Annibaldi, G. Manfredi, and R. O. Dendy, Phys. Plasmas, **9**, 791 (2002).

[18] M. Vlad and F. Spineanu, Plasma Phys. Controlled Fusion, **47**, 281 (2005).

[19] M. Vlad, F. Spineanu, S.-I. Itoh, M. Yagi, and K. Itoh Plasma Phys. Controlled Fusion, **47**, 1015 (2005).

[20] G. Rewoldt, Nucl. Fusion, **31**, 2333 (1991).

[21] M. Albergante, J. P. Graves, T. Dannert, A. Fasoli, F. Zonca, S. Briguglio, G. Vlad and G. Fogaccia, Joint Varenna-Lausanne International Workshop, Varenna, Italy, 25 - 29 August, (2008).

[22] T. Hauff and F. Jenko, Phys. Plasmas, **15**, 112307 (2008).

[23] T. Hauff, M. J. Pueschel, T. Dannert, and F. Jenko, Phys. Rev. Lett., **102**, 075004 (2009).

[24] C. Estrada-Mila, J. Candy and R. E. Waltz, Phys. Plasmas, **13**, 112303 (2006).

[25] G. Manfredi and R. O. Dendy, Phys. Rev. Lett., **76**, 4360 (1996).

[26] A. Fasoli, B. Labit, M. McGrath, S. H. Müller, M. Podestà, F. M. Poli, and G. Plyushchev, Bull. Am. Phys. Soc., **48**, 119 (2003).

[27] F.M. Poli, A. Diallo, A.Fasoli et al, Phys. Plasmas, **13**, 102104 (2006).

[28] F.M. Poli, M Podestà and A Fasoli, Phys. Plasmas **14** 052311 (2007).

[29] B. Labit, A. Diallo, A Fasoli et al, Plasma Phys. Contrl. Fusion, **49**, B281 (2007).

[30] S.H. Müller, C. Theiler, A. Fasoli et al, Plasma Phys. Control. Fusion, **51** 055020 (2009).

[31] L. Federspiel, B. Labit, P. Ricci et al, Phys. Plasmas, **16**, 092501 (2009).

[32] A. Fasoli, B. Labit, M. McGrath et al, Phys. Plasmas, **13**, 055902, (2006).

[33] C. Theiler, I. Furno, P. Ricci et al, Phys. Rev. Lett. **103**, 065001 (2009).

[34] S. H. Müller, Ph.D. thesis, Ecole Polytechnique Fédérale de Lausanne, (2006).

[35] M. Podesta, Ph.D. thesis, Ecole Polytechnique Fédérale de Lausanne, (2007).

[36] MDSplus web site. URL: http://www.mdsplus.org

[37] D-tAcq web site. URL: http://www.d-tacq.com/ACQ32CPCI.shtml

[38] D-tAcq web site. URL: http://www.d-tacq.com/acq196cpci.shtml

[39] BITBUS web site. URL: http://www.bitbus.org

[40] S. L. Leonard, In *Plasma Diagnostic Technique*. R. H. Huddlestone and S. L. Leonard, eds. p.7 New York: Academic (1965).

[41] J. Wesson, “Tokamaks”, Clarendon Press Oxford, Third edition (2004).

[42] Mukhovatov V.S., Shafranov V.D., Nucl. Fusion, **11**, 605 (1971).

[43] E. Küng, Master’s thesis, Ecole Polytechnique Fédérale de Lausanne, (2008).

[44] G. Plyushchev, H. Boehmer, A. Diallo,et al, Rev. Sci. Instrum., **77**, 10F503 (2006).

[45] O.W. Richardson. "The Emission of Electricity from Hot Bodies", Longman's, Green and Company, London, (1916).

[46] Physik der Glühelektroden, Akademische Verlagsgesellschaft, Leipzig, (1928).

[47] F.M. Johnson, RCA Rev., **50**, 427 (1962).

[48] W. Schottky, Phys. Z., **15**, 872 (1914).

[49] J. R. Pierce, Proc. IRE, **29**, 28 (1941).

[50] J. R. Pierce, "Theory and Design of Electron Beams." Van Nostrand, Princeton, New Jersey (1949).

[51] T. Ichikawa , K. Akiyama, G. Satoh, H. Koizumi, Chem. Phys. Lett., **313**, 129 (1999).

[52] O.Heinz, R.T.Reaves, Rev. Sci. Instr., **39**, 8 (1968).

[53] HeatWaveLabs web site. URL: http://www.cathode.com/pdf/tb-118.pdf

[54] J.P. Blewett and E.J. Jones: Phys. Rev., **50**, 465, (1936).

[55] J. L. Hundley, Phys. Rev., **30,** 864 (1927).

[56] Cotronics web site. URL: http://www.cotronics.com/vo/cotr/ca_onecomp.htm

[57] W. Gekelman, H. Pfister, Z. Lucky, J. Bamber, D. Leneman, and J. Maggs, Rev. Sci. Instrum., **62**, 2875 (1991).

[58] I. H. Hutchinson, *Principles of plasma diagnostics*, Cambridge University Press, New York, (1987).

[59] W. Nagle, W3DUQ, *The Synchronous Detection Process*, 73 Magazine, September, (1967).

[60] T. H. Stix, Plasma Phys., **14**, 367 (1972).

[61] C. D. Child, Phys. Rev., **32**, 492 (1911).

[62] I. Langmuir, Phys. Rev., **2**, 450, (1913).

[63] I. Langmuir, Phys. Rev., **21**, 419 (1923).

[64] U. M. Ascher, L. R. Petzold, *Computer methods for ordinary differential equations and differential-algebraic equations*, SIAM. ISBN 0898714125 (1998).

[65] S. Brunner, E. Valeo and J. A. Krommes, Phys. Plasmas, **6**, 4504 (1999).

[66] A. Burckel, Master's thesis, Ecole Polytechnique Fédérale de Lausanne, (2009).

[67] C. K. Bidsall, A. B. Langdon, *Plasma physics via computer simulation*, McGraw-Hill book company, (1985).

[68] P. Ricci, B. N. Rogers, and S. Brunner, Phys. Rev. Lett., **100**, 225002 (2008).

[69] S. I. Braginskii. Reviews of Plasma Physics, **1**, 205 (1965).

[70] F. F. Chen, *Introduction to Plasma Physics and Controlled Fusion*, Plenum Press, New York (1984).

[71] I. Furno, B. Labit, A. Fasoli et al, Phys. Plasmas, **15**, 055903 (2008).

[72] M. Cotte, Ann. Phys. (Paris) [11] **10**, 333 (1938).

[73] R. Loosjes, H. J. Vink Philips Res. Rep., **4**, 449 (1949).

[74] P. Ricci, et al, Phys. Plasmas, **16**, 055703 (2009).

Acknowledgments

I would like to thank, first and foremost, my thesis supervisor, Prof. Ambrogio Fasoli, for his essential scientific support and his constant encouragements during all these years. I would also like to acknowledge his efforts to improve my presentation and writing skills.

I am very grateful to all TORPEX team, and especially to Dr. Ivo Furno and Dr. Mark McGrath, for their advices, suggestions and help.

I would like to send my thanks to all members of technical staff of CRPP. In particular, I wish to thanks Omar Bartolomeoli, Albert Perez, Jean-Michel Mayor, Rene Chavan, Patrice Gorgerat and Pierre Lavanchy.

I am grateful to Prof. Giovanni Dietler, Dr. Joseph Snipes, Dr. Jonathan Graves and Dr. Carlos Hidalgo, for accepting to be members of my jury.

I would like also to express my gratitude to Prof. Minh Quang Tran and Dr. Kurt Appert for giving me the opportunity to start my PhD study at CRPP.

I also would like to thank my friends and my volleyball team-mates Lesya Shchutska, Olexandr Gudozhnik, Victoria Glushko, Irina Sidorova, Veronika Maslova, Prof. Yury Tsybin, Dr. Tagir Aushev, Aleksey Vorobyev, who made my stay in Switzerland enjoyable.

Gennady PLYUSHCHEV
Chemin des Bruyeres 5
CH1007 Lausanne
Switzerland
Mobile: +41 79 577 2736
E-mail: gennady.plyushchev@gmail.com

June 30, 1981
Male
Single
Russian
Permit B

Education

Ecole Polytechnique Federale de Lausanne – EPFL. Doctoral program in physics.	since 2004
Moscow Engineering Physics Institute (State University) – MEPhI, 115409 Moscow, Russian Federation. Diploma with **the Honours**. *Specialty:* Nuclear physics. *Qualification:* Engineer-Physicist. **GPA 5.0** (out of 5.0).	1998-2004
Graduated from Secondary Lenin School of General Education in Pochep, Braynsk Region, Russian Federation. Certificate with **the SILVER medal**. **GPA 4.9** (out of 5.0).	1998

Languages

English:	working knowledge
French:	working knowledge
Russian:	mother language

Computer skills

Mac OS, Unix, Windows, Matlab, SolidWorks, MS Office, OpenOffice, HTML.

Publications

Refereed Journal Articles

G. Plyushchev, H. Boehmer, A. Diallo et al, **A new fast ion source and detector for investigating the interaction of turbulence with supra-thermal ions in a simple magnetized toroidal plasma**, Rev. Sci. Instrum. 77, 10F503 (2006)

C. Theiler, including G. Plyushchev, **Cross-Field Motion of Plasma Blobs in an Open Magnetic Field Line Configuration** Phys. Rev. Lett. **103**, 065001 (2009)

B. Labit, including G. Plyushchev, **Statistical properties of electrostatic turbulence in toroidal magnetized plasmas**, Plasma Phys. Contrl. Fusion **49** B281 (2007)

B. Labit, including G. Plyushchev, **Universal statistical properties of drift-interchange turbulence in TORPEX toroidal plasmas**, Phys. Rev. Lett. **98** 255002 (2007)

A. Fasoli, including G. Plyushchev, **Electrostatic Turbulence and Transport in a Simple Magnetized Plasma** , Phys. Plasmas, **13**, 055902, (2006)

S.H. Müller, including G. Plyushchev, **Probabilistic analysis of turbulence structures from 2D plasma imaging**, Phys. Plasmas **13**, 100701 (2006)

F.M. Poli, including G. Plyushchev, **Experimental characterization of drift-interchange instabilities in a simple toroidal plasma**, Phys. Plasmas **13**, 102104 (2006)

S.H. Müller, including G. Plyushchev, **Basic turbulence studies on toroidal plasma experiment and challenges in the theory-experiment comparison**, Phys. Plasmas, **12**, 090906 (2005)